

# Kerr Nonlinearity Compensation Using Polarization-Independent Fiber-Based Optical Parametric Amplifier in High-Speed Optical Transmission Systems

vorgelegt von  
M.Sc.  
Isaac Sackey  
geb. in Obuasi

von der Fakultät IV - Elektrotechnik und Informatik  
der Technischen Universität Berlin  
zur Erlangung des akademischen Grades

Doktor der Ingenieurwissenschaften  
-Dr.-Ing.-

genehmigte Dissertation

Promotionsausschuss:

Vorsitzender: Prof. Dr. Giuseppe Caire

Gutachter: Prof. Dr.-Ing. Klaus Petermann

Gutachter: Prof. Dr. Nick Doran

Gutachter: Dr.-Ing. Ronald Freund

Tag der wissenschaftlichen Aussprache: 10. Mai 2016

Berlin 2016



*To my wife Linda  
and  
children: Emmanuel, Joel and Ethan*



# Acknowledgment

The four-year journey leading to this Ph.D. dissertation has been very exciting. I wish to thank my supervisor, Professor Klaus Petermann, for always being there to provide the necessary light on this path when there was darkness. I also thank him for his unwavering interest in this research work. I have not only acquired academic knowledge from him, but his humility and great sense of humor as well.

My thanks also go to my group leader, Dr. Colja Schubert, for providing the serene and conducive atmosphere during my four-year stay as a guest research scientist at the Fraunhofer Heinrich Hertz Institute (HHI) in Berlin. In fact, his tolerance and ability to get work done on schedule has had a great impact on me. I am also extremely grateful to Dr. Thomas Richter, Dr. Robert Elschner, and Dr. Mahmoud Jazayerifar for their insightful guidance, good support, and for being excellent academic role models. Their consistent interest in seeing me transcend beyond the ordinary to the extra-ordinary is recommendable.

I am grateful to the rest of my colleagues at the Fraunhofer HHI, namely; Dr. Christian Meuer, Dr. Markus Nölle, Dr. Johannes Fischer, Dr. Carsten Schmidt-Langhorst, Lutz Molle, Pablo Wilke-Berenguer, Felix Frey, Saleem Al-reesh, and Dirk-Daniel Groß for sharing their knowledge and expertise. Dr. Georg Rademacher and the rest of my colleagues at the High Frequency Technique and Photonic Engineering Department, Technischen Universität Berlin, are acknowledged for their support towards this work. I am also pleased to have worked with Dr. Francesco Da Ros and Professor Christophe Peucheret in some joint research works at the Fraunhofer HHI.

I am extremely grateful for the financial support from the Deutsche Forschungsgemeinschaft (DFG) through Professor Hans-Joachim Grallert, who made it possible for me. It is my utmost prayer that Jehovah blesses you all. Amen!!

Isaac Sackey  
Berlin, December 2015



# Abstract

Kerr nonlinearity compensation in long-haul optical transmission networks has become necessary since the nonlinear impairment poses fundamental limits on the achievable transmission reach. Mid-link spectral inversion technique employing Fiber-based optical parametric amplifier (FOPA)s exhibit the capabilities for nonlinearity compensation through optical phase conjugation (OPC). However, the implementation of FOPAs in practical transmission systems is limited by their inherent polarization-dependent nature. Nevertheless, FOPAs employing the polarization-diversity loop scheme can be operated as polarization-independent optical sub-systems. The presence of Brillouin scattering in the diversity loop can degrade data signals significantly.

This thesis focuses on the experimental investigation of the stimulated Brillouin scattering (SBS)-induced distortions in a polarization-independent FOPA based on the polarization - diversity loop scheme. Initially, a single - pump polarization-independent FOPA using a polarization-maintaining highly nonlinear fiber (PM-HNLF) in the diversity loop is experimentally investigated. Parametric on-off gain for up to 20 dB, using a continuous wave (CW) signal and a 28-GBd single-polarization (SP) quadrature phase-shift keying (QPSK) data signal, are used in the investigation. It is shown that Brillouin scattering between the counter-propagating pumps in the diversity loop yields polarization-dependent gain (PDG) if an asymmetric local dispersion profile of the used highly nonlinear fiber (HNLF) is present.

In addition, a dual-pump polarization-independent FOPA is also designed and experimentally investigated in terms of amplification and wavelength conversion for OPC applications. A 28-GBd polarization-division multiplexed (PDM) 16-ary quadrature amplitude modulation (16-QAM) signal in a 50-GHz spaced five-channel wavelength-division multiplexing (WDM) system is used in the investigation. Mid-link spectral inversion technique employing the OPC device is used for nonlinearity compensation of  $5 \times 28$ -GBd PDM 16-QAM signal transmis-

sion over both a dispersion-compensated link and a dispersion-uncompensated link. A significant increase in nonlinear tolerance is demonstrated. The performance of the mid-link OPC is compared with digital back-propagation algorithm employing the split-step Fourier method for nonlinearity compensation. Signal transmission over up to 800-km of dispersion-compensated link shows that in the single-channel case, the use of the back-propagation algorithm outperformed the OPC. However, with reference to the hard-decision forward-error correction (HD-FEC) threshold, signal transmission was not possible with digital back-propagation in the WDM scenario over the same link length while it was enabled by the OPC.

# Zusammenfassung

Diese Arbeit ist fokussiert auf die experimentelle Untersuchung von Streuungsbedingten Störungen in polarisations - unabhängigen Fiber-based optical parametric amplifiers (FOPAs), welche auf dem Polarisations - diversen Faserring-Schema basieren. Zunächst wird ein solches Schema in einer Konfiguration mit einem einzelnen Pumpsignal und einer polarisations - erhaltenden hochnichtlinearen Faser (HNLf) für Verstärkungen bis zu 20 dB untersucht. Als Eingangssignal wird sowohl ein unmoduliertes Signal als auch ein single - polarization 28-GBd QPSK-moduliertes Signal verwendet. Die im FOPA erzeugten Signalstörungen wurden untersucht und es konnte gezeigt werden, dass Brillouin-Streuung zwischen dem gegenläufigen Pumpsignal im Faserring zu polarisationsabhängiger Verstärkung führt, wenn die HNLf ein asymmetrisches Dispersionsprofil besitzt.

Zusätzlich wurde ein Versuchsaufbau realisiert, bei dem zwei Pumpsignale im Polarisations-diversen Faserring-Schema eingesetzt werden. Dieser wurde zum einen in Bezug auf Signalverstärkung charakterisiert und zum anderen für Wellenlängenumsetzung für OPC-Anwendungen. Hierbei wurden 28-GBd polarisations - gemultiplexte (PDM) 16-QAM Signale in einem fünf - Kanal - Wellenlängenmultiplex (WDM)-System mit 50 GHz Kanalabstand verwendet. Die Technik der Mid-Link spektralen Inversion wurde mit dem realisierten OPC-Aufbau für die Kompensation von nichtlinearen Signalstörungen in einem  $5 \times 28$ -GBd PDM 16-QAM Übertragungssystem untersucht. Dies wurde für dispersionskompensierte als auch dispersionsunkompensierte Faserstrecken untersucht. Eine deutliche Vergrößerung der nichtlinearen Toleranz konnte hierbei demonstriert werden. Des Weiteren wurde die Güte der Signalübertragung mit der Technik der Digitalen-Rückwärtsausbreitung verglichen, die auf einer Split-Step-Fourier-Methode basiert und ebenso nichtlineare Signalstörungen kompensieren kann. Übertragungsexperimente wurden bis zu einer Distanz von 800 km durchgeführt. Im Einkanalfall konnte eine deutlich bessere Signalübertragungsgüte bei

Nutzung der digitalen Rückwärtsausbreitung erzielt werden. Hingegen war die Übertragung im WDM-Fall nur mit der Nutzung des OPC-Aufbaus für die anvisierte Signalfüte erzielbar.

# Contents

<b>Dedication</b>	<b>iii</b>
<b>Acknowledgment</b>	<b>v</b>
<b>Abstract</b>	<b>vii</b>
<b>Zusammenfassung</b>	<b>ix</b>
<b>Contents</b>	<b>xi</b>
<b>1 Introduction</b>	<b>1</b>
1.1 The need for Kerr nonlinearity compensation . . . . .	2
1.2 Challenges in practical fiber-based OPC devices . . . . .	5
1.3 Organization of the Thesis . . . . .	6
<b>2 Advanced Modulation Formats and Coherent Reception</b>	<b>9</b>
2.1 Advanced modulation formats . . . . .	9
2.2 Direct detection . . . . .	11
2.3 Coherent detection . . . . .	12
2.4 Optical signal-to-noise ratio (OSNR) . . . . .	14
2.5 Summary . . . . .	17
<b>3 Linear and Nonlinear Effects in Optical Fibers</b>	<b>19</b>
3.1 Introduction to optical fibers . . . . .	19
3.2 Linear effects in optical fibers . . . . .	21
3.2.1 Attenuation . . . . .	21
3.2.2 Chromatic dispersion . . . . .	22
3.2.3 Polarization mode dispersion (PMD) . . . . .	25
3.3 Nonlinear effects in optical fibers . . . . .	27
3.3.1 Inelastic nonlinear effects . . . . .	27

3.3.2	Elastic nonlinear effects . . . . .	31
3.4	Summary . . . . .	34
<b>4</b>	<b>Fundamentals of Fiber-based Optical Parametric Amplifier</b>	<b>35</b>
4.1	Phase-matching in FOPAs . . . . .	36
4.2	Polarization-dependent FOPAs . . . . .	36
4.2.1	Single-pump polarization-dependent FOPA . . . . .	37
4.2.2	Dual-pump polarization-dependent FOPA . . . . .	40
4.3	Polarization-independent FOPA . . . . .	43
4.3.1	Orthogonally polarized pumps . . . . .	43
4.3.2	Polarization-diversity configurations . . . . .	44
4.4	Impact of pump-induced distortions . . . . .	47
4.4.1	Pump relative intensity noise (RIN) and pump optical single- to-noise ratio (OSNR) . . . . .	47
4.4.2	Effect of pump line-width broadening . . . . .	47
4.5	Summary . . . . .	48
<b>5</b>	<b>Realization of a Fiber-based Optical Parametric Amplifier</b>	<b>49</b>
5.1	Characterization of a polarization-dependent FOPA . . . . .	49
5.1.1	Stimulated Brillouin scattering measurement of a PM-HNLF	49
5.1.2	Impact of pump wavelength detuning and pump power vari- ation on the signal gain-bandwidth . . . . .	52
5.1.3	Saturation measurement . . . . .	55
5.2	Characterization of a polarization - independent FOPA . . . . .	57
5.2.1	Impact of back-reflections in a polarization-diversity loop .	57
5.2.2	Evaluation of pump splitting optimization . . . . .	66
5.2.3	Non-reciprocal gain due to counter-propagating pumps in a polarization-independent FOPA with diversity loop . . . .	72
5.3	Impact of SBS-induced distortions on QPSK signal in a FOPA . . . .	79
5.3.1	28-GBd single-polarization QPSK transmitter setup . . . .	79
5.3.2	Coherent receiver for a 28-GBd single-polarization QPSK signal . . . . .	80
5.3.3	Impact of pump distortion on 28-GBd SP QPSK signal . . .	81
5.4	HNLF requirement for system experiments . . . . .	84
5.5	Summary . . . . .	85

<b>6</b>	<b>Design of a FOPA-based OPC Device</b>	<b>87</b>
6.1	Fundamentals of optical phase conjugation . . . . .	88
6.1.1	Limitations of OPC based on mid-link spectral inversion . .	89
6.1.2	Requirements for an efficient OPC device . . . . .	90
6.2	Experimental realization of OPC device . . . . .	90
6.2.1	28-GBd PDM 16-QAM transmitter setup . . . . .	91
6.2.2	Setup of a coherent receiver for a PDM 16-QAM signals . . .	92
6.2.3	Design of a FOPA-based OPC device . . . . .	93
6.2.4	OPC device performance evaluation . . . . .	95
6.3	Summary . . . . .	101
<b>7</b>	<b>Kerr Nonlinearity Mitigation Using a FOPA-based OPC Device</b>	<b>103</b>
7.1	Transmission link design based on mid-link OPC . . . . .	104
7.1.1	Mid-link OPC-based transmission links utilizing erbium-doped fiber amplifier (EDFA)s . . . . .	104
7.1.2	Mid-link OPC-based transmission links utilizing distributed Raman amplification (DRA) . . . . .	106
7.2	Mitigation of nonlinear effects in a dispersion - compensated link	109
7.2.1	Experimental setup: Link with mid-link OPC and dispersion-compensated spans with EDFAs. . . . .	109
7.2.2	Results and discussion . . . . .	111
7.2.3	Nonlinearity mitigation: mid-link OPC versus digital back-propagation (DBP) . . . . .	117
7.3	Mitigation of nonlinear effects in a dispersion - uncompensated link	122
7.3.1	Experimental setup: Link with mid-link OPC and dispersion-uncompensated spans with backward-pumped DRA. . . . .	122
7.3.2	Results and discussion . . . . .	124
7.4	Summary . . . . .	126
<b>8</b>	<b>Summary and Conclusion</b>	<b>129</b>
8.1	Summary . . . . .	129
8.1.1	SBS-induced pump distortion . . . . .	129
8.1.2	Polarization dependent gain (PDG) in diversity loop scheme	131
8.1.3	Transmission links with mid-link fiber-based OPC . . . . .	131
8.2	Conclusion . . . . .	133
	<b>Bibliography</b>	<b>135</b>

<b>Appendix A Digital Back-propagation (DBP)</b>	<b>153</b>
<b>Appendix B List of Acronyms</b>	<b>157</b>
<b>Appendix C List of Symbols</b>	<b>161</b>
<b>Appendix D Author Publications</b>	<b>165</b>

# List of Figures

2.1	Constellation diagrams of some commonly used modulation formats.	10
2.2	A schematic representation of a single-polarization coherent receiver front-end. . . . .	13
2.3	A representation of a point-to-point transmission link consisting of $N$ fiber spans and $N$ EDFAs. . . . .	15
3.1	Schematic representation of the cross-section of a step-index fiber showing the refractive index profile over the radial distance of the core and cladding of the fiber. $n_{cl}$ = cladding refractive index, $n_{co}$ = core refractive index, $r_{cl}$ = cladding radius, $r_{co}$ = core radius. . .	20
3.2	Pulse propagation in a single-mode fiber which has slightly different refractive indices of the two orthogonal principal axes (fast and slow axis) leading to differential group delay (DGD) (between the polarization components) and eventually pulse broadening. . .	26
3.3	Simulated SBS threshold of a 300 m fiber showing the reflected power at a given input power with and without SBS suppression implementation. . . . .	29
3.4	Generation of new frequency components due to four-wave mixing (FWM) of three input optical waves of frequencies $\omega_{p1}$ , $\omega_{p2}$ and $\omega_s$ [1].	34
4.1	Single-pump polarization-dependent FOPA showing the generated idler and signal amplification at the output of the HNLF. . . . .	37
4.2	Simulated single-pump polarization-dependent FOPA gain-spectrum.	40
4.3	Dual-pump polarization-dependent FOPA showing the generated idler and signal amplification at the output of the HNLF. . . . .	41
4.4	Simulated dual-pump polarization-dependent FOPA gain-spectrum.	42
4.5	Schematic representation of orthogonally polarized pumps for polarization - independent FOPA operation. . . . .	44

4.6	Polarization-independent technique based on: (i) polarization diversity scheme with parallel configuration, (ii) polarization-diversity loop scheme, and (iii) polarization-diversity loop scheme employing a circulator (CIR). . . . .	45
5.1	Experimental setup for the SBS measurement. . . . .	50
5.2	SBS measurements for up to 3-RF pump phase-dithering tones of frequencies: 75 MHz, 275 MHz, and 875 MHz. . . . .	52
5.3	Schematic representation of the experimental setup of a single-pump polarization-dependent FOPA. . . . .	53
5.4	Evaluation of a single-pump polarization-dependent FOPA on the: (a) Impact of pump wavelength detuning on the signal gain - bandwidth profile at a fixed pump power of 31.5 dBm. (b) impact of pump power variation on the signal gain-bandwidth profile at a fixed pump wavelength of 1562 nm. Solid lines-theoretical simulation (Sim.) using equation (4.13), symbols-experimental (Exp.) results. Remark that $\lambda_{zd} = 1561.0$ nm. . . . .	54
5.5	Experimental setup for saturation measurement of a single-pump polarization-dependent FOPA. . . . .	56
5.6	Saturation characteristics of a single-pump polarization-dependent FOPA operating at a pump power of 31.5 dBm. . . . .	56
5.7	Experimental setups: (a) Single-pump polarization-independent FOPA based on the polarization-diversity loop scheme. (b) Modified setup of a single-pump polarization-independent FOPA based on the polarization-diversity loop so as to control the clockwise (A to B) and counter-clockwise (B to A) propagating pump waves in the diversity loop. . . . .	58
5.8	Optical pump spectrum (after 20-dB coupler) with phase-dithering of 3-RF tones (optical spectrum analyzer (OSA) resolution of 0.01 nm) showing SBS-induced distortion at (a) $P_p = 27$ dBm at each direction of the fiber. (b) $P_p = 28.5$ dBm at each direction of the fiber. (c) $P_p = 31.5$ dBm at each direction of the fiber. . . . .	61
5.9	Growth of side-band power of the (A to B) pump (i.e., difference between the side-band (SB) power and the main-band (MB) power in dB) with counter pump (B to A) switched on and off. OSA resolution bandwidth = 0.5 nm. . . . .	62

5.10	A heterodyne electrical spectrum of the pump laser (after the phase modulator) for the cases: (i) with no pump phase-dithering radio frequency (RF) tone, (ii) with 3-RF phase-dithering tones, (iii) with 4-RF phase-dithering tones. Electrical spectrum analyzer resolution bandwidth = 10 MHz and video bandwidth = 10 MHz*.	63
5.11	Optical spectrum of the pump (after 20-dB coupler) for 3- and 4-RF tones (i) with no counter propagating pump, (ii) with counter propagating pump. $P_p = 27$ dBm at each direction of the fiber. 0.01-nm OSA resolution bandwidth.	64
5.12	Schematic representation of pump evolution in the PM-HNLF showing the induced-distortion due to the SBS counter-propagation of the pump.	65
5.13	Schematic representation of pump distortion as a function of the total pump spectral width of a FOPA based on the polarization-diversity loop.	65
5.14	(a) Average signal on-off gain spectra at $P_p = 33$ dBm and $P_p = 31.5$ dBm. (b) Spectra, after 20-dB coupler, at the output of the PM-HNLF showing the signal on-off gain the the generated idler with pump off and on at $P_p = 33$ dBm and $P_p = 31.5$ dBm. (c) Residual PDG of the FOPA with pump switched-off. OSA resolution bandwidth of 0.5 nm.	67
5.15	(a) At $P_p = 31.5$ dBm: Optimization of pump splitting at each signal wavelength. (b) Optimization of pump splitting at a single signal wavelength of 1542 nm. Note that for a particular graph, the y-axis on the left hand side is for the average signal gain whereas the y-axis on the right hand side is for the PDG.	69
5.16	At $P_p = 33$ dBm: (a) Optimization of pump splitting at each signal wavelength. (b) Optimization of pump splitting at a signal wavelength of 1532 nm. Note that for a particular graph, the y-axis on the left hand side is for the average signal gain whereas the y-axis on the right hand side is for the PDG.	70
5.17	At $P_p = 33$ dBm: Optimization of pump splitting at a signal wavelength of (a) 1540 nm. (b) 1544 nm. Note that for a particular graph, the y-axis on the left hand side is for the average signal gain whereas the y-axis on the right hand side is for the PDG.	70

5.18 PDG stability monitoring of the polarization-independent FOPA over time. Note that the $y$ -axis on the left hand side is for the average signal gain whereas the $y$ -axis on the right hand side is for the PDG.	71
5.19 Schematic representation of the experimental setup depicting the modified setup of a single-pump polarization-independent FOPA based on the diversity loop scheme with four pump phase-dithering tones. (Note that a single high power EDFA is used).	73
5.20 Gain spectra of the A to B and the B to A directions of the diversity loop with polarization scrambler switched-off and the absolute difference between the two gain profiles (PDG = shaded region). It also shows the comparison of the PDG due to the difference between the two gain profiles with the measured PDG when the signal is polarization-scrambled as shown in Figure 5.17(b). 0.5-nm OSA resolution bandwidth.	74
5.21 (a) Signal gain in an open diversity loop (i.e., depicting straight FOPA configuration) for both directions of the PM-HNLF. (b) Comparison of signal gain spectral shape of a FOPA with straight configuration and a FOPA in a polarization-diversity loop (i.e., with counter propagating pumps) at the same on-off gain. 0.5-nm OSA resolution bandwidth.	75
5.22 A to B direction gain spectra with and without B to A pump. It also shows the comparison of the gain spectra in each direction of the HNLF when both pumps are turned-on. 0.5-nm OSA resolution bandwidth.	76
5.23 Illustration of non-reciprocal signal gain due to zero-dispersion wavelength ( $\lambda_{zd}$ ) variation and counter propagating pumps in polarization - diversity FOPA.	77
5.24 Experimental setup of a 28-GBd single-polarization (SP) QPSK transmitter.	80
5.25 Experimental setup of a 28-GBd single-polarization QPSK coherent receiver.	81
5.26 Experimental setup of a modified single - pump polarization - independent FOPA for the investigation of impact of pump distortion.	81

5.27	Optical spectra of the signal measured from the modified polarization - diversity loop with and without counter propagating pump (B to A pump). It shows the transfer of pump distortion due to pump phase-dithering (using frequency set I with up to 4-RF tones with frequencies 75, 275, 875 and 2710 MHz) to the modulated signal. OSA resolution bandwidth = 0.01 nm. . . . .	82
5.28	Constellation diagrams of the 28-GBd SP QPSK data signal (at 25-dB receiver OSNR) for the cases with and without counter propagating pump. The two different pump phase-dithering frequency sets (set I and set II) independently investigated at $P_p = 27$ dBm and $P_s = -14.5$ dBm per direction of the PM-HNLF. Average signal on-off gain = 5 dB. . . . .	83
6.1	Schematic representation of a mid-link OPC device in a 2-span transmission link showing the spectrum of the signal before and after the OPC unit. . . . .	89
6.2	Experimental setup of a 5 - channel 28 - GBd PDM 16-QAM transmitter. . . . .	92
6.3	Experimental setup of a 28-GBd PDM 16-QAM coherent receiver. . . . .	93
6.4	Experimental setup of a black-box OPC device based on a dual-pump polarization-independent FOPA. Note that a non-PM-HNLF is used. . . . .	94
6.5	Acquired idler electrical spectra from real-time oscilloscope (real-time oscilloscope (RTO)) showing suppression of pump phase - dithering tones on the generated idler. . . . .	96
6.6	Gain saturation characteristics of the FOPA-based OPC device. . . . .	96
6.7	(a) OPC device gain-bandwidth showing the regions of the signal and idler channels that is used for WDM performance analysis. (b) PDG evaluation of the OPC unit for the amplified signals and their corresponding idlers. . . . .	98
6.8	Optical spectra at the HNLF output of the OPC device, after a 20-dB coupler, showing the generated idlers and the signals at different on-off gain for: (a) signal-channel case. (b) 5-channel WDM scenario. OSA resolution bandwidth of 0.1 nm. . . . .	99

6.9	Receiver bit-error ratio (BER) curves for signal and idler at different gain levels: (a) Single-channel. (b) 5-channel WDM system. (c) OSNR penalties at a BER of $1 \times 10^{-4}$ for both signal and idler as functions of on-off gain. . . . .	100
6.10	29-dB receiver OSNR of $x$ -polarization of the polarization-scrambled 28-GBd PDM 16-QAM signal and idler constellation diagrams at 5-dB and 13-dB on-off gain for both single-channel and 5-channel WDM scenario. . . . .	101
7.1	Transmission link utilizing only EDFAs with: (a) dispersion - uncompensated spans. (b) dispersion - uncompensated spans with mid - link OPC. (c) dispersion - compensated (super large area (SLA)+inverse dispersion-shifted fiber (IDF)) spans with mid-link OPC, (Tx: transmitter, Rx: receiver). . . . .	105
7.2	Transmission link utilizing backward-pumped distributed Raman amplification (DRA) with: (a) dispersion-uncompensated spans. (b) dispersion-uncompensated spans with mid-link OPC. (c) dispersion-compensated spans (SLA+IDF) with mid-link OPC, (Tx: transmitter, Rx: receiver). . . . .	107
7.3	Experimental setup showing the $5 \times 28$ -GBd PDM 16-QAM transmitter, the dispersion-managed fiber spans (SLA+IDF), the dual-pump polarization-independent FOPA, which is used as OPC device, and the coherent receiver. . . . .	109
7.4	(a) Single-channel plot of $Q^2$ -factor versus launch power per polarization over 480 km, 640 km, and 800 km of dispersion-compensated transmission link showing the performances for the cases of straight transmission without nonlinearity mitigation and with OPC operation. (b) single-channel $X$ - and $Y$ -polarization constellation diagrams at 480 km and 800 km at signal launch power of $P_{\text{launch}} = -1$ dBm/pol. . . . .	112

7.5	(a) Five-channel WDM (center-channel): plot of $Q^2$ -factor versus launch power per channel per polarization over the 480 km, 640 km, and 800 km of dispersion-compensated transmission link showing the performances for the cases of straight transmission without nonlinearity mitigation and with OPC operation. (b) WDM-channel (center-channel): $X$ - and $Y$ -polarization constellation diagrams at 480 km and 800 km at signal launch power of $P_{\text{launch}} = -3$ dBm/ch/pol. . . . .	114
7.6	(a) Plot of $Q^2$ -factor as a function of channel index for the cases with and without OPC operation over the 800-km transmission length. (b) Summary of single-channel and WDM $Q^2$ -factor improvements for the 480-km, 640-km, and 800-km transmission lengths. . . . .	115
7.7	Power and dispersion map of the transmission link showing: (a) evolution of EDFA amplified signal power at 0 dBm, (b) signal and idler dispersion profiles before and after the OPC device, respectively.	116
7.8	Single-channel: plot of $Q^2$ -factor versus launch power per polarization, showing the performances for the cases of straight transmission without nonlinearity mitigation, with OPC operation and with split-step Fourier method digital back-propagation (digital back-propagation (DBP)) (a) over the 480-km transmission link at $P_{\text{launch}} = 1$ dBm/pol. (b) over the 800-km transmission link at $P_{\text{launch}} = 0$ dBm/pol. . . . .	119
7.9	Five-channel WDM (center-channel): plot of $Q^2$ -factor versus launch power per polarization, showing the performances for the cases of straight transmission without nonlinearity mitigation, with OPC operation and with split-step Fourier method back-propagation (DBP) (a) over the 480-km transmission link at $P_{\text{launch}} = -3$ dBm/ch/pol. (b) over the 800-km transmission link at $P_{\text{launch}} = -3$ dBm/ch/pol. . . . .	121
7.10	Experimental setup showing the $5 \times 28$ -GBd PDM 16-QAM transmitter, the 400-km dispersion-uncompensated link with backward-pumped distributed Raman amplification (DRA), the OPC device, and the coherent receiver. . . . .	123

7.11 (a) Single-channel: plot of $Q^2$ -factor as a function of launch power per polarization, showing the performances for the cases with and without OPC with the corresponding experimental constellation diagrams at a launch power of 2 dBm/pol. (b) Five-channel WDM (center-channel): plot of $Q^2$ -factor as a function of launch power per polarization, showing the performances for the cases with and without OPC with the corresponding constellation diagrams at a launch power of 2 dBm/pol. . . . .	125
----------------------------------------------------------------------------------------------------------------------------------------------------------------------------------------------------------------------------------------------------------------------------------------------------------------------------------------------------------------------------------------------------------------------------------------------------------------------------------------------------------------------	-----

# List of Tables

1.1 Comparison of some commonly used Kerr nonlinearity compensation schemes in optical transmission systems. Footnote: see page 2 . . . . .	3
5.1 Comparison of fiber specifications of a PM-HNLF and a non-PM-HNLF.	85
7.1 Specifications of the dispersion-compensated fiber (each span consists of SLA and IDF fibers). . . . .	110



# Chapter 1

## Introduction

Maximizing both the spectral efficiency (SE) and the transmission reach in today's optical communication systems is a major challenge which optical networks will have to address in the near future. This will help to sustain the growth in global data demand while using the existing deployed fiber plant at minimal cost per transmitted bit [2, 3]. Current optical networks are now aiming at transmission capacity beyond 400G on a single wavelength and extension of the transmission reach with a reduced cost.

Realizing such a goal, requires the maximization of the spectral efficiency and the transmission reach of the optical communication link [2,4]. The spectral efficiency improvement includes transmission of polarization-division multiplexed (PDM) signals, the use of higher-order modulation formats such as  $m$  - ary phase-shift keying (PSK) and  $m$  - ary quadrature amplitude modulation (QAM), e.g. 16-QAM. Additional figure-of-merits for the spectral efficiency improvement are the use of densely packed channels (e.g. dense wavelength-division multiplexing (WDM)) and the transmission with high data rate in the presence of coherent detection [5]. A current record of a line rate of 864 Gb/s, on a single carrier and employing a coherent receiver, has experimentally been achieved using a PDM 64-QAM modulation format [6].

Moving from lower spectrally efficient modulation formats to higher-order (multi-level) modulation formats requires higher optical signal-to-noise ratios (OSNR). High OSNR eventually requires higher signal launch power per fiber-span. However, Kerr nonlinearity provide an upper bound to the maximum transmittable signal launch power. The Kerr nonlinearity evolve itself in the form of self-phase modulation (SPM), inter - and intra - channel cross-phase modulation (XPM), and inter-and intra-channel four-wave mixing (FWM). This

effect reduces the reach for error-free transmission [2, 4, 7].

## 1.1 The need for Kerr nonlinearity compensation

The degrading impact of Kerr nonlinearities on systems with densely packed channels with higher-order modulation can be very significant [4, 7, 8]. Therefore, higher-order modulation formats cannot withstand longer transmission distance with acceptable degradation compared to less spectrally efficient modulation formats. Reduction in transmission reach as a result of nonlinear impairments of such systems make long-haul applications unattractive. With effective compensation for the nonlinear impairments arising from the transmission system, an increase in the transmission reach of the communication system can be achieved [4, 7].

In this context, recent years have witnessed consistent and progressive research studies with the aim to mitigate Kerr nonlinear distortions in optical transmission systems. Therefore, various numerical [9–12] and experimental [13–17] demonstrations for nonlinearity compensation have been shown. The nonlinear compensation schemes are either in the electrical domain [9–11, 13, 18–21] or in the optical domain [14–17, 22–27]. Some of the electrical domain compensation schemes include digital back-propagation (DBP) [9, 10, 18, 20, 21] and digital coherent superposition of phase-conjugated twin waves (PCTW) [19, 28, 29]. The all-optical domain nonlinearity compensation schemes also include optical coherent superposition using phase-sensitive amplification (PSA) (i.e., copier-PSA) [23, 30]. Another optical domain nonlinearity compensation scheme is the mid-link spectral inversion (MLSI) based on optical phase conjugation (OPC) [14–16, 24]. Table 1.1 shows comparison of Kerr nonlinearity compensation of the commonly used nonlinearity compensation schemes.

The digital signal processing (DSP) power requirements, by the electrical domain nonlinearity compensation schemes, in a high-speed data link dominated by fiber impairments can be significantly high\*. One way to avoid the high DSP requirements, imposed by electrical domain mitigation schemes, is by the implementation of all-optical mitigation schemes. The all-optical schemes provide real-time compensation without the need for electronic signal processing and with a reduced latency. Comparing the advantages and drawbacks of the various nonlinearity compensation schemes as shown in Table 1.1, the MLSI (i.e.,

---

\*Real-time digital nonlinearity compensation is, in principle, possible. However, according to Refs. [31, 32], practical implementation can be very challenging and computationally expensive.

	DBP	PCTW	Copier-PSA	Mid-link OPC
Effectiveness for single-channel	yes	yes	yes	yes
Effectiveness for WDM	no <sup>[9, 69, 125]</sup>	yes	yes	yes
real-time compensation	yes*	yes*	yes	yes
System design complexity	no	moderate	yes	no
Electrical bandwidth requirements for WDM	large <sup>[9, 69, 125]</sup>	less	less	less
Modulation format transparency	yes	yes	yes	yes
Optimization of spectral bandwidth	yes	no <sup>[19]</sup>	no <sup>[23, 30]</sup>	yes
Polarization-independence	yes	yes	no	yes
Noise figure	no	no	low (e.g. 0 dB)	moderate
Additional constraints	DSP computational complexity	signal and its conjugate require similar power and dispersion profiles	signal and its conjugate require similar power and dispersion profiles	symmetric power and dispersion profiles around the OPC device

**Table 1.1:** Comparison of some commonly used Kerr nonlinearity compensation schemes in optical transmission systems. Footnote: see page 2

mid-link OPC) technique offers more advantages than the other three nonlinearity compensation schemes.

The MLSI technique employs optical phase conjugation (OPC) of the propagating signal in the transmission link. It requires an OPC device in the middle of a transmission link [14, 22, 24, 26, 33, 34]. In a symmetric link, the accumulated signal distortions in the first half of the transmission link (i.e., before the OPC device) are reversed and compensated for during signal propagation in the remaining half of the link (i.e, after the OPC device) [14, 35–37].

The concept of OPC for chromatic dispersion compensation was first reported by Yariv et al. in 1979 [35]. The tendency of the OPC device to compensate for nonlinear distortion in a transmission link was theoretically shown by Pepper and Yariv [36]. Experimental implementation of an OPC device, in an optical transmission system, was demonstrated by Watanabe et al., for chromatic dispersion compensation in [37]. Nonlinearity compensation by the OPC device was experimentally shown in [22] and [14]. Thereafter, several numerical and experimental demonstrations for nonlinearity compensation using an OPC device based on different nonlinear media have been reported. The commonly used nonlinear media include semiconductor optical amplifier (SOA) [38], periodically-poled lithium-niobate (PPLN) [16, 39–42], silicon (Si) nanowire [43, 44], and highly-nonlinear fiber (HNLF) [14, 17, 45, 46].

For practical applications, an OPC device should provide broadband operation (capable of WDM operation) with flat gain-bandwidth profile, polarization-independence as well as wavelength and modulation format transparency. Furthermore, the OSNR implementation penalty of the OPC device must be sufficiently low. One way to achieve low OSNR implementation penalty is by using an OPC device which has a high positive conversion efficiency (CE) [47]. However, comparing the other nonlinear media to the HNLF, the SOA has a high noise figure and a limited bandwidth [48]. The PPLN, on the other hand, require high operating temperatures in order to reduce the influence of photo-refractive effects [15]. Therefore, the achievable bandwidth is limited (compared to that of HNLF) due to the temperature dependence on the pump wavelength [49]. The silicon nanowire, although it has a high nonlinear coefficient and a small foot-print, it suffers from severe nonlinear loss mechanisms such as two photon absorption in the C-band [50, 51].

The use of HNLFs to realize fiber-based optical parametric amplifiers (FOPAs) can be employed for nonlinearity compensation based on PSA and OPC. Some of the appealing features of FOPAs also include high gain (e.g. 70 dB gain) [52, 53], broad gain-bandwidth (e.g. 250-nm bandwidth) [54, 55], low-noise figure (e.g. 0 dB) [56], spectral inversion [1], and modulation format transparency. These unique features of FOPAs make them suitable for fulfilling the need for bandwidth and in-line amplification with low-noise figure. In addition, FOPAs are suitable for OPC devices for nonlinearity compensation and all-optical wavelength conversion [1, 47, 57].

Recent studies on the design of fiber-based OPC devices have been performed in a 100-GHz spaced  $10 \times 114$ -Gb/s PDM QPSK system [17]. In addition, WDM systems with up to 8-channels using PDM 16-QAM signals have been used to characterize an OPC device [45, 46]. Furthermore, the combination of Raman-based amplification and fiber-based OPC scheme has been recently demonstrated for nonlinear distortions compensation [26, 27, 34]. Multiple OPCs can also be implemented in a transmission link and this provides improved performance compared to the use of a single OPC in the link [25, 26, 34, 58]. Further discussions on nonlinearity compensation employing OPC are presented in Chapter 7.

## 1.2 Challenges in practical fiber-based OPC devices

Although the fiber-based OPC (i.e., FOPA-based OPC) has numerous promising features, it has several challenges which make practical implementation difficult. For instance, the underlying physical phenomenon of FOPA operation, which is FWM based on the third-order nonlinear susceptibility,  $\chi^{(3)}$ , is inherently polarization-dependent [59]. Therefore, polarization-independent operation is a prerequisite for practical application of FOPA in optical communication systems. This is due to the fact that the state-of-polarization (SOP) of a propagating signal in a transmission link is random. Again, due to the polarization-dependent nature of FOPA, their operation is very sensitive to changes in ambient temperature. Therefore using polarization - maintaining highly nonlinear fiber (PM-HNLF) as a gain medium for the FOPA will be interesting to be studied since polarization-maintaining fiber (PMF)s preserve the polarization of light when correctly launched into one of the principal axes of the PMF.

The realization of a polarization-independent FOPA using two orthogonally polarized pumps (high power signal) at different wavelengths has been shown [60,61]. The use of a polarization - diversity loop scheme to achieve polarization - independent FOPA operation has also been shown [62,63]. One main drawback of schemes employing orthogonally polarized pumps is the effect of birefringence variation of standard HNLFs [47, p. 252]. The fiber birefringence can cause the orthogonality of the pumps to be lost thereby leading to significant levels of polarization dependent gain (PDG) [64–66].

On the other hand, the polarization-diversity loop scheme is susceptible to stimulated Brillouin scattering (SBS) in the loop [67, 68], [47, p. 251]. The SBS can degrade the performance of the FOPA substantially especially at high-gain conditions [67]. In order to fully integrate FOPAs in current optical communication networks, polarization - independent operations especially at high gain conditions are paramount. The realization of a polarization-independent FOPA based on a polarization-diversity loop scheme in system experiments at high gain conditions have not been comprehensively studied.

The objectives of the thesis, therefore, are focused on two areas. One of the objectives is to characterize and implement a polarization-independent FOPA based on the polarization-diversity loop scheme. A PM-HNLF is to be employed for the implementation of the polarization-independent FOPA with high gain. Investigation of the impact of SBS in the diversity loop is of interest especially at high gain conditions. A continuous wave (CW) and a 28-GBd single-polarization QPSK

data signal will be used for the characterization of the polarization-independent FOPA.

The polarization-independent FOPA is to be used as an OPC device for non-linearity compensation in a WDM system. An experimental investigation of the FOPA-based polarization-independent OPC for Kerr nonlinearity compensation of higher-order modulation formats with higher symbol rates, which has so far not been extensively studied, is necessary. Therefore, another focus of the thesis is the implementation of the FOPA as mid-link OPC device for fiber nonlinearity compensation of 28-GBd PDM 16-QAM signal transmission. The experiments will be conducted for single-channel and for a five-channel 50-GHz spaced WDM system in (i) a dispersion-compensated link utilizing lumped amplification by EDFAs and, (ii) a dispersion-uncompensated link with backward-pumped Raman amplification. The investigated FOPAs are to be operated in the linear (small-signal gain) or unsaturated pump regime unless stated otherwise.

### 1.3 Organization of the Thesis

**Chapter 2** introduces the reader to the fundamentals of advance modulation formats and coherent reception. The chapter discusses some commonly used modulation formats and it draws the attention on the importance of coherent detection in optical communication systems.

**Chapter 3** reviews the linear and nonlinear effects which accompanies signal transmission in optical fibers. It discusses linear effects such as chromatic dispersion and nonlinear effects which include SBS, stimulated Raman scattering, and Kerr nonlinearities in fibers.

**Chapter 4** introduces the fundamentals of FOPA. It contains a discussion on the various types of FOPA such as single- and dual-pump FOPA, polarization-dependent and polarization-independent FOPA. The later part of the chapter explains the importance of pumps counter-phasing (a technique to enhance the SBS threshold of a fiber and to suppress the transfer of pump phase-dithering tones on the conjugated signal copies) in a dual-pump FOPA.

**Chapter 5** demonstrates the realization of practical FOPA as a subsystem. Systematic characterization and system performance analysis of both polarization-dependent and polarization-independent FOPA based on the polarization-diversity loop scheme are also discussed in the chapter. In addition, the impact of pump distortion (in the polarization-diversity loop) on 28-GBd single-polarization QPSK

data signal is investigated.

**Chapter 6** highlights a systematic system performance evaluation of a dual-pump polarization-independent FOPA as OPC device for WDM applications. A  $5 \times 28$ -GBd PDM 16-QAM data signal is employed for the performance evaluation of the FOPA-based OPC device.

**Chapter 7** focuses on the implementation of polarization-independent FOPA, based on the polarization-diversity loop scheme, as OPC device for nonlinearity compensation of 28-GBd PDM 16-QAM data signals in a dispersion-compensated link with lumped amplification utilizing EDFAs. The performance of the fiber-based OPC for nonlinearity compensation is compared with that of DBP in the same link configuration. Finally, the use of the fiber-based OPC is also implemented in a dispersion-uncompensated link based on backward-pumped Raman amplification for nonlinearity compensation of  $5 \times 28$ -GBd PDM 16-QAM signals.

**Chapter 8** presents a summary of the important finding of the thesis. It further provides possible suggestions for future research with respect to the implementation of polarization-diversity loop-based FOPA as a subsystem with minimum degradation.

**Appendix A** gives insight into the fundamentals of numerical method, based on the split-step Fourier method, for solving the nonlinear Schrödinger equation. This is implemented for the purpose of digital back-propagation algorithm for nonlinearity compensation.



## Chapter 2

# Advanced Modulation Formats and Coherent Reception

One of the key solutions to the global data demand requires an increase in spectral efficiency of the optical network. Considering the limited optical bandwidth in optical fibers, higher-order modulation formats and coherent reception are essential requirements to increase the spectral efficiency. In order to generate higher-order modulation formats, a complex transmitter employing IQ-modulator(s) is/are necessary. The use of coherent reception is a convenient way to detect the transmitted multi-level modulation format. Coherent reception is also capable of compensating for linear distortions of the signal [69, 70].

In this chapter, a brief introduction to advanced modulation formats is discussed. In Section 2.2 and 2.3, direct detection and coherent detection schemes, respectively, are reviewed. Knowledge of the optical signal-to-noise ratio (OSNR) of the transmitted data signal is essential since it relates the quality of the signal. Thus OSNR measurement is also discussed in Section 2.4

### 2.1 Advanced modulation formats

Data modulation, in general, is achieved by adjusting any of the physical parameters of the electric field of the signal (e.g. amplitude, frequency, phase, and polarization). This is achieved with a modulator at the transmitter. The normalized complex information (i.e., symbol),  $\underline{A}(t)$ , can be given by:

$$\underline{A}(t) = a(t)\exp(j\varphi(t)) \quad (2.1)$$

Where  $a(t)$ , and  $\varphi(t)$  are the time-dependent amplitude and the time-dependent phase of the symbol. The real part of the symbol (i.e.,  $\Re\{\underline{A}(t)\} = a(t)\cos(\varphi(t))$ ) and imaginary part of the symbol (i.e.,  $\Im\{\underline{A}(t)\} = a(t)\sin(\varphi(t))$ ) are modulated independently. It is common to refer to the real and imaginary parts of the symbol, respectively, as the in-phase (I) and quadrature (Q) components. Thus an IQ-modulator is required for the modulation of both components. After modulation, using a monochromatic carrier wave of frequency  $\omega_0$  and neglecting the  $z$ -dependency and polarization, the electric field of the optical modulated signal at the output of the transmitter can be given as:

$$E(t) = \underline{A}(t)\sqrt{P_0} \cdot \exp(-j\omega_0 t) = a(t)\exp(j\varphi(t))\sqrt{P_0} \cdot \exp(-j\omega_0 t) \quad (2.2)$$

Where  $\sqrt{P_0}$  is the amplitude of the continuous wave (CW) signal and the normalized complex amplitude,  $\underline{A}(t)$ , is the complex envelope of the modulated optical signal with time dependent amplitude  $a(t)$  and phase  $\varphi(t)$ . Note that the product  $a^2(t) \cdot P_0$  represents the instantaneous signal power [71, p. 32]. In practice, the real part of the optical field is transmitted and it is given by:

$$E_s(t) = \Re\{\underline{A}(t)\sqrt{P_0} \cdot \exp(-j\omega_0 t)\} \quad (2.3)$$

At the receiver, the I and Q components are separated using, e.g. a coherent detection scheme, and the independent data signals are recovered. Figure 2.1 shows the I and Q representation of different modulation formats which are used in optical communication systems. The on-off keying (OOK) scheme is the simplest modulation format. It encodes binary amplitude modulation with one-bit per symbol. Thus the symbol rate is the same as the bit rate. The binary phase-shift keying (binary phase-shift keying (BPSK)) scheme encodes also one-bit per symbol but the BPSK is phase modulated. The quadrature phase-shift keying (quadrature phase-shift keying (QPSK)) scheme encodes two bits per symbol but the QPSK is phase modulated. The quadrature phase-shift keying

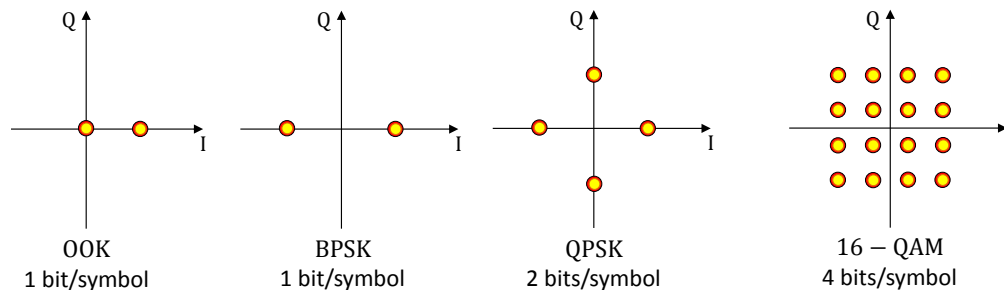


**Figure 2.1:** Constellation diagrams of some commonly used modulation formats.

(QPSK) and the 16-ary quadrature amplitude modulation (16-QAM) are multi-level modulation formats which incorporate both amplitude and phase modulation thereby having 2-bits per symbol and 4-bits per symbol, respectively. The QPSK has phase and constant amplitude modulation (similar to two BPSK signals on both the I and Q phases) whereas the 16-QAM has phase and multi-level amplitude modulation.

The bit rate and the symbol rate are related to each other by [72, p. 29]:

$$R_b = R_S \log_2 M \quad (2.4)$$

Where  $R_b$ ,  $R_S$ , and  $M$  are the bit rate, symbol rate, and the number of communication symbols (modulation order). The modulation order ( $M$ ) indicates the number of symbols or constellation points on the I and Q complex plane. More complex modulation formats such as 32-QAM, 64-QAM, have been reported [4]. The spectral efficiency (measured in bit/s/Hz/polarization) of an optical communication system is increased if the number of bits per symbol is increased. High number of bits per symbol can be achieved with higher-order modulation formats (e.g. see Figure 2.1), however higher OSNR is required for the higher-order modulation formats [4]. In addition, the spectral efficiency can be doubled if the data signals are on two orthogonal polarizations such as in polarization-division multiplexed (PDM) signals. WDM system with narrow channel spacing also increases the spectral efficiency [4].

## 2.2 Direct detection

The basic form of direct detection is the simplest receiver in optical communication systems and it is capable of detecting only amplitude modulated data (OOK signals). It is insensitive to the spectral characteristics (e.g. phase, wavelength) and the polarization state of the optical signal [73, p. 398]. With the implementation of a delay-line interferometer in the receiver circuitry, differential-phase modulated optical signal can be detected (without using a coherent detection technique). In such a scheme, a delay-line interferometer is implemented to create a phase difference of one symbol duration between adjacent symbols of the input signals in one of the branches of the interferometer [72, p. 47]. The differentially phase encoded information is then converted into amplitude information by destructive or constructive interference of successive symbols at the output of the interferometer prior to the detection by the photodiodes. Direct detection schemes are basically applicable to differentially phase-modulated signals, e.g.

differential binary phase-shift keying (DBPSK), differential quadrature phase-shift keying (DQPSK). A drawback of the direct detection scheme is to adapt or modify the receiver configuration when the symbol-rate or modulation format is changed.

## 2.3 Coherent detection

In contrast to direct detection techniques, coherent detection is sensitive to not only an optical signal's amplitude but its phase, frequency and polarization as well [72, 74]. Coherent detection techniques can be more complex relative to the direct detection techniques. The coherent detection techniques provide significant unparalleled advantages compared to direct detection. The advantages offered by digital signal processing (DSP)-based coherent reception include improved receiver sensitivity, frequency selectivity, and linear distortions cancellation such as chromatic dispersion [69, 74, 75] and polarization-mode dispersion (PMD) [76]. However, their compensation for nonlinear distortions is still under investigation [10, 77]. In coherent detection, an additional CW signal (usually at the receiver) is required and superimposed to the incoming data signal. This additional optical signal is known as local oscillator (LO).

A simple schematic representation of a single-polarization coherent detection scheme is shown in Figure 2.2. Here, a single-polarization data signal,  $E_s(t)$ , is received together with a tunable CW local oscillator (LO) in front of a  $2 \times 4$  (two inputs and four outputs)  $90^\circ$  optical hybrid. The  $90^\circ$  optical hybrid enables the mixing of the electric fields of the received signal and the LO. The coherent superposition of the two fields allows the I and Q components of any amplitude and/or phase modulated signal to be retrieved. This is achieved after the balanced photodetector (BPD) and by employing both analog-to-digital conversion and appropriate DSP algorithms.

$$E_s(t) = \Re\{\underline{A}_s(t)\sqrt{P_0} \cdot \exp[-j(\omega_0 t - \varphi_0)]\} \quad (2.5)$$

$$E_{LO}(t) = A_{LO}\exp[-j(\omega_{LO}t - \varphi_{LO})] \quad (2.6)$$

Equation (2.5) describes the electric field of the incoming optical data signal [78, p. 158]. The electric field of the LO can also be written as shown in equation (2.6).  $\underline{A}_s(t)$  is the complex amplitude of the data signal and  $A_{LO}$  is the amplitude

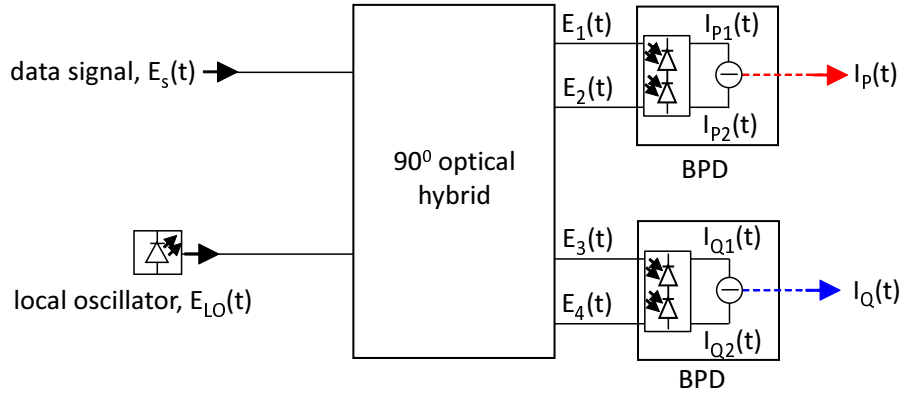


**Figure 2.2:** A schematic representation of a single-polarization coherent receiver front-end.

of the LO.  $\omega_0$  and  $\omega_{LO}$  are the angular frequencies of the carrier and the LO, respectively. Whereas  $\varphi_0$  and  $\varphi_{LO}$  are, respectively, the initial phases of the carrier and the LO. Note that the laser phase noise, the amplifier spontaneous emission (ASE) noise as well as shot noise and thermal noise of the photodiodes are neglected. The data signal and the LO are coherently superimposed in the hybrid as shown in Figure 2.2. The relationship between the input and output electric fields and the transfer function of a  $(2 \times 4)$   $90^\circ$  optical hybrid is given by [72, p. 101], [71, p. 63]:

$$\begin{bmatrix} E_1(t) \\ E_2(t) \\ E_3(t) \\ E_4(t) \end{bmatrix} = \frac{1}{2} \cdot \begin{bmatrix} 1 & 1 \\ 1 & j \\ 1 & -1 \\ 1 & -j \end{bmatrix} \cdot \begin{bmatrix} E_s(t) \\ E_{LO}(t) \end{bmatrix}$$

The four electric fields ( $E_1(t)$ ,  $E_2(t)$ ,  $E_3(t)$ , and  $E_4(t)$ ) at the output of the optical hybrid, after coherent superposition of the two waves, are given as:

$$E_1(t) = \frac{1}{2}(E_s + E_{LO}) \quad (2.7)$$

$$E_2(t) = \frac{1}{2}(E_s + jE_{LO}) \quad (2.8)$$

$$E_3(t) = \frac{1}{2}(E_s - E_{LO}) \quad (2.9)$$

$$E_4(t) = \frac{1}{2}(E_s - jE_{LO}) \quad (2.10)$$

The corresponding output photocurrent of all the four photodiodes can also be written as [72, p. 101]:

$$I_{P1}(t) = \frac{R}{2} \left[ P_0 \cdot a^2(t) + P_{LO} + 2a(t)\sqrt{P_0 P_{LO}} \cdot \cos(\Delta\omega t + \Delta\varphi + \varphi(t)) \right] \quad (2.11)$$

$$I_{P2}(t) = \frac{R}{2} \left[ P_0 \cdot a^2(t) + P_{LO} - 2a(t)\sqrt{P_0 P_{LO}} \cdot \cos(\Delta\omega t + \Delta\varphi + \varphi(t)) \right] \quad (2.12)$$

$$I_{Q1}(t) = \frac{R}{2} \left[ P_0 \cdot a^2(t) + P_{LO} + 2a(t)\sqrt{P_0 P_{LO}} \cdot \sin(\Delta\omega t + \Delta\varphi + \varphi(t)) \right] \quad (2.13)$$

$$I_{Q2}(t) = \frac{R}{2} \left[ P_0 \cdot a^2(t) + P_{LO} - 2a(t)\sqrt{P_0 P_{LO}} \cdot \sin(\Delta\omega t + \Delta\varphi + \varphi(t)) \right] \quad (2.14)$$

Where the intermediate frequency,  $\Delta\omega = \omega_0 - \omega_{LO}$  and the phase difference between the carrier and the LO is  $\Delta\varphi = \varphi_0 - \varphi_{LO}$ . The phase of the symbol is  $\varphi(t)$ . Whereas  $R$  is the responsivity of the photodiode and  $P_{LO} = |E_{LO}|^2$ . The output photocurrents after the balanced photodiodes (BPDs) yield either the in-phase or the quadrature current components and they are given by:

$$I_p(t) = I_{P1}(t) - I_{P2}(t) = 2a(t)R\sqrt{P_0 P_{LO}} \cdot \cos(\Delta\omega t + \Delta\varphi + \varphi(t)) \quad (2.15a)$$

$$I_Q(t) = I_{Q1}(t) - I_{Q2}(t) = 2a(t)R\sqrt{P_0 P_{LO}} \cdot \sin(\Delta\omega t + \Delta\varphi + \varphi(t)) \quad (2.15b)$$

Therefore, the complete information of the complex signal in equation (2.1) (i.e.,  $\underline{A}(t)$ ) can be recovered when the receiver reference frequency ( $\omega_{LO}$ ) and phase ( $\varphi_{LO}$ ) are locked to that of the carrier with appropriate digital signal processing (DSP) algorithms [75]. It is worth noting that for a polarization-multiplexed (PDM) signal, two 90° optical hybrids are used.

## 2.4 Optical signal-to-noise ratio (OSNR)

The optical signal-to-noise ratio (OSNR) provides a key performance indicator of a signal and it predicts also the bit-error ratio (BER) of the received signal. In WDM systems, it gives a per-channel assessment of signal quality. Its measurements involves measuring the total signal power in the passband of the channel under investigation and the ASE noise power over 0.1-nm (12.5-GHz, usually at 1550 nm) reference optical bandwidth ( $B_0$ ) of the ASE noise around the center wavelength of the measured optical signal. In order to take into consideration

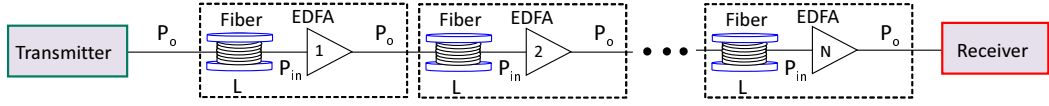


**Figure 2.3:** A representation of a point-to-point transmission link consisting of  $N$  fiber spans and  $N$  EDFAs.

the tilt in EDFA spectrum, the ASE around the signal channel are interpolated in order to obtain the in-band ASE noise power. In the transmission system as shown in Figure 2.3, each segment consists of a fiber span of length  $L$ , and an optical amplifier with a launch power of  $P_0$ . As the signal propagates over the link, each amplifier adds ASE noise after signal amplification. Neglecting the fiber span loss and assuming a quantum noise limited input signal, the input OSNR, in two polarizations, to the first EDFA in the link is given by [79]:

$$OSNR_{input} = \frac{P_{in}}{h\nu B_0} \quad (2.16)$$

Where  $h$  is the Planck's constant and  $\nu$  is the optical frequency of the signal. Considering a single EDFA with a gain of  $G$  and with a quantum noise-limited input signal with average optical power of  $P_{in}$ , the OSNR at the output of the EDFA, in two polarizations, is given by:

$$OSNR_{output} = \frac{P_0}{h\nu B_0 + P_{ASE}} = \frac{GP_{in}}{h\nu B_0 + P_{ASE}} \quad (2.17)$$

Where  $P_{ASE}$  is the added ASE noise power in two polarizations by the EDFA and it is given by [78, p. 305]:

$$P_{ASE} = 2n_{sp}(G - 1)h\nu B_0 \quad (2.18)$$

Where  $n_{sp}$  is the spontaneous emission factor (or the inversion factor) of the EDFA. Therefore the noise figure,  $F$ , of a single EDFA can be obtained from equations (2.16) and (2.17) as:

$$F = \frac{OSNR_{input}}{OSNR_{output}} = \frac{1}{G} [1 + 2n_{sp}(G - 1)] \quad (2.19)$$

Where  $OSNR_{input}$  and  $OSNR_{output}$  are the input and output optical signal-to-noise ratios of the amplifier. Usually, in a transmission system, as shown in Figure 2.3, the signal launch power at the output of an EDFA is set such that the signal gain compensates for the loss of the fiber span thus the output signal power ( $P_0$ ) before the receiver is the same as the input signal power before the

link. Taking the fiber span into consideration, the noise figure of a segment,  $F_{seg}$ , (i.e., a single span and a single EDFA) can be given as:

$$F_{seg} = 1 + 2n_{sp}(G - 1) = G \cdot F \quad (2.20)$$

Assuming the same specifications of the fiber spans and same gain and specifications for the EDFAs, the total noise figure,  $F_{tot}$ , of the entire transmission link is given by [79]:

$$F_{tot} = 1 + N \cdot (F_{seg} - 1) = 1 + 2N \cdot n_{sp}(G - 1) \quad (2.21)$$

Where  $N$ ,  $G$ , and  $F_{seg}$  are respectively the number of segments in the link, the amplifier gain, and the noise figure of a segment. For noise figures larger than one, the total noise figure,  $F_{tot} \approx N \cdot F_{seg}$ . The OSNR in front of the receiver (at the end of the transmission link) is given by:

$$OSNR|_{[dB]} = P_0|_{[dBm]} + 58 - 10 \cdot \log_{10}(N) - F_{seg}|_{[dB]} \quad (2.22)$$

Where,  $P_0$  is the output power of the signal before the receiver. Note that the 58 dBm accounts for quantum noise limitation in two polarizations considering noise bandwidth,  $B_0 = 12.5$  GHz at a center wavelength of 1550 nm (i.e.,  $h\nu B_0 = -58$  dBm).

Equations (2.17), (2.18), (2.19), and (2.21) indicate that the signal OSNR at the receiver can be increased by employing inline optical amplifiers with low noise figures, reducing the number of amplifiers in the link, or increasing the signal launch power per fiber span ( $P_0$ ). In addition, due to the relatively high loss of a transmission fiber span ( $\sim 20$  dB over 100 km of a standard fiber), the number of amplifiers is usually higher (i.e., more accumulated ASE noise) for long-haul transmission systems. Hence, it is customary to increase the signal launch power so as to maximize the receiver OSNR, however this approach has accompanied nonlinear distortion issues which will be addressed later in the thesis. For phase-insensitive optical amplifiers (i.e., amplifiers with only signal(s), without conjugated copies, at the input) with quantum-noise limited input signals, equation (2.19) shows that at high gain conditions ( $G \gg 1$ ) and for complete inversion ( $n_{sp} = 1$ ), the noise figure of the amplifier is  $F \approx 2$ . This indicates that phase-insensitive amplifiers have a quantum limited noise figure of 3 dB.

## **2.5 Summary**

Fundamentals of advanced modulation formats have been reviewed and also the direct detection and the coherent detection techniques have been discussed. It is convenient to detect advanced modulation formats with coherent detection, which is also capable of compensating for linear distortions. The optical signal-to-noise ratio (OSNR) in a transmission system has been briefly discussed in this chapter.



## **Chapter 3**

# **Linear and Nonlinear Effects in Optical Fibers**

The ability of an optical fiber to guide light (by the principle of total internal reflection) has contributed to the revolutionary data transmission provided by optical network technology in our world today. However, practical optical fibers have several associated problems, from its fabrication to its implementation. The fiber imperfections together with the undesired effects such as attenuation, dispersion, and nonlinear effects can significantly limit the efficiency of practical optical fibers.

This chapter focuses on the discussion of the properties of an optical fiber and some of the challenges associated with signal propagation in an optical fiber. Section 3.1 provides the fundamentals of a single-mode step-index fiber whereas in Section 3.2, particular attention is paid to the linear effects such as optical loss, chromatic dispersion, and birefringence, of optical fibers. Inelastic nonlinear effects resulting from Brillouin scattering and Raman scattering are discussed in Section 3.3.1. The elastic nonlinear effects due to the Kerr nonlinearities (self-phase modulation, cross-phase modulation, four-wave mixing) and the nonlinear Schrödinger equation (NLSE) are discussed in Section 3.3.2.

### **3.1 Introduction to optical fibers**

The optical fiber is a dielectric waveguide that operates at optical frequencies (in the Tera-Hertz range). The simplest form of an optical fiber consists of two different glasses in a cylindrical form as shown in Figure 3.1. The inner glass, usually known as core, is doped with a different material to increase the refrac-

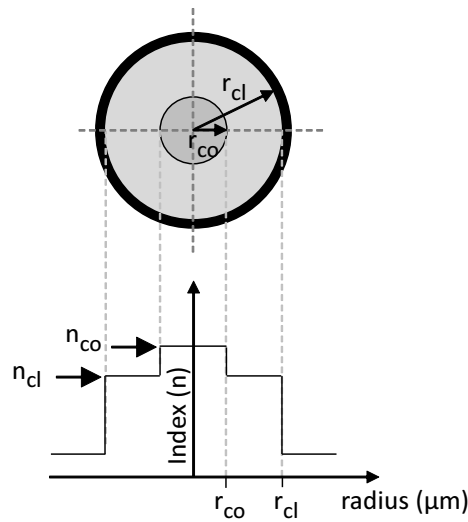


**Figure 3.1:** Schematic representation of the cross-section of a step-index fiber showing the refractive index profile over the radial distance of the core and cladding of the fiber.  $n_{cl}$  = cladding refractive index,  $n_{co}$  = core refractive index,  $r_{cl}$  = cladding radius,  $r_{co}$  = core radius.

tive index. The outer glass, also known as cladding, is doped to have a lesser refractive index than the core (i.e.,  $n_{co} > n_{cl}$ ). In practice, another material such as a plastic coating forms a jacket and it is implemented on the outer part of the cladding to protect the quartz fiber from damages and makes the fiber robust to bending.

Optical fibers are basically categorized as either single-mode fibers or multi-mode fibers. The single-mode fiber supports only the propagation of the fundamental mode in the optical fiber [78, p. 34], [79] whereas the multi-mode fiber supports the propagation of several modes [78, p. 34], [79]. Note that this thesis limits fiber discussions on only single-mode step-index fibers unless stated otherwise. Specifically, in a step-index fiber, the refractive index of the core is made higher than the refractive index of the cladding as also shown in Figure 3.1 [78, p. 25]. The physical phenomenon which governs the propagation of light in the optical fiber is the principle of total internal reflection [78, p. 24]. For instance, in the step index fiber, the higher refractive index of the core keeps the light wave in the core. In general, during manufacturing of an optical fiber, both the core and cladding are doped with different materials to alter their respective refractive indices. Germanium dioxide ( $\text{GeO}_2$ ) and Phosphorus pentoxide ( $\text{P}_2\text{O}_5$ ) are two of the most commonly used dopants to increase the refractive in-

dex whereas Fluorine (F) is used to decrease the refractive index [80, p. 60], [79]. In the drawing process, the preform is fed into a furnace and the soft glass (due to the heating) is pulled into a fiber. One essential parameter of an optical fiber which characterizes the number of modes supported by the fiber is the normalized frequency parameter usually known as  $V$ -parameter. The  $V$ -parameter is given by [78, p. 59]:

$$V = (2\pi r_{\text{co}}/\lambda) \cdot NA \quad (3.1)$$

Where  $r_{\text{co}}$  is the radius of the fiber core,  $\lambda$  is the wavelength of the fundamental mode and  $NA$  is the numerical aperture which is defined as:  $NA = \sqrt{n_{\text{co}}^2 - n_{\text{cl}}^2}$ . In order for the fundamental mode to propagate in a single-mode fiber,  $V$ -parameter must be less than 2.405 (i.e.,  $V < 2.405$ ) [78, p. 59].

Ideally, optical fibers should support light wave propagation to an infinite distance but linear effects such as attenuation and dispersion degrades the signal if these undesirable effects are not taken care off.

## 3.2 Linear effects in optical fibers

The linear properties of an optical fiber are those physical parameters which are independent of the intensity of the light wave propagating in the fiber and the refractive index of the fiber does not depend on the intensity of the optical wave. Fiber loss, fiber dispersion (e.g. chromatic dispersion and PMD), and polarization-dependent loss (PDL) are some of the linear effects in optical fibers.

### 3.2.1 Attenuation

Fiber loss, usually known as fiber attenuation, is one of the linear properties of an optical fiber. A low-loss optical fiber is made from fused silica glass ( $\text{SiO}_2$ ) and the attenuation coefficient ( $\alpha$ ) of silica fibers are typically 0.15 dB/km at 1550 nm. Note that in 2002, low attenuation fiber at a record 0.148 dB/km, at 1550 nm, has been reported [81]. The main sources of optical fiber attenuation are material absorption due to hydroxyl ions ( $\text{OH}^{-1}$ ) or the impurities in the fiber, Rayleigh scattering as a result of the random molecular structure of the silica glass. This leads to perturbations or random fluctuations in the refractive index which eventually scatter light in all directions [78, p. 58]. The evolution of the power of a bit stream propagating in an optical fiber is given by [78, p. 55]:

$$\frac{dP}{dz} = -\alpha \cdot P \quad (3.2)$$

Where  $\alpha$ ,  $P$ , and  $z$  are the attenuation coefficient of the fiber, average optical power, and length of the propagation distance, respectively. If  $P(0)$  is the input optical power, traveling over a fiber of length  $L$ , then the output optical power is obtained from equation (3.2) as:

$$P(L) = P(0)\exp(-\alpha \cdot L) \quad (3.3)$$

It is clear from equation (3.3) that the transmitted optical power decreases as it propagates over the transmission length of the fiber. The decrease of the input power in the fiber plays an essential role in optical transmission systems since the level of attenuation determines the maximum transmission distance of the signal. Thus signal amplification is a necessity for signal propagating in optical fibers especially at longer transmission distances. The unit of  $\alpha$  in equation (3.3) is usually expressed in 1/km, however, due to the convenience in handling simple computations in the logarithmic scale, the unit of the signal attenuation is usually stated in dB/km by fiber manufacturer's on data sheets. The conversion is given as [78, p. 56]:

$$\alpha(\text{dB/km}) = \frac{10}{L} \log_{10} \left[ \frac{P(L)}{P(0)} \right] \approx 4.343 \cdot \alpha \quad (3.4)$$

### 3.2.2 Chromatic dispersion

Another linear property of a glass fiber is chromatic dispersion and it plays a significant role in optical communication systems. For instance, in certain applications, such as parametric amplification (discussed in Chapter 4), near zero-dispersion is required in order to obtain a satisfactorily broad bandwidth of the amplifier. However, in WDM data transmission, nonlinear crosstalk among WDM channels can be significant in the presence of low dispersion. In a long transmission link, signal broadening in the time domain due to chromatic dispersion, causes inter-symbol interference and it has to be compensated for. Specifically, the chromatic dispersion of an optical fiber consists of two main dispersion parts which are the material dispersion and waveguide dispersion. The material dispersion occurs as a result of the dependency of the refractive index as a function of the wavelength [80, p. 97]. The waveguide dispersion, however, arises from the dependence of the fiber's waveguide properties on wavelength (i.e., dependency of fiber geometry and refractive index profile). In order to determine the chromatic dispersion in optical fiber, the propagation of a pulse with electric field vector,  $\mathbf{E}$ , with low intensity is considered. In general terms, there is a response

of induced electrical polarization of any dielectric medium under the influence of electric field and the optical glass fiber is no exception. This is described by the wave equation based on Maxwell's equations as [82, p. 32]:

$$\nabla \times \nabla \times \mathbf{E} = -\mu_0 \epsilon_0 \frac{\partial^2 \mathbf{E}}{\partial t^2} - \mu_0 \frac{\partial^2 \mathbf{P}}{\partial t^2} \quad (3.5)$$

Note that  $\mu_0 \epsilon_0 = 1/c^2$ . Where  $c$ ,  $\mu_0$ ,  $\epsilon_0$  are the speed of light, the permeability and the permittivity in vacuum and  $\mathbf{P}$  is the induced polarization of the medium due to the electric field. Generally, the induced polarization consists of a linear part,  $\mathbf{P}_L(\mathbf{r}, t)$ , and a nonlinear part,  $\mathbf{P}_{NL}(\mathbf{r}, t)$ , and it is given by [82, p. 32]:

$$\mathbf{P}(\mathbf{r}, t) = \mathbf{P}_L(\mathbf{r}, t) + \mathbf{P}_{NL}(\mathbf{r}, t) \quad (3.6)$$

Here,  $\mathbf{r}$  represents a position vector. As stated earlier, the consideration of the fiber in this case is under low intensity thus the nonlinear part of the induced polarization (which will be discussed later in this chapter under Section 3.3) is treated as very small perturbations and can be neglected. The linear part, however, is expressed as:

$$\mathbf{P}(\mathbf{r}, t) = \mathbf{P}_L(\mathbf{r}, t) = \epsilon_0 \int_{-\infty}^{\infty} \chi^{(1)}(\mathbf{t} - \mathbf{t}') \cdot \mathbf{E}(\mathbf{r}, \mathbf{t}') d\mathbf{t}' \quad (3.7)$$

Where  $\chi^{(1)}(t)$  is the linear susceptibility of the medium and the relationship between the frequency-dependent susceptibility,  $\tilde{\chi}^{(1)}(\omega)$ , and frequency-dependent relative permittivity,  $\epsilon_r(\omega)$ , is given by [82, p. 33]:

$$\epsilon_r(\omega) = 1 + \tilde{\chi}^{(1)}(\omega) \quad (3.8)$$

Where  $\tilde{\chi}^{(1)}(\omega)$  is the Fourier transform of  $\chi^{(1)}(t)$ . The frequency-dependent susceptibility of an electromagnetic wave in a dielectric medium is a complex entity and so is the frequency-dependent permittivity. The real and imaginary parts of the frequency-dependent permittivity are related to the frequency-dependent refractive index,  $n(\omega)$ , and the frequency-dependent attenuation coefficient,  $\alpha(\omega)$ . As a result of the low attenuation of an optical fiber in the wavelength range of interest (around 1.3  $\mu\text{m}$  and 1.55  $\mu\text{m}$ ), the imaginary part of the permittivity is much smaller than the real part [82, p. 34]. Therefore  $\epsilon_r(\omega) = n^2(\omega)$ . Furthermore, in a homogeneous medium, the frequency-dependent refractive index,  $n(\omega)$ , is independent of the spatial coordinates of the core and cladding. Equation (3.5) can be re-written in the frequency domain as [79]:

$$\nabla^2 \tilde{\mathbf{E}} + n_i^2(\omega) k_0^2 \tilde{\mathbf{E}} = 0 \quad (3.9)$$

Here  $i = 1, 2$  with  $n_1 = n_{co}$ ,  $n_2 = n_{cl}$  and  $\tilde{\mathbf{E}}$  is the Fourier transform of  $\mathbf{E}$ . The wave number in vacuum,  $k_0 = \omega\sqrt{\mu_0\epsilon_0} = 2\pi/\lambda_0$ . Assuming weakly guiding waveguide (i.e.,  $n_{cl} < n_{eff} < n_{co}$ ), where  $n_{eff}$  is the effective index of refraction, the Helmholtz equation (i.e., equation (3.9)) yields two solutions for two orthogonal polarizations. For instance taking an electric field polarized in the  $x$ -direction and propagating in the  $z$ -direction, the solution of equation (3.9) in the frequency domain is given by [82, p. 42]:

$$\tilde{\mathbf{E}}_x(r, \omega) = F(x, y)\tilde{A}(0, \Delta\omega)\exp[j\beta(\omega)z] \quad (3.10)$$

Where  $F(x, y)$  is the transverse modal profile of the wave propagating along the fiber and  $\Delta\omega = \omega - \omega_0$ . Note that  $\omega_0$  is the angular center frequency of a quasi-monochromatic carrier optical wave of width  $\Delta\omega$ .  $\tilde{A}(0, \Delta\omega)$ , is the initial field complex amplitude of the slowly varying envelope ( $\tilde{A}(z, \Delta\omega)$ ) of the wave,  $\tilde{E}_x(r, \omega)$ . The propagation of a frequency component at  $\omega$  is determined by the propagation constant,  $\beta(\omega)$ , and considering a narrow range of frequencies about a center frequency,  $\omega_0$ , one can expand  $\beta(\omega)$  using Taylor's series around a reference frequency,  $\omega_0$ , as:

$$\beta(\omega) = k_0 n_{eff}(\omega) = \beta_0 + (\omega - \omega_0)\beta_1 + \frac{(\omega - \omega_0)^2}{2}\beta_2 + \frac{(\omega - \omega_0)^3}{6}\beta_3 + \dots \quad (3.11)$$

$$\beta_m(\omega) = \left. \frac{\partial^m \beta}{\partial \omega^m} \right|_{\omega=\omega_0} \quad (3.12)$$

Where  $m = 0, 1, 2, 3, \dots$  and  $\beta_0$  is a constant phase shift which is frequency-independent. The first-order dispersion,  $\beta_1$ , is also known as group delay per length and it is related to the group velocity,  $v_{gr}$ , from the relation [79]:

$$v_{gr} = \left( \frac{d\beta}{d\omega} \right)^{-1} = \left( \frac{d(k_0 n_{eff}(\omega))}{d\omega} \right)^{-1} = \frac{1}{\beta_1} \quad (3.13)$$

$\beta_2$  is the second-order dispersion (also known as group velocity dispersion (GVD) or the chromatic dispersion) and it is related to the dispersion parameter,  $D$ , from the relation [79]:

$$D = \left( \frac{d\beta_1}{d\lambda} \right) = -\frac{2\pi c}{\lambda^2}\beta_2 = -\frac{\lambda}{c} \cdot \frac{d^2 n_{eff}(\lambda)}{d\lambda^2} \quad (3.14)$$

Usually, a term *normal dispersion* is often used when the dispersion parameter,  $D$ , is negative (i.e., when  $\beta_2 > 0$ ). However, *anomalous dispersion* occurs when  $D$  is positive (i.e., when  $\beta_2 < 0$ ) and the wavelength at which  $\beta_2 = 0$  is referred

to as zero-dispersion wavelength ( $\lambda_{zd}$ ). The third-order dispersion ( $\beta_3$ ) is related to the dispersion slope,  $S$ , by:

$$S = \left( \frac{dD}{d\lambda} \right) = \frac{4\pi c}{\lambda^3} \beta_2 + \left( \frac{2\pi c}{\lambda^2} \right)^2 \beta_3 \quad (3.15)$$

Usually, the dispersion slope is significant in systems with high data rates [83] whereas the chromatic dispersion is the main dispersion parameter creating major signal impairments in long-haul transmission systems and even at lower data rates. The fourth-order dispersion,  $\beta_4$ , and the remaining higher terms can be obtained by differentiating the preceding dispersion term as shown in equation (3.12).

### 3.2.3 Polarization mode dispersion (PMD)

A single-mode fiber inherently supports two orthogonal polarization modes (e.g.  $x$ - and  $y$ -polarizations) which basically forms the principal axes (vertical and horizontal) of the fiber. Therefore in a perfect symmetric and stress-free core, the orthogonal modes are degenerate (i.e., they have the same propagation constant). However, imperfections in the fiber core, during the drawing process, random variations in the core shape and external stress result in random coupling of the two polarization states [78, p. 44]. The two orthogonal polarizations of the signal experience different propagation constants and therefore travel at different speeds. This eventually leads to pulse broadening as shown in Figure 3.2. The polarization axes of the fiber are then referred to as *fast axis* (axis with lower refractive index) and *slow axis* (axis with higher refractive index). This property of a fiber exhibiting different refractive indices on the principal axes is known as birefringence,  $B$ , as shown in Figure 3.2 and it is given as [82, p. 14]:

$$B = \frac{|\beta_x - \beta_y|}{k_0} = \frac{|\Delta\beta|}{k_0} = |n_x - n_y| = \frac{\lambda}{L_B} \quad (3.16)$$

Where  $n_x, n_y$  are the refractive indices of the two orthogonal polarizations, and  $L_B$  is the beat length of the fiber. Considering a short piece of an optical fiber (i.e., uniform birefringence), the differential group delay (DGD), which is also the absolute time delay ( $|\Delta\tau|$ ) between the two orthogonal polarization states of the fiber, scales linearly with the length of the fiber and it is given by [84, p. 5]:

$$|\Delta\tau| = \frac{L}{v_{gr}} \quad (3.17)$$

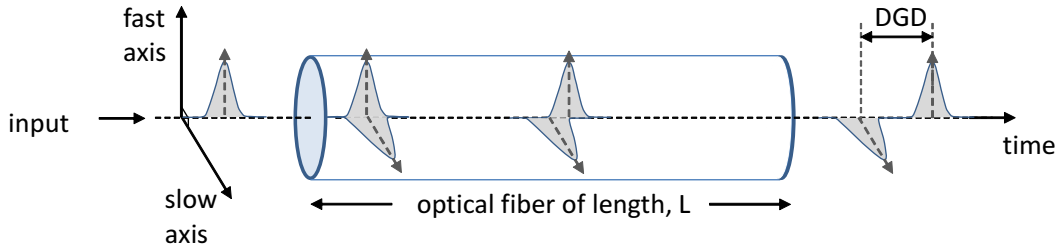


**Figure 3.2:** Pulse propagation in a single-mode fiber which has slightly different refractive indices of the two orthogonal principal axes (fast and slow axis) leading to DGD (between the polarization components) and eventually pulse broadening.

From equations (3.13), (3.16) and (3.17),  $|\Delta\tau|$  can be written as:

$$|\Delta\tau| = L \cdot \frac{d(\Delta\beta)}{d\omega} = L \cdot \frac{d(k_0 B)}{d\omega} \quad (3.18)$$

It can be seen from equation (3.18) that  $|\Delta\tau|$  (or DGD), is a measure of the birefringence,  $B$ . However, longer fibers can be approximated as a concatenation of short pieces of fiber lengths [59, p. 214]. The birefringence is no longer constant but it becomes a function of location of the fiber. The average DGD (i.e.,  $\langle DGD \rangle$ ) scales with the square root of the length of the fiber and it is given by [84, p. 6]:

$$\langle DGD \rangle = D_p \cdot \sqrt{L} \quad (3.19)$$

Where the constant of proportionality,  $D_p$ , is the PMD coefficient parameter and it is measured in  $ps/\sqrt{km}$ . Note that the PMD is a measure of the average DGD (i.e.,  $PMD = \langle DGD \rangle$ ). Since the PMD has  $\sqrt{L}$  dependence, its impact on pulse broadening of lower data rates propagating over short transmission length is small compared with chromatic dispersion (GVD) effects. However, for higher data rates and also in long-haul transmission systems, the impact of PMD can be very significant. In addition, PMD does not only lead to pulse broadening but also causes random variation of the state of polarization of any optical field propagating through the fiber due to its dependence on the local birefringence [78, p. 45]. In order to avoid the random variation of the state-of-polarization of a signal in a fiber, large amount of birefringence is intentionally introduced into the fiber during manufacturing, through fiber design modifications (e.g. polarization-maintaining fibers) [82, p. 15]. Any optical signal that is aligned

in polarization to one of the principal axis of a polarization-maintaining fiber is preserved as the signal propagates along the fiber [82, p. 15].

### 3.3 Nonlinear effects in optical fibers

In Section 3.2.2, it was discussed that the induced electrical polarization which is generated as a result of a dielectric material under the influence of electric field ( $\mathbf{E}$ ) has both linear and nonlinear terms. The total induced dielectric polarization,  $\mathbf{P}$ , can be written as [82, p. 17]:

$$\mathbf{P} = \epsilon_0 \left( \chi^{(1)} \cdot \mathbf{E} + \chi^{(2)} : \mathbf{E}\mathbf{E} + \chi^{(3)} : \mathbf{E}\mathbf{E}\mathbf{E} + \dots \right) \quad (3.20)$$

Where  $\chi^{(1)}$ ,  $\chi^{(2)}$ , and  $\chi^{(3)}$  are the first-order, second-order, and third-order susceptibilities. The linear susceptibility,  $\chi^{(1)}$ , (first-order susceptibility) is the most dominant effect of the total induced polarization. Its effects are included through the refractive index and the attenuation coefficient of the fiber.  $\chi^{(2)}$  exists also in non-centrosymmetric media such as PPLN and it is responsible for nonlinear effects such as difference-frequency generation (DFG). It vanishes in fused silica glass due to the symmetry of the silica molecule. Thus  $\chi^{(3)}$  becomes the lowest-order nonlinear effect in optical fibers. The nonlinear effects in fibers can be classified as elastic or inelastic. Specifically, the real part of  $\chi^{(3)}$  is the elastic nonlinear term which is known as Kerr nonlinearity, whereas the imaginary part of  $\chi^{(3)}$  constitutes the inelastic nonlinear effects (e.g. stimulated Brillouin and Raman scattering) [59, p. 38].

#### 3.3.1 Inelastic nonlinear effects

During inelastic nonlinear interactions in a dielectric medium, there is an energy exchange between the electromagnetic field and the dielectric medium. Two phenomena constitute this kind of nonlinear effects in optical fibers and they are: stimulated Brillouin scattering (SBS) and stimulated Raman scattering (SRS).

#### Brillouin scattering

Brillouin scattering occurs as a result of interaction between an incident optical wave and acoustic vibration (acoustic phonons) in the optical fiber. The acoustic vibration is generated as a result of electrostriction (variation of medium shape or density due to electric field). This causes frequency down-conversion of the

optical wave (also known as back-scattered wave or the Stokes shift) typically at 10 GHz. Specifically, the generated acoustic wave travels in the same direction as the optical wave in the forward direction and this produces a narrow band gain for optical frequencies traveling in opposite direction, therefore depleting the forward traveling optical wave [78, p. 59]. The Brillouin gain bandwidth is generally different for different fibers and can be up to 100 MHz [78, p. 59] (e.g.  $\sim 20$  MHz for Ge-doped fibers). Brillouin scattering can either be a stimulated or a spontaneous effect. The spontaneous Brillouin scattering occurs even if the intensity of the incident optical wave is weak and it is caused by the thermal effect, due to the field, in the dielectric medium. It is the first occurrence of the Brillouin process as it initiates the stimulated Brillouin scattering (SBS) (i.e., at high intensities, the scattering light exhibits a stimulated feature and it is known as SBS).

Usually the reflected power from a fiber consists of both SBS and Rayleigh scattering. Remark that investigation of Rayleigh scattering is not the primary focus of the thesis thus much emphasis will not be placed on this effect. Considering the reflected power from a fiber as shown in Figure 3.3, it can be seen that the back-scattered light grows linearly at lower input powers but rises exponentially at high input powers. The linear increase at lower power levels of the asymptotic curve of the back-scattered power is mainly dominated by Rayleigh back-scattering whereas the SBS dominates where the curve deviates from the linear regime. The reflected power from a fiber cannot be higher than the input power, therefore in Figure 3.3, the reflected power again grows linearly with the higher input powers (above the SBS threshold) once its value equals the input power (neglecting the loss of the fiber). This tendency causes the output power of the fiber to saturate at higher input powers (not shown in Figure 3.3). Note that an experimental measurement of SBS is presented in Chapter 5 Section 5.1.1.

To quantify the power level at which the Brillouin back-scattering becomes significant, a parameter namely SBS threshold is used. The SBS threshold,  $P_{th}$ , of a fiber has been estimated differently in literature [57, 85–87]. In this thesis, the SBS threshold is estimated as the input power at which the back-scattered light from a fiber is 1% of the input power into the fiber [85]. Generally, the SBS threshold is defined as [88, 89]:

$$P_{th} = \frac{21CA_{eff}}{g_B L_{eff}} \left( 1 + \frac{\Delta\nu_p}{\Delta\nu_B} \right) \quad (3.21)$$

Where  $A_{eff}$  is the effective mode area of the fiber and the constant  $C$  is either one

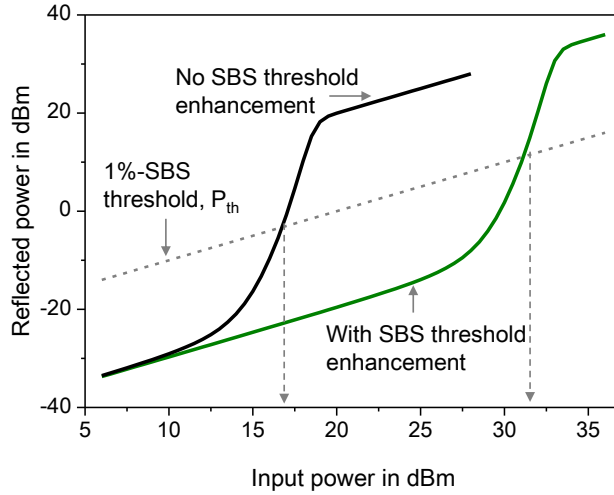


**Figure 3.3:** Simulated SBS threshold of a 300 m fiber showing the reflected power at a given input power with and without SBS suppression implementation.

or two if the optical wave is single-polarization or dual-polarization signal, respectively.  $g_B$  is the Brillouin gain coefficient and for silica fibers,  $g_B \approx 5 \times 10^{-11}$  m/W.  $\Delta\nu_p$  is the line-width of the forward optical wave.  $\Delta\nu_B$  is the SBS gain-bandwidth, and  $L_{eff}$  is the effective length of the fiber. The effective length is the fiber length at which the optical power is assumed to be constant (nonlinear interaction is maximum) and it is expressed as [78, p. 554]:

$$L_{eff} = \frac{1 - \exp(-\alpha L)}{\alpha} \quad (3.22)$$

Where  $L$  and  $\alpha$  are the total length and linear attenuation coefficient, respectively, of the fiber. The effective mode area is obtained from the transverse modal field distribution in equation (3.10) and it is given by [59, p. 35]:

$$A_{eff} = \frac{\left( \int \int_{-\infty}^{\infty} |F(x,y)|^2 dx dy \right)^2}{\int \int_{-\infty}^{\infty} |F(x,y)|^4 dx dy} \quad (3.23)$$

Recall that  $F(x,y)$  is the transverse modal field distribution. In order to minimize the Brillouin back-scattering, several schemes have been reported. For instance, it can be seen from equation (3.21) that reducing the fiber length will increase the SBS threshold and this has been shown in [90, p. 285]. Note that reducing the fiber length indicates a reduction of the interaction length of the fiber. Application of a linear or stepwise temperature gradient along the fiber also has the tendency to increase the SBS threshold [91]. The SBS threshold can also be increased by applying a strain on the fiber [92]. However, both temperature and strain can alter the dispersion of the fiber [93, 94] and may not

be appropriate for many application which rely on stable dispersion. Another scheme involves the division of the used fiber into several sections and individual optical isolators are placed between the sections [95]. It has been shown that doping the core of a silica fiber with aluminum instead of germanium increases the SBS threshold. Aluminum raises the refractive index and lowers the acoustic wave whereas germanium raises both the refractive index and the acoustic wave [94, 96, 97]. However, aluminum-doped fibers have very high attenuation (e.g. 6 dB/km) [97]. Phase-modulation of the input optical wave is also a well-known scheme to enhance the SBS threshold [98]. Increasing the line-width of the input beam,  $\Delta\nu_p$ , increases the SBS threshold,  $P_{th}$  of the fiber as can be seen from equation (3.21). The dispersion of the used fiber are not affected by phase-modulation of the input optical beam, thus this scheme is the preferred choice for SBS threshold enhancement in the thesis.

### **Stimulated Raman scattering**

Stimulated Raman scattering (SRS) occurs in fibers when there is a nonlinear interaction between an input light and molecular vibrations of the fiber (optical phonons). This effect can cause a power transfer from the optical field to another field whose frequency is downshifted (Stokes wave) by an amount determined by the vibrational modes of the medium [82, p. 298]. Similar to SBS, Raman scattering has a threshold but its value is nearly 1000 times higher compared to SBS. While SBS amplifiers reflect light which is 10 GHz shifted from the forward wave, SRS amplifies both forward and backward optical waves which are inside the Raman amplification gain-bandwidth. The gain-bandwidth of a single-pump Raman amplifier extends over a large frequency range (up to 40 THz) with a peak gain located at a 13-THz lower frequency relative to the high power optical wave [82, p. 299]. The bandwidth with a significant gain (useable bandwidth for amplification in practice) is about 6 THz. In WDM systems, the Raman effect manifests itself when shorter wavelengths feed power to the longer wavelength channels. Raman amplification in a transmission system can be obtained by lumped amplification (i.e., discrete amplifier) or by distributed amplification (when the entire transmission fiber is used as the amplification medium) [99]. Distributed Raman amplification (DRA) has been shown to provide better OSNR and better signal power-symmetry relative to the center of a transmission span than lumped amplification. Near-ideal power-length symmetry can be achieved by using both forward and backward pumping [99]. However, backward-pumped

distributed Raman amplification is often used since the configuration minimizes the transfer of pump intensity noise to the amplified signal [99]. As a result of the near-ideal power-length symmetry of distributed Raman amplification, the combination of Raman amplifiers and optical phase conjugation (OPC) are used for Kerr nonlinearity compensation in optical transmission systems. Further explanation and implementation of using distributed Raman amplification for nonlinearity compensation is discussed in Chapter 7.

### 3.3.2 Elastic nonlinear effects

Other nonlinear effects limiting the performance of optical transmission systems are the elastic nonlinear effects. They are due to a modulation of the refractive index of the fiber at high optical powers. Therefore the effects are usually known as intensity-dependent refractive index nonlinear effects. They are also referred to as the optical Kerr effect [59, p. 183]. Three fundamental nonlinear effects constitute the Kerr nonlinearity, and they are: self-phase modulation (SPM), cross-phase modulation (XPM), and four-wave mixing (FWM). The intensity-dependent nonlinear refractive index,  $n'$ , is given by [82, p. 18]:

$$n' = n_0 + n_2|\mathbf{E}|^2 \quad (3.24)$$

Where  $n_0$  is the linear refractive index and  $n_2$  is the nonlinear refractive index coefficient which is related to the real part of the third-order nonlinear susceptibility,  $\chi^{(3)}$ , by the relation [82, p. 41]:

$$n_2 = \frac{3}{8n_0}\Re\{\chi^{(3)}\} \quad (3.25)$$

Typical values for the nonlinear refractive index term,  $n_2$ , are usually in the range of  $2.2 \times 10^{-20} \text{ m}^2/\text{W}$  to  $3.9 \times 10^{-20} \text{ m}^2/\text{W}$ . The wide variation of the  $n_2$  values depends on the fiber type (i.e., used dopants) and the measurement technique [59, p. 431]. The electric field in equation (3.20) can be written as:

$$\mathbf{E}(z, t) = \Re\{A(z, t)\exp[-j(\omega_0 t - \beta_0 z)]\} \quad (3.26)$$

The slowly varying envelope,  $A(z, t)$ , is given by:

$$A(z, t) = \frac{1}{2\pi} \int_{-\infty}^{\infty} \tilde{A}(z, \Delta\omega)\exp[j\beta(\omega)z - j\beta_0 z]d(\Delta\omega) \quad (3.27)$$

Where  $\tilde{A}(z, \Delta\omega)$  is the Fourier transform of  $A(z, t)$  and  $\Delta\omega = \omega - \omega_0$ . Substituting  $\beta(\omega)$  with Taylor expansion yields an equation given by [59, p. 35]:

$$\frac{\partial A(z, T)}{\partial z} = \underbrace{-\frac{\alpha}{2}A(z, T) - j\frac{\beta_2}{2}\frac{\partial^2 A(z, T)}{\partial T^2} + \frac{\beta_3}{6}\frac{\partial^3 A(z, T)}{\partial T^3}}_{\text{Linear}} + \underbrace{j\gamma|A(z, T)|^2 A(z, T)}_{\text{Nonlinear}} \quad (3.28)$$

$$\gamma = \frac{2\pi n_2}{\lambda_0 A_{eff}} \quad (3.29)$$

Equation (3.28) is the so called nonlinear Schrödinger equation (NLSE) and it describes the field evolution of a light propagating in an optical fiber [82, p. 44]. In equation (3.28), the variable  $T = t - z \cdot \beta_1$  and it is the retarded time frame which is moving at a group velocity of the envelope of the field. The NLSE consists of two parts: the linear part and the nonlinear part. The linear part takes in account the attenuation coefficient and dispersion parameters of the fiber. The nonlinear term, relates the intensity,  $|A(z, T)|^2$ , and the nonlinear coefficient,  $\gamma$ . The nonlinear coefficient is defined in equation (3.29). Where  $A_{eff}$  is the effective mode area of the fiber (see equation (3.23)) and  $\lambda_0$  is the operating wavelength of the optical beam in the fiber.

### Self-phase modulation (SPM)

Self-phase modulation (SPM) is a single-channel nonlinear effect and it manifests itself in an optical fiber at high intensities. The optical intensity modulates the refractive index of the medium and eventually causes a nonlinear phase delay of the optical pulse itself. The phase of a monochromatic optical field changes by [82, p. 18]:

$$\Delta\varphi = n'k_0 L_{eff} = (n_0 + n_2|E|^2)k_0 L_{eff} \quad (3.30)$$

The nonlinear phase shift ( $\Delta\varphi_{SPM}$ ) generated by the pulse itself is given by:

$$\Delta\varphi_{SPM} = n_2 k_0 L_{eff} |E|^2 = \frac{2\pi n_2}{\lambda_0} \frac{P}{A_{eff}} L_{eff} = \gamma P L_{eff} \quad (3.31)$$

Where  $P$  is the input optical power of the propagating light wave in the fiber.

### Cross-phase modulation (XPM)

Cross-phase modulation (XPM) occurs in optical fibers when more than one optical wave is present in the fiber at high intensity conditions. For instance, when two optical fields, polarized in the  $x$ -direction and with frequencies  $\omega_1$  and  $\omega_2$ ,

propagate along a fiber, both fields will cause a change in the refractive index and will eventually cause a phase shift on the other optical wave. The total nonlinear phase shift,  $\Delta\varphi_{NL}$ , seen by the field at  $\omega_1$  is given by [82, p. 19]:

$$\Delta\varphi_{NL} = n_2 k_0 L_{eff} (|E_1|^2 + 2|E_2|^2) \quad (3.32)$$

Thus the optical field at  $\omega_1$  experiences a phase shift from two different contributions. The first term in equation (3.32) ( $n_2 k_0 L_{eff} |E_1|^2$ ) is the SPM of the optical wave itself due to its amplitude,  $E_1$ . The second term in equation (3.32) describes the XPM (i.e.,  $\Delta\varphi_{XPM} = 2n_2 k_0 L_{eff} |E_2|^2$ ) as a result of the field at  $\omega_2$ . This is known as inter-channel XPM. For equally intense optical fields for different wavelength, the phase-shift due to XPM is twice the phase-shift due to SPM. Depending on the signal power levels, both inter- and intra-channel XPM may lead to significant signal degradation.

#### Four-wave mixing (FWM)

When at least two optical fields at different optical frequencies propagate in an optical fiber, the interaction between the different optical fields generate a new optical wave at another frequency. This effect is known as four-wave mixing (FWM). The efficiency of FWM is dependent on the instantaneous powers of the interacting waves, frequency separation and the relative phase of the waves. For instance, three optical waves of frequencies  $\omega_{p1}$ ,  $\omega_{p2}$  and  $\omega_s$  propagate in a fiber, the interaction among the optical waves will generate new optical waves as shown in Figure 3.4. In the event where  $\omega_{p1} \neq \omega_{p2} \neq \omega_s$ , a special type of FWM has occurred and the process is known as non-degenerate FWM. However, a degenerate FWM is said to occur when  $\omega_{p1} = \omega_{p2} \neq \omega_s$ . Thus any combination of the input waves can generate new frequencies, except when  $\omega_{p1} = \omega_{p2} = \omega_s$ , and an example is given by [59, p. 370]:

$$\omega_i = \omega_{p1} + \omega_{p2} - \omega_s \quad (3.33)$$

Where  $\omega_i$  is the frequency of the generated optical wave. Equation (3.33) indicates that two photons (one each) are lost from the optical waves at  $\omega_{p1}$  and  $\omega_{p2}$  and new optical waves at frequencies,  $\omega_s$  and  $\omega_i$ , are simultaneously created by the lost photons. This is only possible when the total energy and momentum are conserved [82, p. 343]. The momentum-conservation requirement leads to phase-matching condition, which must be satisfied for FWM to take place [82, p. 343]. This will be discussed in detail in Chapter 4. Similar to intra-channel XPM,

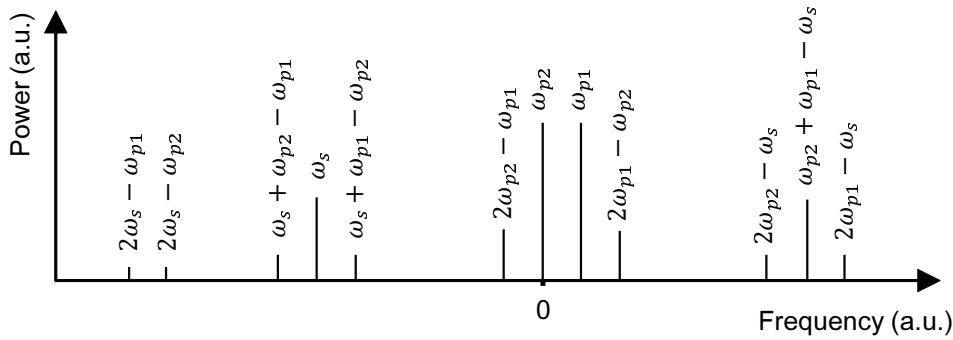


**Figure 3.4:** Generation of new frequency components due to FWM of three input optical waves of frequencies  $\omega_{p1}$ ,  $\omega_{p2}$  and  $\omega_s$  [1].

the spectral components of a single-channel pulse can interact with each other to generate new optical frequencies and the effect is known as intra-channel FWM. Both intra- and inter-channel FWM also lead to significant signal distortions. Nevertheless, FWM can be very useful in optical transmission systems especially in parametric processes in optical fibers.

### 3.4 Summary

In this chapter, a review of the fundamental principles of optical fiber have been discussed. Linear attenuation and dispersion in optical fibers have been briefly explained. Polarization mode dispersion (PMD) and birefringence fluctuation often lead to polarization rotation in a fiber. Implementation of a polarization maintaining fiber can reduce the impact of birefringence fluctuations. Inelastic nonlinear scattering (i.e., Brillouin and Raman scattering) and elastic scattering (Kerr effects) have been theoretically considered. Stimulated Brillouin scattering (SBS) reduces the amount of output power that can be achieved for a given input power into an optical fiber. Different schemes such temperature or strain gradient along the fiber can reduce the SBS thus increasing the SBS threshold. Spectral width broadening of the input optical signal is another scheme that can suppress the degree of SBS. The optical Kerr effects can lead to nonlinear phase distortion of optical signals propagating in a fiber.

## Chapter 4

# Fundamentals of Fiber-based Optical Parametric Amplifier

The fiber-based optical parametric amplifiers (FOPAs) exhibit numerous promising features which make them essential candidates for potential applications in high-speed optical communication systems. Compared to the high noise figure and the limited bandwidth of the already existing amplification technologies (e.g. EDFA), FOPAs have high gain [53] and broad bandwidth [55, 100]. In addition, FOPAs exhibit spectral inversion, ultra-fast (femtosecond scale) response and low noise amplification [56, 101]. Therefore, they can be useful for in-line amplification with low noise figure and optical phase conjugation for nonlinearity compensation. They are also applicable for wavelength conversion and high-speed optical signal processing which include all-optical regeneration and optical sampling [1].

Usually, special types of single-mode fibers with a small core diameter (typically  $\sim 4\mu\text{m}$ ) are used. These fibers are popularly known as highly nonlinear fibers (HNLFs). As a result of their small core diameter, they tend to have higher nonlinear coefficient, typically between  $10 \text{ /}(\text{W}\cdot\text{km})$  and  $20 \text{ /}(\text{W}\cdot\text{km})$ , which is about ten times higher than that of standard fibers which have a nonlinear coefficient of about  $1.3 \text{ /}(\text{W}\cdot\text{km})$ . The underlying physical phenomenon governing the operation of FOPA is four-wave mixing which is inherently polarization dependent [102, 103]. Therefore the basic form of FOPAs, which is polarization-dependent, is not capable for practical implementation in optical communication systems. This is due to the random nature of the state-of-polarization of a signal propagating in a transmission link. Furthermore, in order to use the FOPA for WDM systems, a broad and flat gain-bandwidth is a prerequisite.

This chapter reviews the fundamental operation of a FOPA based on different configurations. The basic configurations of a polarization-dependent FOPA for both single-pump and dual-pump are discussed in Section 4.2. The theoretical background of both single-pump and dual-pump polarization-independent FOPA configurations are presented in Section 4.3. Orthogonally polarized pumps and polarization - diversity schemes are also discussed in Section 4.3. In Section 4.4, the impact of pump-induced distortions on signals and ways to minimizing them are also discussed.

## 4.1 Phase-matching in FOPAs

Parametric amplification in fibers makes use of FWM which relies on the third-order nonlinear susceptibility to generate signal copies (also known as idlers) of the input signals. For efficient FWM, phase-matching between the interacting waves is necessary and this depends on two conditions which should be satisfied: conservation of energy and conservation of momentum [82, p. 343]. A perfect phase-matching condition is achieved when the phase mismatch parameter is approximately zero [59, p. 370]. For instance, if two high power signals (also known as pumps) at frequencies  $\omega_{p1}$  and  $\omega_{p2}$  and a signal at a frequency of  $\omega_s$  are input into a HNLF. The energy conservation as a result of the elastic nonlinear process in the HNLF can be written as:

$$\omega_s + \omega_i = \omega_{p1} + \omega_{p2} \quad (4.1)$$

Where the generated, idler, frequency is  $\omega_i$ . The phase-matching condition for this process is  $\Delta\beta \approx 0$  (from the conservation of momentum) where:

$$\Delta\beta = \beta_s + \beta_i - \beta_{p1} - \beta_{p2} \quad (4.2)$$

Here,  $\Delta\beta$  is the linear phase mismatch parameter whereas  $\beta_{p1}$  and  $\beta_{p2}$  are the propagation constants for the pumps at frequencies  $\omega_{p1}$  and  $\omega_{p2}$ , respectively.  $\beta_s$  and  $\beta_i$  are the propagation constants of the input signal and the generated idler at frequencies  $\omega_s$  and  $\omega_i$ , respectively.

## 4.2 Polarization-dependent FOPAs

The simplest form of a FOPA is the polarization-dependent configuration which requires that the orientation of the state-of-polarization of the incoming signal

is not random at the input of the FOPA. However, for practical applications, polarization-independent operation is required. Both categories can either be a single-pump FOPA or a dual-pump FOPA.

### 4.2.1 Single-pump polarization-dependent FOPA

A single-pump polarization-dependent FOPA requires only one pump and signal(s) at the input of the HNLF. In order to achieve efficient FWM, the polarizations of both the signal (signals in case of WDM) and the pump must be co-polarized at the input of the HNLF. Figure 4.1 shows a schematic representation of a single-pump polarization-dependent FOPA.

Considering the interaction of three co-polarized monochromatic waves (in one polarization direction) with frequencies  $\omega_p, \omega_s, \omega_i$  and propagation constants  $\beta_p, \beta_s, \beta_i$  for the pump, signal, and idler, respectively. The total electric field,  $E$ , propagating along the HNLF (neglecting the fiber loss) is given by [59, p. 369], [1]:

$$\begin{aligned}
 E = F(x, y) \frac{1}{2} [ & A_p(z, t) \cdot \exp(j[\beta_p z - \omega_p t]) \\
 & + A_s(z, t) \cdot \exp(j[\beta_s z - \omega_s t]) \\
 & + A_i(z, t) \cdot \exp(j[\beta_i z - \omega_i t]) + c.c ]
 \end{aligned} \tag{4.3}$$

Where  $F(x, y)$  is the transverse modal field profile.  $A_p(z, t)$ ,  $A_s(z, t)$ , and  $A_i(z, t)$  are the complex field amplitudes of the pump, signal, and idler, respectively. It is worth noting that the frequencies of all the waves are assumed to be similar such that the nonlinear coefficient are equal for the waves. The notation *c.c* means complex conjugate. The propagation of the individual waves in the HNLF is

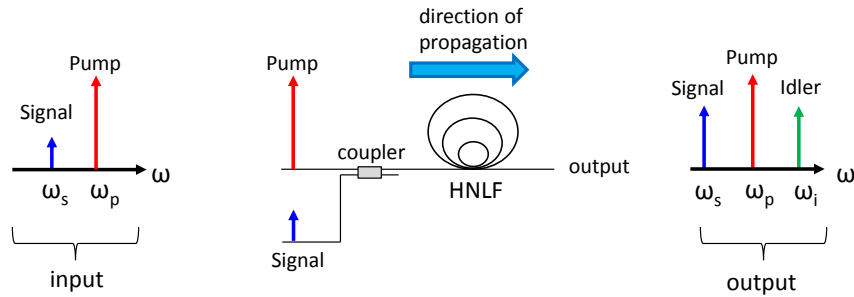


**Figure 4.1:** Single-pump polarization-dependent FOPA showing the generated idler and signal amplification at the output of the HNLF.

described by [59, p. 371], [1]:

$$\frac{dA_p}{dz} = j\gamma \left( |A_p|^2 + 2(|A_s|^2 + |A_i|^2) \right) A_p + 2j\gamma A_s A_i A_p^* \cdot \exp(j\Delta\beta z) \quad (4.4)$$

$$\frac{dA_s}{dz} = j\gamma \left( |A_s|^2 + 2(|A_i|^2 + |A_p|^2) \right) A_s + j\gamma A_i^* A_p^2 \cdot \exp(-j\Delta\beta z) \quad (4.5)$$

$$\frac{dA_i}{dz} = \underbrace{j\gamma \left( |A_i|^2 + 2(|A_s|^2 + |A_p|^2) \right) A_i}_{\text{SPM and XPM}} + \underbrace{j\gamma A_s^* A_p^2 \cdot \exp(-j\Delta\beta z)}_{\text{FWM}} \quad (4.6)$$

In equations (4.4), (4.5), and (4.6), SPM and XPM phase shifts form the first two terms on the right hand side of equations (4.4), (4.5), and (4.6). The last term on the right hand side of the equations corresponds to FWM among the interacting waves in the HNLF. Assuming an undepleted-pump condition and re-writing (4.4), (4.5), and (4.6) in terms of powers and phases of the waves where  $P_{p,s,i}(z) = |A_{p,s,i}(z)|^2$ , we have [104]:

$$\frac{dP_p}{dz} = -4\gamma \sqrt{(P_p^2 P_s P_i)} \cdot \sin\theta \quad (4.7)$$

$$\frac{dP_s}{dz} = 2\gamma \sqrt{(P_p^2 P_s P_i)} \cdot \sin\theta \quad (4.8)$$

$$\frac{dP_i}{dz} = 2\gamma \sqrt{(P_p^2 P_s P_i)} \cdot \sin\theta \quad (4.9)$$

Here,  $\theta$  is relative phase difference between the interacting waves in the HNLF and its rate of change over the fiber length is given by [105]:

$$\frac{d\theta}{dz} = \Delta\beta + \gamma(2P_p - P_s - P_i) + \gamma \left[ \sqrt{(P_p^2 P_s / P_i)} + \sqrt{(P_p^2 P_i / P_s)} - 4\sqrt{(P_s P_i)} \right] \cos\theta \quad (4.10)$$

In a typical phase-insensitive FOPA (i.e., when only signal and pump are present at the input of the HNLF) in an unsaturated condition,  $\theta$  is shown to develop from the initial value of  $\pi/2$ , thus power can flow from the pump to the signal and idler as can be seen from equations (4.7)-(4.9) [105]. Note that the FOPA discussion in the entire thesis is phase-insensitive unless otherwise stated. As the light propagates along the fiber, exchange of power occurs among the interacting waves and so long as  $\theta \approx \pi/2$ , the pump will feed power to the signal and idler so long as the total phase mismatch parameter is zero. Therefore the third

term in (4.10) can be neglected and the relative phase difference and the total phase mismatch parameter can be re-written as:

$$\frac{d\theta}{dz} \approx \Delta\beta + \gamma(2P_p - P_s - P_i) \approx \Delta\beta + 2\gamma P_p = \kappa \quad (4.11)$$

Where  $\kappa$  is the total phase mismatch parameter per unit length of the FWM among the interacting waves in the HNLF and it consists of a linear phase term,  $\Delta\beta = \beta(\omega_s) + \beta(\omega_i) - 2\beta(\omega_p)$ , and a nonlinear phase term,  $2\gamma P_p$ . In an unsaturated pump condition, where  $P_p \gg P_s$ , the  $P_s$  and  $P_i$  terms on the right hand side of equation (4.11) can be neglected. Thus the second approximation in equation (4.11) is valid. One can expand  $\beta(\omega)$  using Taylor's series around the zero-dispersion frequency,  $\omega_{zd}$ , and  $\Delta\beta$  can be written as [47, p. 112]:

$$\Delta\beta = \beta_3 \cdot (\omega_p - \omega_{zd})(\omega_s - \omega_p)^2 + \beta_4 \cdot \frac{(\omega_s - \omega_p)^2}{12} \left[ (\omega_s - \omega_p)^2 + 6(\omega_p - \omega_{zd})^2 \right] \quad (4.12)$$

The unsaturated gain of the signal,  $G_s$ , is defined as the ratio of the output signal power,  $P_s(L)$ , to the input signal power,  $P_s(0)$ , of a HNLF of length,  $L$ , and it is given by [47, p. 49] [1]:

$$G_s = \frac{P_s(L)}{P_s(0)} = 1 + \left[ \frac{\gamma P_p}{g} \cdot \sinh(gL) \right]^2 \quad (4.13)$$

Where  $g$  is the parametric gain coefficient which is defined as [47, p. 48]:

$$g^2 = [(\gamma P_p)^2 - (\kappa/2)^2] \quad (4.14)$$

It is clear from equations (4.13) and (4.14) that for a maximum signal gain,  $\kappa$  must be zero so that  $g^2$  is maximum. Therefore, equation (4.11) indicates that it is essential for the linear phase mismatch ( $\Delta\beta$ ) to be negative in order to compensate for the nonlinear phase mismatch ( $2\gamma P_p$ ) in order to obtain a maximum parametric gain. The parametric gain occurs when  $-4\gamma P \leq \Delta\beta \leq 0$ . To realize a negative  $\Delta\beta$ , according equation (4.12), the pump frequency ( $\omega_p$ ) must be placed slightly at a lower frequency relative to the zero-dispersion frequency ( $\omega_{zd}$ ) of the HNLF (i.e.,  $\omega_{zd} > \omega_p$ ). The unsaturated conversion efficiency of the idler,  $G_i$ , is also defined as the ratio of the output idler power with pump on to the input signal power and it given by [47, p. 48] [1]:

$$G_i = G_s - 1 \quad (4.15)$$

Thus at higher parametric gain levels (where  $G_s \gg 1$ ), the idler conversion efficiency and the signal gain will be almost equal. Figure 4.2 shows the calculated parametric gain, based on equation (4.13), of a single-pump FOPA using

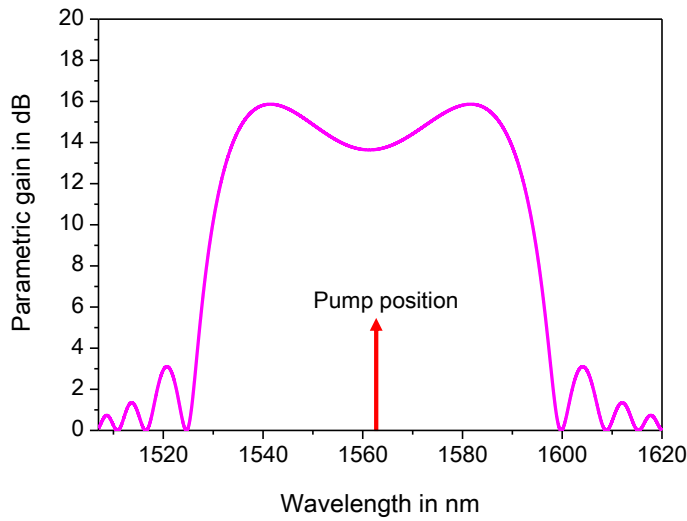


**Figure 4.2:** Simulated single-pump polarization-dependent FOPA gain-spectrum.

the following parameters: HNLF has length = 300 m,  $\gamma = 11$  /( $\text{W}\cdot\text{km}$ ), dispersion slope,  $S = 0.02$  ps/( $\text{nm}^2\cdot\text{km}$ ), zero-dispersion wavelength (ZDW) ( $\lambda_{zd}$ ) = 1560.9 nm,  $\beta_4 = 2.5 \times 10^{-4}$  ps<sup>4</sup>/km. The used pump power and wavelength are  $P_p = 31.5$  dBm and  $\lambda_p = 1561.3$  nm, respectively. The single-pump FOPA gain profile, as shown in Figure 4.2, has a dip. Thus, its implementation for WDM applications is undesirable especially for high gain amplification, since channels will not experience the same gain. The dip in the gain profile can be interpreted from Equation (4.12), for signal frequencies close to the pump frequency (i.e.,  $\omega_s \approx \omega_p$ ),  $\Delta\beta \approx 0$ . Therefore, the total phase mismatch parameter becomes positive (i.e.,  $\kappa > 0$  from Equation (4.11)). This indicates that the phase-matching condition is not fulfilled thereby reducing the FWM efficiency resulting in a dip of the gain profile around the center frequency. Specifically, the parametric gain becomes a quadratic dependence (i.e.,  $G_s \approx (\gamma PL)^2$ ) instead of exponential dependence (i.e.,  $G_s \approx \exp(\gamma PL)$ ) when the total phase mismatch parameter ( $\kappa$ ) is zero [1].

#### 4.2.2 Dual-pump polarization-dependent FOPA

The dual-pump FOPA is a suitable FOPA configuration for WDM applications since it is capable of producing a nearly flat gain profile. In this configuration, two pumps at frequencies  $\omega_{p1}$  and  $\omega_{p2}$  are used instead of only one pump. The pumps are placed symmetrically around the zero-dispersion frequency,  $\omega_{zd}$ , and are combined together with the weak signal. All three waves are aligned in polar-

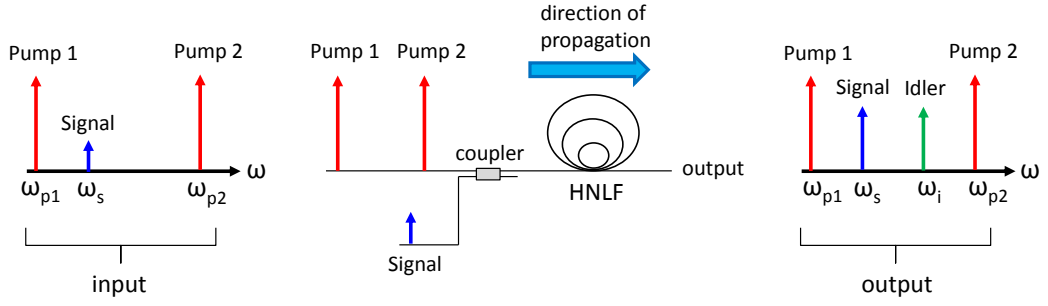


**Figure 4.3:** Dual-pump polarization-dependent FOPA showing the generated idler and signal amplification at the output of the HNLF.

ization before launching them into the HNLF [106] as shown in Figure 4.3. The phase mismatch parameter,  $\kappa$ , is given by:

$$\kappa = \Delta\beta + \gamma(P_1 + P_2) \quad (4.16)$$

Where  $P_1$  and  $P_2$  are the pump powers. The linear phase mismatch parameter ( $\Delta\beta$ ) is given by:

$$\Delta\beta = \beta(\omega_s) + \beta(\omega_i) - \beta(\omega_{p1}) - \beta(\omega_{p2}) \quad (4.17)$$

The Taylor series expansion can be again used to expand  $\beta(\omega)$  around the zero-dispersion frequency,  $\omega_{zd}$ , and  $\Delta\beta$  is given by [47, p. 117]:

$$\begin{aligned} \Delta\beta = & \beta_3 \cdot (\omega_{avg} - \omega_{zd}) [(\omega_s - \omega_{avg})^2 - (\Delta\omega_p)^2] \\ & + \frac{\beta_4}{12} \cdot [(\omega_s - \omega_{avg})^4 - (\Delta\omega_p)^4] \end{aligned} \quad (4.18)$$

Where the average pump frequency,  $\omega_{avg}$ , is given by:

$$\omega_{avg} = (\omega_{p1} + \omega_{p2})/2 \quad (4.19)$$

The pump separation,  $\Delta\omega_p$ , relative to the average pump frequency is also given by:

$$\Delta\omega_p = \omega_{p1} - \omega_{avg} = \omega_{avg} - \omega_{p2} \quad (4.20)$$

For a perfect phase-matching ( $\kappa = 0$ ), the average frequency ( $\omega_{avg}$ ) has to be placed slightly at a lower frequency (in the order of few nanometers) relative to the zero-dispersion frequency ( $\omega_{zd}$ ). In addition, an appropriate pump separation has to be chosen so that  $\Delta\beta$  can compensate for the nonlinear phase term

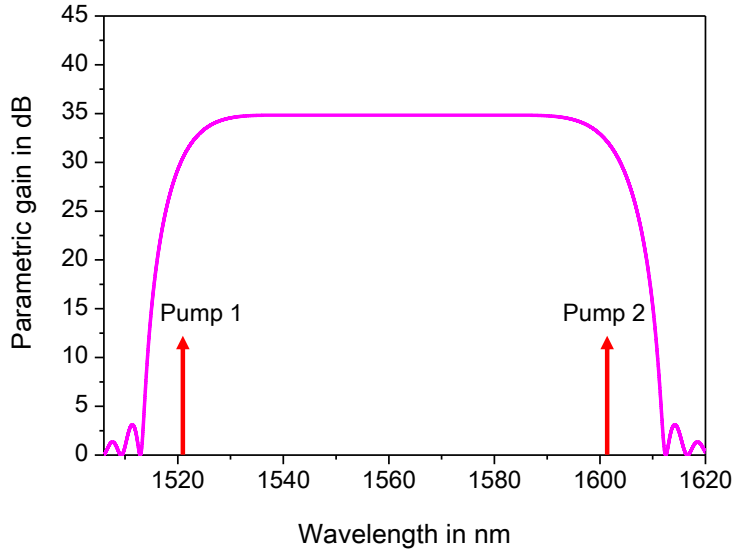


**Figure 4.4:** Simulated dual-pump polarization-dependent FOPA gain-spectrum.

in equation (4.16). The unsaturated parametric gain of the dual-pump FOPA is given by:

$$G_s = 1 + \left[ \frac{2\gamma\sqrt{P_1P_2}}{g} \cdot \sinh(gL) \right]^2 \quad (4.21)$$

Figure 4.4 shows a calculated parametric gain, based on equation (4.21), of a dual-pump FOPA using the following parameters: HNLF has length = 300 m,  $\gamma = 11$  /( $\text{W}\cdot\text{km}$ ), dispersion slope,  $S = 0.02$  ps/( $\text{nm}^2\cdot\text{km}$ ), ZDW ( $\lambda_{zd}$ ) = 1560.9 nm,  $\beta_4 = 2.5 \times 10^{-4}$  ps<sup>4</sup>/km. Pump power,  $P_1 = P_2 = 28.5$  dBm and pump wavelengths,  $\lambda_{p1} = 1521.1$  nm and  $\lambda_{p2} = 1601.1$  nm.

The broad bandwidth and flat gain profile of the dual-pump FOPA, as shown in Figure 4.4 makes it appealing for WDM applications. From Equation (4.18), it can be seen that for signal frequencies close to the average pump frequency ( $\omega_s \approx \omega_{avg}$ ), the linear phase mismatch becomes negative ( $\Delta\beta < 0$ ). Thus the total phase mismatch parameter,  $\kappa \approx 0$  from Equation (4.16). Therefore, the phase-matching condition is fulfilled over the frequency range around the center frequency. Adjusting the pump separation can either increase or decrease the gain-bandwidth. A 3-dB gain-bandwidth of over 100 nm using a FOPA based on the dual-pump configuration has been experimentally demonstrated [100]. However, in the event where the powers of the two pumps are not well optimized, a non-flat gain profile can be observed. This is due to the Raman effect which causes the pump at the shorter wavelength to feed energy to the pump at the longer wavelength. This effect occurs when the two pumps are within the Raman

gain bandwidth [47, p. 20].

### 4.3 Polarization-independent FOPA

To practically implement a FOPA in an optical transmission system, polarization-independent operation is necessary. This is due to the FOPA gain being a function of the state-of-polarization of the incoming signal. The presence of birefringence fluctuations in optical transmission links causes the state-of-polarization of the propagating signal to randomly vary along the link.

Polarization-independent operation is possible in FOPAs with any arbitrary state-of-polarization of the incoming signal as long as the FOPA is operated in a linear gain regime (i.e., small signal regime). Although polarization-independent operation in saturation has been shown in [107], practical implementation is often doubted since saturation operation of the FOPA severely degrades data signals [108, 109]. To achieve polarization-independent FOPA operation, two main architectures which are, orthogonally polarized pumps [61, 64, 106, 110] and polarization-diversity configurations [63, 111–113], are used.

#### 4.3.1 Orthogonally polarized pumps

Dual-pump FOPA with orthogonally polarized pumps is the simplest of all the polarization-independent FOPA schemes. It requires two pumps in its operation hence suitable for a dual-pump FOPA. The pumps must be orthogonal to each other [61, 64, 66]. They must have different frequencies (e.g.  $\omega_{p1}$  and  $\omega_{p2}$ ) and are placed symmetrically around the center frequency (close to the ZDW). The illustration in Figure 4.5 shows orthogonally polarized pumps (i.e.,  $x$ - and  $y$ -polarizations). The incoming polarization-scrambled signal couples its polarization to either of the orthogonally polarized pumps. Each polarization component of the signal experiences parametric gain due to the presence of the same polarization orientation of the pump in the HNLF. When both pumps have the same power, the polarization components of the signal experiences equal signal gain (same parametric gain spectra). Therefore the parametric amplification and generation of conjugated signal copies are independent of the input state-of-polarization of the incoming signal as shown in Figure 4.5. An obvious undesirable effect with this scheme is that, a perfect polarization orthogonality of the pumps must be maintained in the fiber at all times but that cannot be achieved with fibers with random birefringence fluctuation. The fiber birefrin-

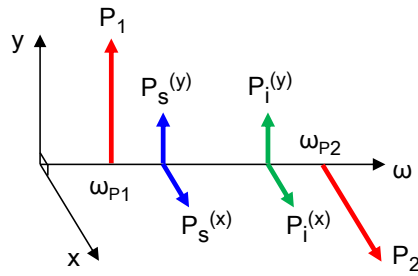


**Figure 4.5:** Schematic representation of orthogonally polarized pumps for polarization - independent FOPA operation.

gence causes different gain spectra for the two polarized pumps, and this effect becomes more pronounced in wideband parametric amplification (for large pump spacing), eventually leading to large PDGs [47, p. 252], [64].

### 4.3.2 Polarization-diversity configurations

Unlike the orthogonally polarized pumps technique which requires dual-pumps, the polarization-diversity technique can be implemented either with a single-pump or a dual-pump FOPA configuration [63, 111]. The polarization-diversity scheme requires a polarization beam splitter (PBS) which splits the arbitrary polarization of the incoming weak signal into its orthogonal (e.g.  $x$  and  $y$ ) polarization components which travel on different paths as shown in Figure 4.6. Each signal component experiences parametric amplification once both pump and signal propagates through a HNLF. Therefore the parametric gain becomes independent of the state-of-polarization of the incoming signal. Theoretically, same pump powers in both directions of the loop lead to the same gain spectrum (gain reciprocity) when the FOPA is operated in an unsaturated pump regime. In this configuration, the available pump power for amplification will be  $P_0/2$  (i.e., when the total pump power is  $P_0$ ) in each direction of the loop. Thus, the parametric gain for signals around the pump wavelength (i.e., where  $G_s \approx (\gamma PL)^2$ ) will be 6 dB smaller compared to the gain in a polarization-dependent configuration with the same total pump power. The gain in both configurations can be made equal by doubling, for instance, the fiber length of the FOPA employing the polarization-diversity scheme. The polarization-diversity technique has several configurations, as shown in Figure 4.6.

**Polarization-diversity: parallel scheme**

Two identical HNLFs (with same fiber specifications) are required in this configuration in order to obtain identical parametric gain at the output of the polarization beam combiner (PBC) as shown in Figure 4.6(i). In practice, it is difficult to produce identical HNLFs due to uncontrolled effects such as fiber core deformations which eventually lead to zero-dispersion wavelength fluctuation. In addition, the optical path lengths in the two directions must perfectly match in order to avoid interference at the output. The available total pump power is reduced

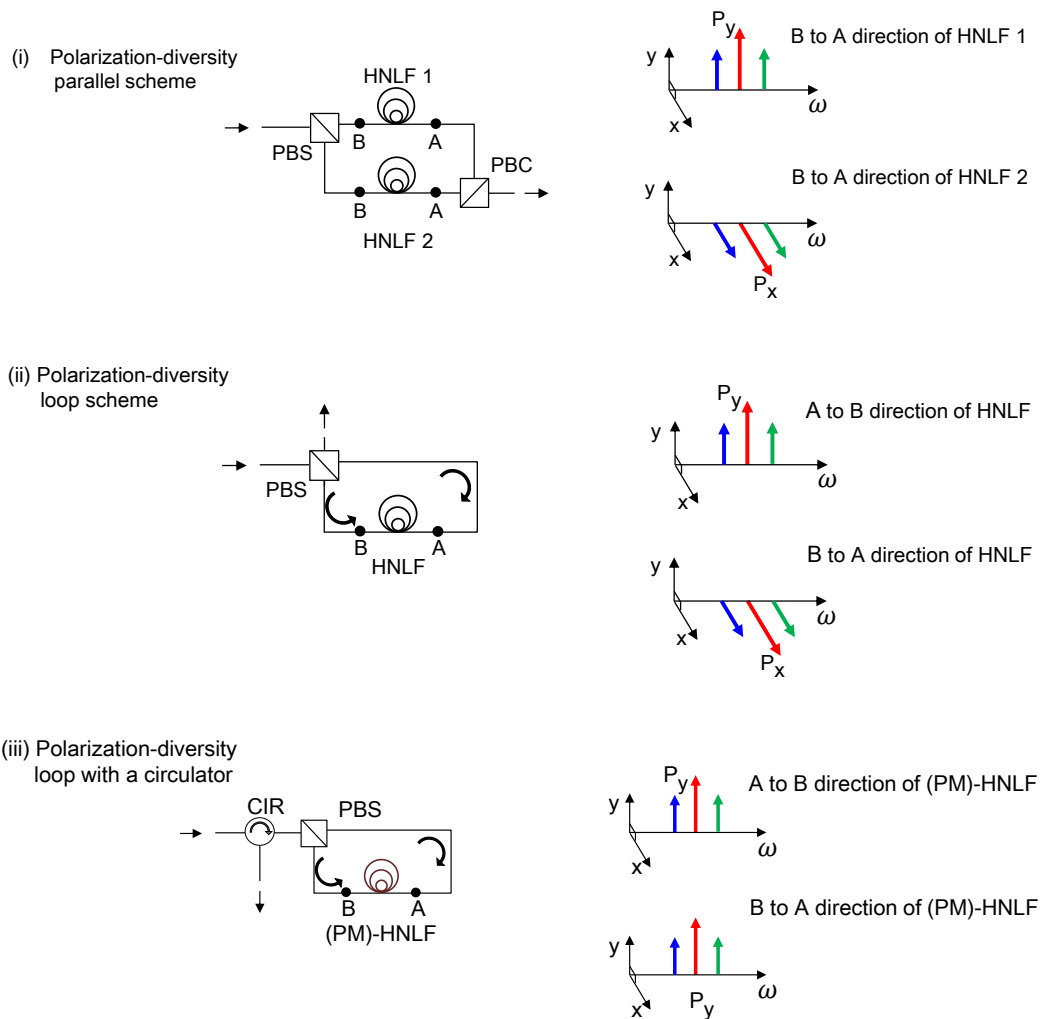


**Figure 4.6:** Polarization-independent technique based on: (i) polarization diversity scheme with parallel configuration, (ii) polarization-diversity loop scheme, and (iii) polarization-diversity loop scheme employing a circulator (CIR).

by half, due to the splitting, thus the maximum gain is reduced compared to the polarization-dependent counterpart configuration. Nevertheless, this scheme has less issues with reflections which is often the problem in diversity schemes with loop configurations.

### **Polarization-diversity: loop scheme**

This configuration avoids the optical path length matching issue in the parallel scheme. It also requires only one PBS and a HNLF as shown in Figure 4.6(ii). Here, after a parametric process in the HNLF, the bidirectional waves (A to B and B to A directions) are re-combined by the PBS and the waves exit the fourth port of the PBS. Similar to the parallel scheme, the maximum gain is reduced (due to the splitting) compared to the polarization-dependent counterpart configuration. In addition, since the propagating waves travel bidirectionally in the HNLF, the scheme has reflection-induced distortion problems [47, p. 251] [67].

### **Polarization-diversity loop with a circulator**

The output wave from the PBS in the diversity loop scheme can be made to exit the input port of the PBS. A circulator with a high isolation between the input/output ports is employed in order to obtain the output light after the loop as shown in Figure 4.6(iii). This configuration is usually used in the case where the HNLF is polarization-maintaining (it can also be used for conventional HNLFs). Note that one of the main challenges in realizing a FOPA with a conventional HNLF is the random nature of birefringence of the HNLF which eventually causes random rotation of the state-of-polarization of the propagating light waves in the fiber [47, 82]. Therefore one way to avoid such a detrimental effect is to employ a PM-HNLF since state-of-polarization preservation of the light waves along the fiber is ensured once they are linearly polarized along the axes of birefringence of the PM-HNLF [47].

In PM-HNLFs, the orthogonal principal states-of-polarizations are well defined therefore considering Figure 4.6(iii), the orthogonal components of the pump, after splitting, travel in the same polarization axis (one of the principal axes) of the PM-HNLF. Due to the high birefringence of PM-HNLFs, the unpredictable variations as a result of PMD in conventional HNLFs are eliminated. However, the scheme is more prone to reflections since all waves propagate on the same axis of polarization of the PM-HNLF [67].

## 4.4 Impact of pump-induced distortions

### 4.4.1 Pump RIN and pump OSNR

One fundamental requirement of FOPA is the quality of the used pump. The relative intensity noise (RIN) and the OSNR of the pump are the key requirements. The impact of pump RIN on 16-QAM data signals have experimentally been investigated and reported in [114]. The studies indicated that the pump amplitude fluctuation has a significant impact on the quality of the signal. This is due to the exponential parametric gain dependence on the pump power. Hence small fluctuations on the pump amplitude causes severe gain fluctuation on the signal and idler thereby degrading their quality. It was shown that pumps with lower RIN (e.g. below -155 dB/Hz) and high OSNR (e.g. above 56 dB) renders parametric amplification or conversion with good signal or idler quality [114, 115].

### 4.4.2 Effect of pump line-width broadening

As already discussed in Section 3.3.1, the presence of SBS in fibers limits the amount of optical power at the output of the fiber. This effect limits the achievable parametric gain in FOPAs since the gain depends on the pump power. A well-known technique for suppressing the SBS is broadening the line-width of the pump without affecting the amplitude. This is obtained by modulating (dithering) the pump phase [98]. The phase relation among the interacting waves in a dual-pump FOPA, as discussed in Section 4.1, is given by:

$$\varphi_i = \varphi_{p1} + \varphi_{p2} - \varphi_s \quad (4.22)$$

Where  $\varphi_i$ ,  $\varphi_{p1}$ ,  $\varphi_{p2}$ , and  $\varphi_s$  are the phases of the idler, pump one and two, and signal, respectively. Equation (4.22) shows that the phase of the idler contains the addition of the pump phases. Assuming  $\varphi_{p1} = \varphi_{p2}$ , then the idler phase is proportional to twice the pump phase. Pump phase-dithering with  $n$  number of RF tones indicates that the pump has a line-width which consists of  $3^n$  spectral components of the main-band (dominating spectral components) [98]. The spectrum of the converted wave (idler) becomes twice as broad as the pump spectrum ( $2 \times 3^n$ ) [116].

The use of idlers in FOPAs have many applications such as wavelength conversion, all-optical add-drop, and optical phase conjugation for nonlinearity compensation. The quality of the idler must be the same as the signal but this is

usually not the case in systems employing the pump phase-dithering for SBS threshold enhancement.

One well - known technique for reducing the idler spectrum broadening is counter-phasing dithering. The technique requires two pumps (at different wavelengths) and it is thus not applicable for single-pump FOPA [116–118]. The phases of the two pumps are dithered such that there is a  $\pi$ -phase shift between the phases of the pumps ( $\varphi_{p1} = -\varphi_{p2}$ ), therefore from equation (4.22),  $\varphi_i = -\varphi_s$ . Thus the idler pump phase-dithering induced broadening cancels out and the idler quality becomes the same as the signal.

## 4.5 Summary

In this chapter, the fundamental principles governing fiber-based optical parametric amplifiers (FOPAs) have been theoretically discussed. In order to implement FOPAs in practical optical networks, polarization-independent operation is a prerequisite since the simplest form of FOPA is polarization-dependent. FOPA-based schemes employing orthogonally polarized pumps and the polarization-diversity loop techniques for the realization of polarization-independent operation have been discussed. The impact of pump noise, such as high relative intensity noise (RIN), and low optical signal-to-noise ratio (OSNR) on the amplified signals and the wavelength converted signals have been reviewed. Counter - phasing dithering is an efficient technique for reducing idler pump phase-dithering induced broadening.

## Chapter 5

# Realization of a Fiber-based Optical Parametric Amplifier

Systematic characterization of a fiber-based optical parametric amplifier (FOPA) for any application in the optical communication system is paramount, since it gives a general information of the FOPA as a sub-system. In a transmission network, a good understanding based on systematic characterization is desirable and it helps in system analysis and performance evaluation.

This chapter explores the experimental implementation of a FOPA. The chapter begins with the discussion of the basic characterizations of a single-pump polarization-dependent FOPA. Furthermore, among the several polarization-independent configurations which were introduced in Chapter 4, the polarization-diversity loop with a circulator (see Figure 4.6(iii)) is implemented in order to realize a single-pump polarization-independent FOPA. The FOPA is characterized using both CW signals and a 28-GBd QPSK data signal. In order to achieve polarization stabilization in the FOPA, as described in Chapter 4, a PM-HNLF is used in realizing the FOPA.

## 5.1 Characterization of a polarization-dependent FOPA

### 5.1.1 Stimulated Brillouin scattering measurement of a PM-HNLF

As a result of SBS in fibers, as discussed in Chapter 3 Section 3.3.1, the applicable pump power in HNLFs is usually limited. Consequently, the achievable signal on-off gain of the FOPA is also limited once the pump power is above the Brillouin threshold of the fiber. In this thesis, the pump phase-dithering or pump phase-modulation technique [98], as discussed in Chapter 4, is implemented in order

to increase the SBS threshold. To measure the SBS characteristics of the PM-HNLF, the experimental setup shown in Figure 5.1 is used. It consists of an external cavity laser (ECL) at a wavelength of 1562.2 nm which serves as a CW source of the pump. This is phase-modulated using a phase-modulator (Phase Mod.) with a modulation index of 1.4 radians. The phase-modulator has been driven by three sinusoidal RF tones at the frequencies  $f_1$ ,  $f_2$ , and  $f_3$  with values 75 MHz, 275 MHz, and 875 MHz, respectively. Each of the RF tone has been modulated with a modulation index of 1.4 radians. The RF tones are electrically combined together using an electrical coupler and after amplifying the total RF power using an electrical amplifier (24-dB linear gain, 3-dB cut-off frequency of 1200 MHz), an electrical low-pass filter (LPF) enables the suppression of the high frequency components which arises as a result of harmonic generation by the electrical amplifier. The polarization controller (PC) after the pump laser is used to align the polarization of the pump wave into the axis of the phase modulator. Note that 10% of the (output port of the 10-dB coupler) pump power is used to combine with another CW light source, which serves as a local oscillator (LO), and both lights are detected by a photodiode (PD) for a heterodyne detection on an electrical spectrum analyzer (ESA). After amplification of the pump (the 90% output port of the 10-dB coupler) with a high power EDFA, the out-of-band amplified ASE noise is suppressed using an optical bandpass filter (OBPF) with a full-width at half maximum (FWHM) bandwidth of 0.8 nm. The ASE suppression in this particular experiment is not critical, thus the OBPF (with an insertion loss of 1.6 dB) can be removed to increase the pump power.

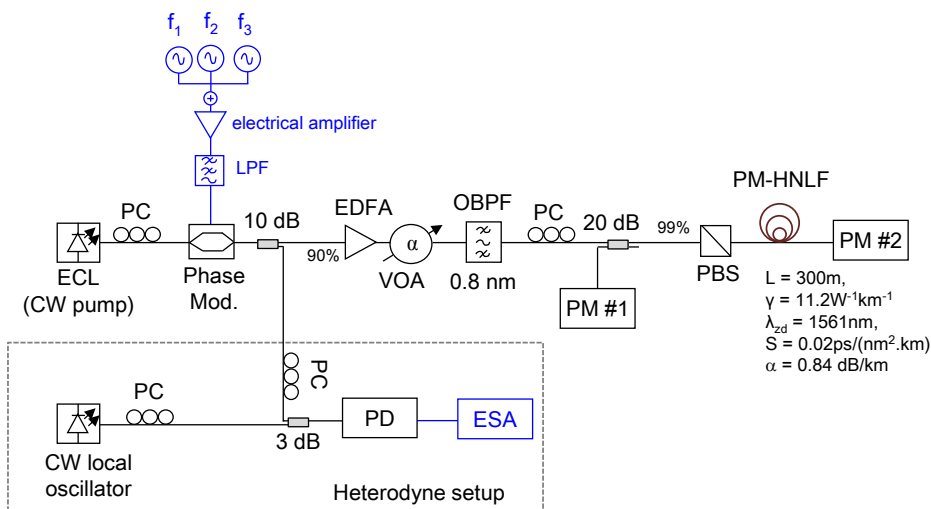


**Figure 5.1:** Experimental setup for the SBS measurement.

The use of the polarization controller in front of the polarization beam splitter (PBS) enables the polarization alignment of the pump wave into the fast-axis of the PM-HNLF. The output light of the fiber is detected using a power meter (PM #2). The 20-dB coupler in front of the PM-HNLF enables the measurement of the back-scattered light (Rayleigh and SBS) using a power meter (PM #1). The variable optical attenuator (VOA) has been used to adjust the pump power levels into the fiber. The PM-HNLF has length ( $L$ ), fast-axis zero-dispersion wavelength ( $\lambda_{zd}$ ), nonlinear coefficient ( $\gamma$ ), attenuation ( $\alpha$ ), and fast-axis slope ( $S$ ) of 300 m, 1561 nm, 11.2/(W·km), 0.84 dB/km, and 0.02 ps/(nm<sup>2</sup>·km), respectively. Particularly, the fast-axis of the PM-HNLF is used in the experiment since the slow-axis zero-dispersion wavelength is at 1514 nm which is not a typical telecommunication wavelength.

### **Experimental results**

In order to measure the SBS characteristics from the PM-HNLF, the pump power into the PM-HNLF has been initially varied from 6 dBm to 22 dBm and all the three RF tones are switched-off. Figure 5.2 shows the measured output power from the PM-HNLF and the back-scattered power as functions of the input pump power into the fiber. It can be seen from Figure 5.2 that without the application of pump phase-dithering (no RF tone), as the input power is gradually increased, the output power from the fiber increases and the back-scattered power grow as well. The measured SBS threshold for this case (no pump phase-modulation tone) is found to be 16.5 dBm (1%-threshold). After the 16.5 dBm input power, the output power begin to saturate whereas the back-scattered power continues to increase.

Therefore the 1%-SBS threshold gives the input power for which the output pump power starts to saturate. Furthermore, after turning-on the 75 MHz RF tone, the RF power of the sinusoidal tone is adjusted so as to obtain equal amplitude of the major spectral lines (dominating spectral components) on the electrical spectrum analyzer (ESA). Application of only one RF tone for the pump phase-modulation therefore increases the SBS threshold to 21 dBm (indicating 4.5-dB increase in the SBS threshold). This value is expected since, ideally, the SBS threshold improvement scales with  $10 \cdot \log_{10} 3^n$ , where  $n$  is the number of RF tones. After application of all three RF tones, the SBS threshold power increased to 30.7 dBm (indicating 14 dB more pump power compared to the case without any pump phase-dithering).

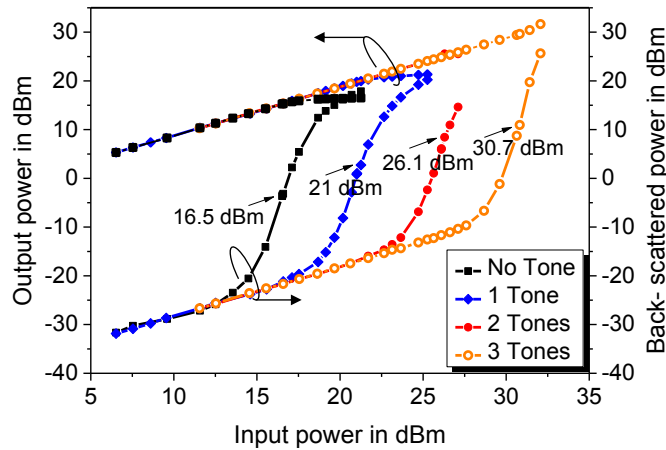


**Figure 5.2:** SBS measurements for up to 3-RF pump phase-dithering tones of frequencies: 75 MHz, 275 MHz, and 875 MHz.

### 5.1.2 Impact of pump wavelength detuning and pump power variation on the signal gain-bandwidth

One of the appealing features of a FOPA is the degree-of-freedom to vary the gain-bandwidth profile for a desired application. This unique feature is realized by either a suitable allocation of the pump wavelength with respect to the zero-dispersion wavelength of the implemented HNLF or a specific pump power of the FOPA [1, 47, 82]. Therefore the investigation of the pump wavelength and the pump power characteristics in designing a FOPA cannot be disregarded. Figure 5.3 is a representation of the experimental setup that has been implemented for the investigation. A single-pump polarization-dependent FOPA is employed for the investigation of the signal gain-bandwidth profile dependence on the pump wavelength detuning.

An external cavity laser (ECL) with a line - width of 100 kHz and a RIN of -145 dB/Hz is used as a CW pump source for the FOPA. The phase of the pump is dithered by a phase modulator (Phase Mod.) which is driven by three sinusoidal RF tones as discussed in Section 5.1. The pump phase-dithering has been implemented so as to increase the overall SBS threshold of the used fiber. For simplicity, the electrical amplifier and filter as well as the heterodyne setup for monitoring the adjusted phase-modulation on the electrical spectrum analyzer are not shown in Figure 5.3. After amplification of the phase-modulated pump using an EDFA, the out-of-band ASE noise is suppressed using an optical band-pass filter with a bandwidth of 0.8 nm. A second external cavity laser serves as

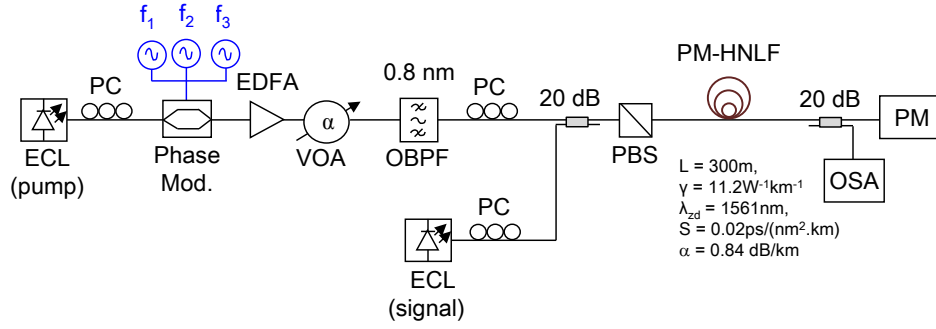


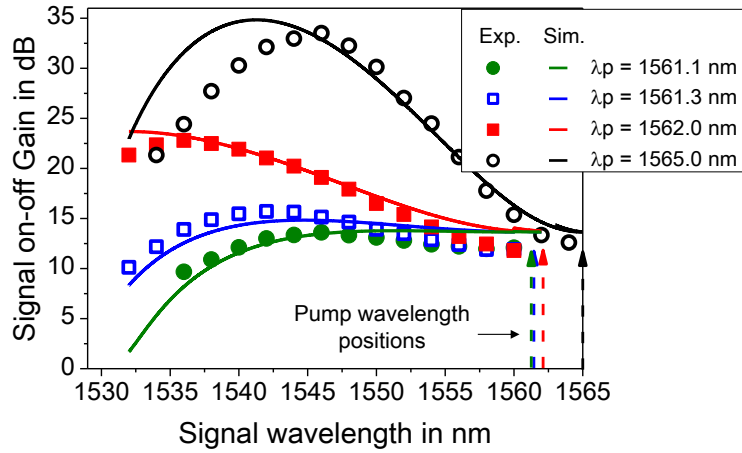
**Figure 5.3:** Schematic representation of the experimental setup of a single-pump polarization-dependent FOPA.

a CW signal source. The signal and the pump are combined and after aligning the polarization of both waves, they are sent to the fast-axis of the PM-HNLF via the polarization beam splitter (PBS). The PM-HNLF that has been used in this experiment is the same as the one used in Section 5.1.1. In order to operate the FOPA in the linear regime, the pump power ( $P_p$ ) and the signal power ( $P_s$ ) that have been sent to the PM-HNLF are kept fixed at 31.5 dBm and -14.5 dBm respectively [47, 108, 119].

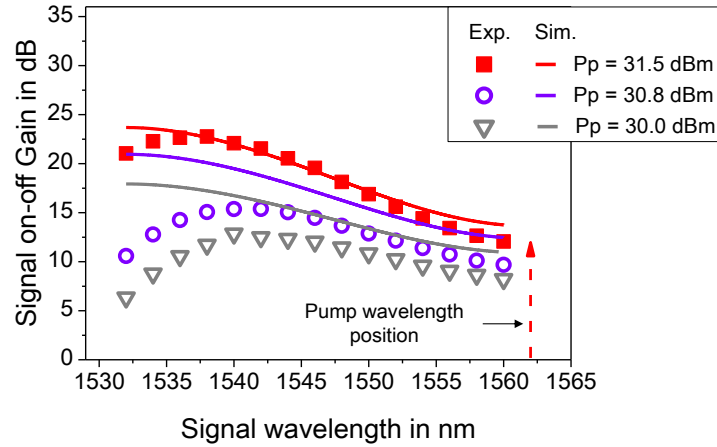
### Experimental results

To measure the dependence of signal gain-bandwidth profile on the pump wavelength ( $\lambda_p$ ) variation, the pump wavelength has been set to 1561.1 nm, 1561.3 nm, 1562 nm, and 1565 nm. It should be noted that the parametric on-off signal gain is defined as the ratio of the signal power at the output of the PM-HNLF with the pump-on to the signal power at the output of the PM-HNLF with the pump-off [54]. The on-off gain spectrum of the signal at a specific pump wavelength is measured on the optical spectrum analyzer (OSA) by adjusting the signal wavelength ( $\lambda_s$ ) from 1532 nm to 1564 nm. The experimental measurements are compared with theoretical (analytical) simulation (i.e., from equation (4.13)) in Section 4.2.1. The analytical simulation and the experimental results are, respectively, shown as solid lines and symbols in Figure 5.4. The used parameters for the PM-HNLF in the simulation are: length ( $L$ ) = 300 m, fast-axis zero-dispersion wavelength ( $\lambda_{zd}$ ) = 1561 nm, nonlinear coefficient ( $\gamma$ ) = 11.2/(W·km), attenuation ( $\alpha$ ) = 0.84 dB/km, and fast-axis slope ( $S$ ) = 0.02 ps/(nm<sup>2</sup>·km). The parameters are the same as those used in the experiments. A typical value of the fourth-order dispersion,  $\beta_4$ , of  $2.7 \times 10^{-55}$  s<sup>4</sup>/m has been chosen in the theoretical

simulation [59, p. 397].



(a)



(b)

**Figure 5.4:** Evaluation of a single-pump polarization-dependent FOPA on the: (a) Impact of pump wavelength detuning on the signal gain - bandwidth profile at a fixed pump power of 31.5 dBm. (b) impact of pump power variation on the signal gain-bandwidth profile at a fixed pump wavelength of 1562 nm. Solid lines-theoretical simulation (Sim.) using equation (4.13), symbols-experimental (Exp.) results. Remark that  $\lambda_{zd} = 1561.0$  nm.

Figure 5.4(a) shows the measured signal spectrum for each set pump wavelength. It is clear that the peak signal gain decreases with decreasing the pump wavelength detuning with respect to the zero-dispersion wavelength. In addition, the peak signal gains are measured at different signal wavelengths. However, the signal amplification bandwidth decreases with increasing the pump

wavelength detuning. For instance, the measured 3-dB bandwidth (excluding the idler) are 6 nm, 7 nm, and 8.8 nm for pump wavelength of 1565 nm, 1561.3 nm, and 1561.1 nm respectively. The pump wavelength is not set to a wavelength less than the zero-dispersion wavelength. This is because a pump wavelength less than the zero-dispersion wavelength will result in a poor phase-matching condition as discussed in Chapter 4. The different signal gain profiles in Figure 5.4(a) are due to different phase-matching conditions (as a result of the pump wavelength detuning). In practice, the zero-dispersion wavelength is not constant but it fluctuates. Even small changes in the zero-dispersion wavelength (less than 0.1 nm) can produce large changes in the gain spectrum [59, p. 398]. Therefore one of the reasons for the discrepancy between the experiment and the theory is due to the zero-dispersion wavelength fluctuation which is not included in the simulation. It is worth noting that the impact of zero-dispersion wavelength fluctuation on the gain profile will be discussed later in this Chapter. In addition, the impact of the fiber loss has been neglected in the simulation. Nevertheless, a strong sensitivity of the pump wavelength on the gain profile is visible in both the theory and the experimental results.

The influence of pump power variation on the signal gain-bandwidth is also investigated. Here, the pump wavelength is kept fixed at 1562 nm and the pump powers into the PM-HNLF are adjusted to 30 dBm, 30.8 dBm, and 31.5 dBm. Note that in each measurement, the signal power is still kept constant at -14.5 dBm as in the previous experiment. Similar to Figure 5.4(a), the theoretical simulation has been compared with the experimental results. It can clearly be seen from Figure 5.4(b) that the peak signal gain increases with increasing the pump power (more visible in the experimental results) which also shapes the curvature of the signal gain spectra. The discrepancies in both the theory and experiments is also due to the zero-dispersion wavelength fluctuation and the fiber loss which has been neglected in the theory.

### 5.1.3 Saturation measurement

The saturation characteristic is an essential parameter of any optical amplifier. Therefore, for the purpose of system evaluation, the saturation characteristics of the investigated single-pump polarization-dependent FOPA are studied.

The experimental setup in Figure 5.5 is employed for the saturation measurement. Specifically, the pump power has been kept constant at 31.5 dBm for all

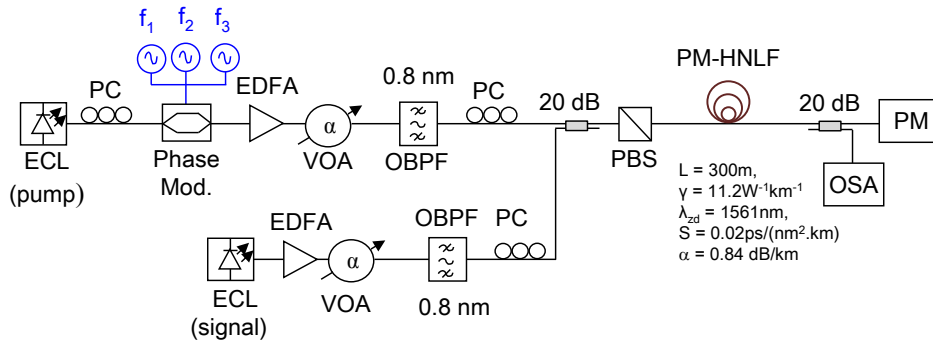


**Figure 5.5:** Experimental setup for saturation measurement of a single-pump polarization-dependent FOPA.

the measurements and for a particular set pump wavelength, the signal power into the PM-HNLF is varied from -30 dBm to +10 dBm using the variable optical attenuator in the signal path. The measurement was carried out for pump wavelengths ( $\lambda_p$ ) of 1561.1, 1561.3 nm, 1562 nm, and 1565 nm. The used setup is similar to the one in Figure 5.3 except the EDFA and the OBPF in the signal path. In addition, the measurements are performed for signal wavelengths at the peak on-off gain for the different spectra in Figure 5.4. The summary of the saturation performance of the FOPA is shown in Figure 5.6.

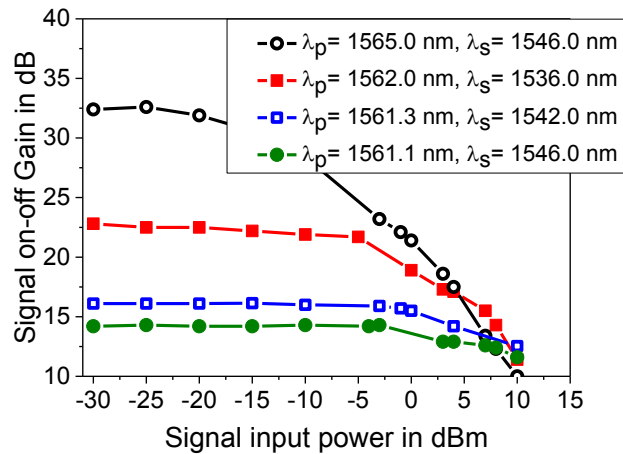


**Figure 5.6:** Saturation characteristics of a single-pump polarization-dependent FOPA operating at a pump power of 31.5 dBm.

Therefore higher signal input powers are required for pump depletion at lower on-off gain whereas lower input powers are already sufficient for pump depletion

at higher gain. It is evident from Figure 5.6 that as a result of higher signal amplitudes due to the higher signal gain in the case of the 1565-nm pump wavelength, the pump is quickly depleted thereby reaching saturation much faster than at the lower signal gains. Nevertheless at low on-off gain, the FOPA also saturates as a result of higher signal input power which consequently depletes the pump.

## **5.2 Characterization of a polarization - independent FOPA**

In practical optical communication systems, the random variation of the propagating signal's state-of-polarization requires polarization-independent devices in the transmission network. Here, the polarization-diversity loop technique has been adapted to a PM-HNLF for the application of a single-pump polarization-independent FOPA. Specifically, the polarization-diversity loop with a circulator (Figure 4.6(iii)) in Section 4.3 has been used.

### **5.2.1 Impact of back-reflections in a polarization-diversity loop**

One of the main differences between a FOPA with straight configuration (i.e., polarization-dependent) and a FOPA based on a polarization-diversity loop scheme is the presence of back reflections in the latter. These reflections (e.g. Rayleigh scattering and SBS) can introduce distortions to the propagating light waves in the loop. Therefore systematic investigations are necessary to verify the impact of reflection-induced distortions in a FOPA based on the polarization-diversity loop scheme especially at high gain conditions.

#### **Experimental setup**

Figure 5.7(a), setup I, is a representation of the experimental setup of a single-pump polarization-independent FOPA based on the polarization-diversity loop scheme. The PM-HNLF used in the setup is the same as the one which has been used in the previous experiments. The setup consists of an external cavity laser with a line-width of 100 kHz and a relative intensity noise (RIN) of -145 dB/Hz.

The laser is used as a CW pump source at a wavelength of 1562.2 nm. After phase-dithering of the pump with three or four sinusoidal RF tones (depending on the type of investigation) of frequencies 75 MHz, 275 MHz, 875 MHz, and

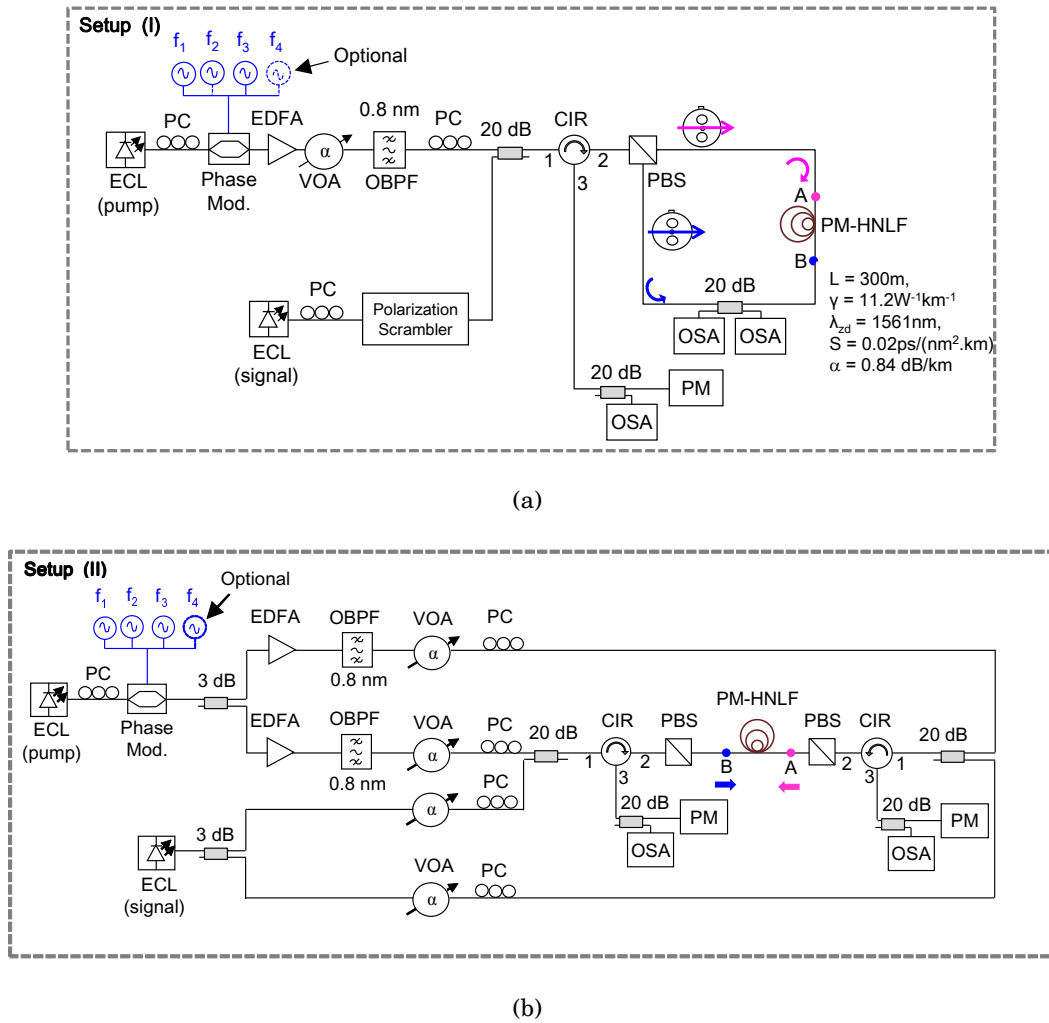


**Figure 5.7:** Experimental setups: (a) Single-pump polarization-independent FOPA based on the polarization-diversity loop scheme. (b) Modified setup of a single-pump polarization-independent FOPA based on the polarization-diversity loop so as to control the clockwise (A to B) and counter-clockwise (B to A) propagating pump waves in the diversity loop.

2710 MHz representing  $f_1$ ,  $f_2$ ,  $f_3$ , and  $f_4$  in the setup, the phase-modulated pump is amplified using an EDFA. Note that the fourth RF tone will be used when higher SBS threshold or pump power (parametric gain) is required.

The variable optical attenuator (VOA) in the pump path serves as a control for the pump power into the PM-HNLF. The out-of-band ASE noise is suppressed with an optical bandpass filter with a bandwidth of 0.8 nm. A tunable external cavity laser is also used as a CW signal source. The total signal power in

the diversity loop (i.e., both directions of the PM-HNLF) is set to -14.5 dBm and the polarization scrambler enables the measurement of the effectiveness of the polarization-independence of the FOPA. After combining the pump and the signal with a 20-dB coupler, both waves are sent to the polarization beam splitter (PBS) via port 2 of the circulator (CIR). It should be noted that the fiber outputs of the polarization beam splitter and the PM-HNLF are connected such that the orthogonal polarization components (vertical and horizontal polarization) of the incoming light travel on the fast axis of the PM-HNLF both in the A to B (clockwise) and B to A (counter-clockwise) directions of the diversity loop. The A to B and B to A pump powers in the loop are monitored with an optical spectrum analyzer via the 20-dB coupler in the loop. After launching the pump to the polarization beam splitter, a manual adjustment of the polarization controller before the polarization beam splitter enables the setting of equal pump powers in the A to B and B to A directions of the diversity loop. The technique for dividing the pump power into the directions of the diversity loop is known as *pump splitting*. Furthermore, the polarization beam splitter also splits the polarization scrambled signal's polarization into its orthogonal components which also travel in the fast axis of the PM-HNLF in both the A to B and B to A directions of the loop. The polarization-aligned signals with the pump components traveling in both directions of the nonlinear medium experiences the same parametric gain in each direction of the PM-HNLF (i.e., when the FOPA is operated in the linear regime) irrespective of the input state-of-polarization of the signal. After recombining the amplified signals by the polarization beam splitter, the total signal is routed to the optical spectrum analyzer (via the output port 3 of the circulator and the 20-dB coupler at the output of the FOPA) for evaluation.

To investigate the impact of the reflections in the diversity loop, the modified setup shown in Figure 5.7(b), setup II, is implemented. This allows an independent control of the A to B and the B to A propagating pump waves in the diversity loop. The variable optical attenuators (VOAs) are used to independently control the propagating light waves whereas manipulating the polarization controllers enables polarization alignment of the light waves to the fast axis of the PM-HNLF.

### **Discussion of results**

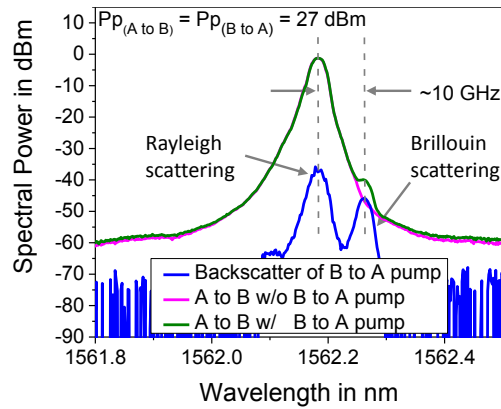
Initially, 3-RF tones (75 MHz, 275 MHz, and 875 MHz) are used and the pump powers in each direction of the PM-HNLF in the setup II (Figure 5.7(b)) are each set to 27 dBm. Note that the total pump power will correspond to a signal on-off

gain of 5 dB if a signal is present. The B to A pump is turned-on and its back-scattered light is measured with an optical spectrum analyzer. In order to verify the impact of the back-scattered light, the A to B pump is also turned-on and its spectrum has been measured while the B to A pump is turned-on and off.

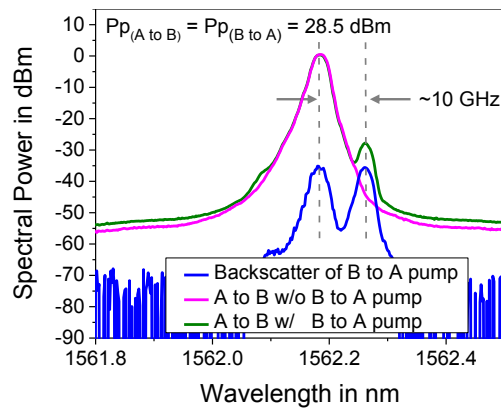
The measured optical spectra of the various cases are shown in Figure 5.8. It can be seen from Figure 5.8(a) that without the B to A counter propagating pump, the A to B pump spectrum is undistorted (depicting pump spectrum in a polarization-dependent FOPA). Although the SBS from the back-scattered light of the B to A pump is smaller than the Rayleigh scattered light, it is clear from the measured spectra that when both pumps from each direction (A to B and B to A pumps) of the PM-HNLF are turned-on, the A to B pump then becomes slightly distorted by the SBS of the counter propagating pump which amplifies a 10-GHz frequency component of the A to B pump. It is worth mentioning that due to the small signal gain, the presence of signal in the HNLF does not have any influence on the pump spectra shape.

The pump powers in each direction of the fiber is further increased to 28.5 dBm and later to 31.5 dBm. The total pump powers will, respectively, correspond to a signal on-off gain of 10 dB and 19.3 dB if a signal is present. Figure 5.8(b) shows that increasing the pump power resulted in an increase of the SBS of the counter propagating pump. Consequently the generated side-band on the A to B pump is higher than that in the case of lower pump powers. The Rayleigh back-scattered light now has a similar amplitude as the SBS. In other words the A to B pump is more distorted than the case when the pump powers are low. Figure 5.8(c) shows the pump spectra when the pump powers are increased to 31.5 dBm at each side of the fiber, and it can be seen that the growth of the generated SBS (of the B to A pump) is found to be 37 dB more than that in the case when the pump powers are each 27 dBm as shown in Figure 5.8(a). This high increase in the side-band power is due to the amplification of the high SBS power of the counter propagating pump. Moreover, it is evident that the A to B pump shape is more distorted (when both pumps at each side of the fiber are turned-on) than the previous two scenarios when the pump power per direction have been 27 dBm and 28.5 dBm.

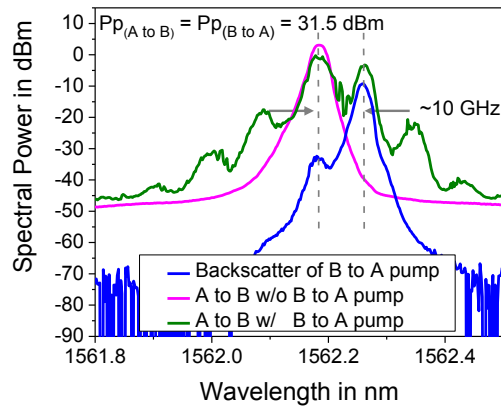
To investigate the severity of the SBS of the propagating pumps, using the setup in Figure 5.7(b), only the A to B pump has been allowed to propagate in the HNLF. The corresponding SBS is measured as the input power is adjusted from 27 dBm to 31.5 dBm. This scenario is analogous to the SBS measurement



(a)



(b)



(c)

**Figure 5.8:** Optical pump spectrum (after 20-dB coupler) with phase-dithering of 3-RF tones (OSA resolution of 0.01 nm) showing SBS-induced distortion at (a)  $P_p = 27 \text{ dBm}$  at each direction of the fiber. (b)  $P_p = 28.5 \text{ dBm}$  at each direction of the fiber. (c)  $P_p = 31.5 \text{ dBm}$  at each direction of the fiber.

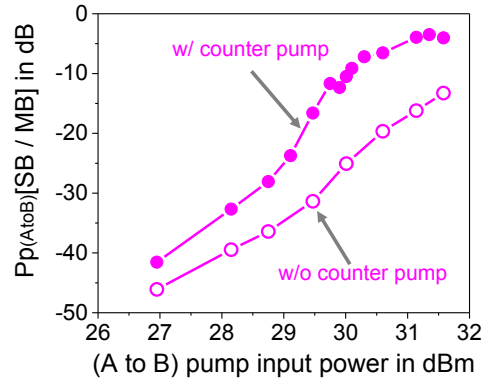


**Figure 5.9:** Growth of side-band power of the (A to B) pump (i.e., difference between the SB power and the MB power in dB) with counter pump (B to A) switched on and off. OSA resolution bandwidth = 0.5 nm.

in a straight fiber (polarization-dependent) configuration.

Figure 5.9 shows a linear increase of the SBS power with increased input pump power. However, when the counter propagating pump (B to A) together with the (A to B) pump are turned-on, the growth of the 10-GHz side-band (difference between the instantaneous side-band power and the main-band power) of the A to B pump is found to increase nonlinearly which saturates at high input pump levels as shown in Figure 5.9. The saturation is due to the fact that the growth of the side-band power cannot be larger than the main-band power of the pump. The higher levels of side-band power in the presence of counter propagating pump are due to the availability of an initial optical wave (i.e., a seed) at 10 GHz offset from the main-band of the pump at the input of the HNLF (see Figure 5.10). The seed is amplified by the counter-propagating pump through SBS. Note that even in the absence of the counter propagating pump (i.e., without B to A pump), the growth of the side band is found to fluctuate over time (although very small) and this is due to the stochastic nature of spontaneous Brillouin scattering which initiates the generated SBS [120].

This scenario is analogous to increasing the spectral width of the pump by employing more pump phase-dithering tones as discussed in Section 4.4.2. For instance, the number of RF tones in the setup in Figure 5.7 is increased from 3-RF tones to 4-RF tones. The fourth pump phase-dithering RF tone is at a frequency of 2710 MHz. Addition of the fourth RF tone increased the SBS threshold of the PM-HNLF from 30.7 dBm (with three RF tones) to 33.2 dBm. The electrical spectrum of the pump after phase-dithering is measured on an electrical spectrum analyzer for both the three and the four phase-dithering RF tones as shown

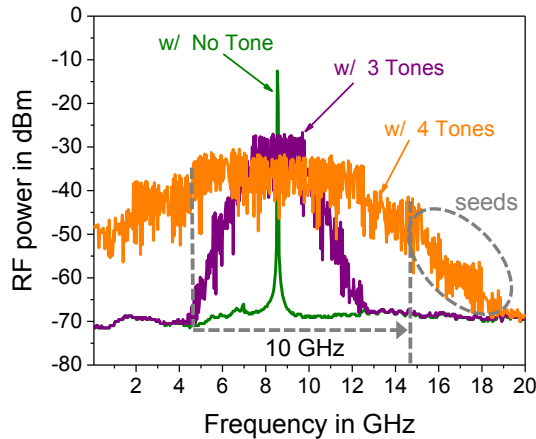


**Figure 5.10:** A heterodyne electrical spectrum of the pump laser (after the phase modulator) for the cases: (i) with no pump phase-dithering RF tone, (ii) with 3-RF phase-dithering tones, (iii) with 4-RF phase-dithering tones. Electrical spectrum analyzer resolution bandwidth = 10 MHz and video bandwidth = 10 MHz\*.

in Figure 5.10\*.

It is clear from Figure 5.10 that there is only noise floor at 10 GHz offset from the main spectral components of the pump (i.e., no seed present) in the case of phase-dithering with 3-RF tones. Therefore the generation of a 10 GHz sideband of the pump is due to the SBS of the counter-propagating pump alone (no seed present). However, in the case of pump phase-dithering with 4-RF tones or more, the spectral width of the pump already creates seeds which eventually get amplified by the SBS of a counter-propagating pump. It can also be seen from Figure 5.10 that in the case of the 4-RF tones, the relative difference between the maximum power of the seeds and that of the main-band is about 11 dB. This indicates that the seed power can be significant and it is easily enhanced by the amplification of the counter-propagating pump through SBS.

Furthermore, the pump spectra shapes for the 3- and 4-RF tones are measured, one after the other, on the optical spectrum analyzer (OSA) as shown in Figure 5.11. The pump power per direction of the PM-HNLF has been 27 dBm. The spectral width and distortion of the pump is more evident in the case of 4-RF tones (2710 MHz maximum frequency) than that of 3-RF tones (875 MHz maximum frequency). Although, the SBS in the 3-tones is more pronounced than

\*The center frequency of  $\sim 8$  GHz of the heterodyne measurement shown in Figure 5.10 is due to the difference in frequency between the LO and the pump laser under test.

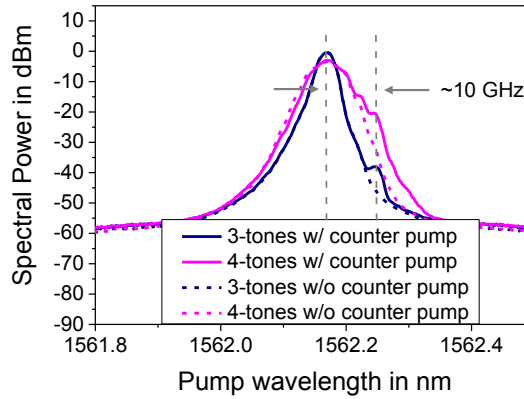


**Figure 5.11:** Optical spectrum of the pump (after 20-dB coupler) for 3- and 4-RF tones (i) with no counter propagating pump, (ii) with counter propagating pump.  $P_p = 27$  dBm at each direction of the fiber. 0.01-nm OSA resolution bandwidth.

that in the 4-tone case, pump distortion is more severe with increasing the pump bandwidth and this is due to the amplification of the already existing seed optical waves.

The growth in power of the SBS side-band on a pump causes amplitude modulation of the pump which causes the envelope of the pump (main-band and side-band powers) to oscillate in time at the Brillouin frequency [68]. This effect has severe impact on the pump leading to pump distortion [67]. The pump distortion starts with the generation of a 10-GHz side-band through SBS of the counter propagating pump. The side-band then interacts with the main-band of the forward propagating pump through FWM. The FWM process generates higher-order side-bands on the forward propagating pump as illustrated in Figure 5.12. The effects on the forward propagating pump simultaneously occur on the counter propagating pump. The impact of the pump oscillation on the signal gain has been shown theoretically in [68] and experimentally in Section 5.2.3.

The sketch in Figure 5.12 shows that as the A to B pump propagates in the HNLf, a 10-GHz shifted side-band is generated due to SBS from the counter propagating (B to A) pump wave. The side-band acts as a signal and it interacts with the main-band of the pump via FWM to produce other higher order side-bands which consequently degrades the pump's spectral shape substantially (see Figure 5.8(c)). Thus, the CW pump eventually becomes a modulated pump and the total power of its envelope (as a result of the main-band and the side-band interactions) oscillates in time. The theoretical work governing the impact of Brillouin reflections as a result of counter propagating pumps in the HNLf has been

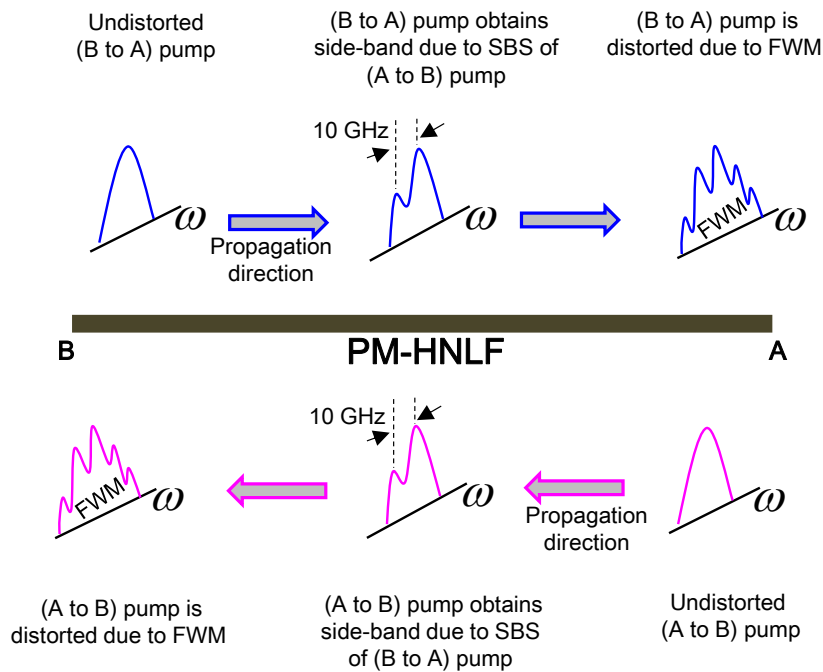


**Figure 5.12:** Schematic representation of pump evolution in the PM-HNLF showing the induced-distortion due to the SBS counter-propagation of the pump.

reported in [67] and it indicated that pump distortion as a function of the pump spectral width can be illustrated as shown in Figure 5.13.

The schematic representation in Figure 5.13 shows that there exist an optimization pump spectral width where a minimum (min) pump distortion can be obtained. For the same signal gain, a small pump spectral width will yield a high SBS side-band power whereas larger pump spectral width will result in amplification of seed optical waves (which are 10 GHz offset from the main-band of the pump) by the SBS of the counter propagating pump. Optimization of the pump

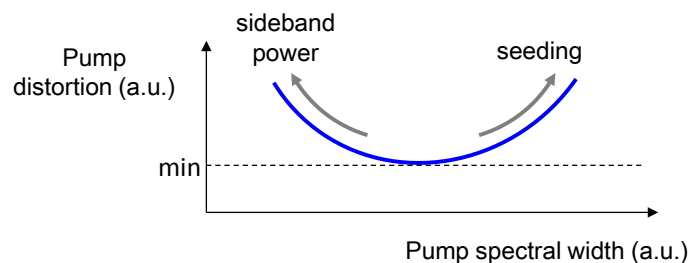


**Figure 5.13:** Schematic representation of pump distortion as a function of the total pump spectral width of a FOPA based on the polarization-diversity loop.

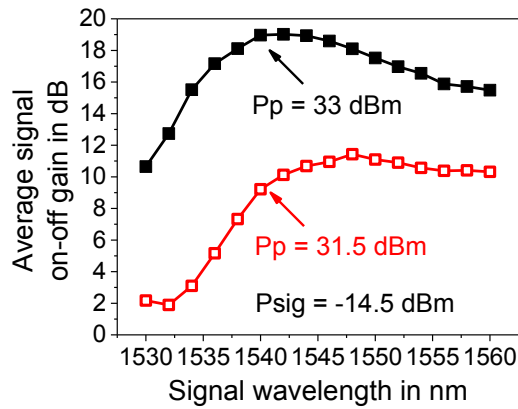
power and the total pump spectral width will yield minimum pump distortion, however, at the expense of the achievable signal gain.

The experimental measurements (which will be discussed later in this Chapter) and the analytical analysis [67] evidently show that the Brillouin reflections in FOPAs based on the polarization-diversity loop scheme can lead to severe pump distortion which eventually leads to signal distortion. The amplitude modulation of the pump (due to the side-band) can also lead to XPM on the signal. The impact of pump distortion on the modulated signal is discussed in Section 5.3. One way to minimize the SBS reflections in the loop (i.e., pushing down the curve in Figure 5.13) is to use a highly SBS-suppressed HNLF [92], [121], [47, p. 321].

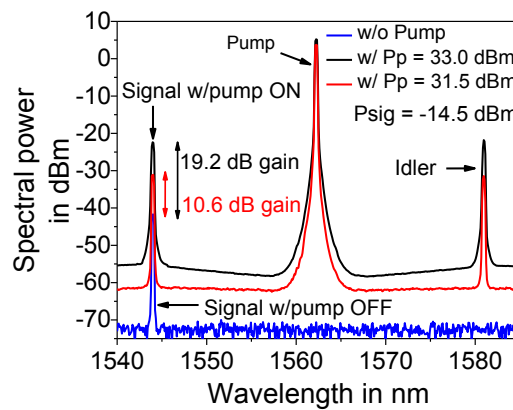
### 5.2.2 Evaluation of pump splitting optimization

The setup for the single-pump polarization-independent FOPA based on the polarization - diversity loop scheme in Figure 5.7(a) is implemented for the optimization of the pump splitting in the diversity loop as also explained in [113]. In order to obtain a high signal gain in this investigation, 4-RF pump phase-dithering tones are used. Recall that addition of the fourth RF tone increased the SBS threshold of the PM-HNLF from 30.7 dBm (with three RF tones) to 33.2 dBm. With regards to the SBS threshold by applying the 4-RF tones, the expected 35.6 dBm threshold is not achieved and this has been due to the bandwidth limitation of the used electrical amplifier.

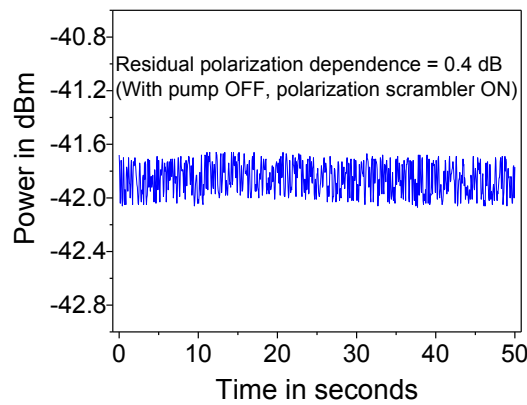
Initially, the total pump power in (both directions) the diversity loop has been set to 31.5 dBm and later to 33 dBm. For each pump power, the polarization scrambled signal is swept in wavelength from 1530 nm to 1560 nm and the signal spectrum is measured. Note that the pump wavelength is still kept at 1562.2 nm. Figure 5.14(a) shows a peak on-off gain of 19.2 dB at a signal wavelength of 1544 nm when the pump power has been 33 dBm, whereas the peak on-off gain for a pump power of 31.5 dBm is 11.3 dB at a signal wavelength of 1548 nm. It is worth noting that the average parametric signal gain (in this section of the thesis) is the average of the signal gain of both polarizations (i.e., in both directions) of the diversity loop. In other words, it is the average signal gain at the output of the diversity loop. The pump-on and -off output spectra of the signal, pump and the generated idler waves at the output of the FOPA, when the signal wavelength is set to 1544 nm, are shown in Figure 5.14(b) (OSA resolution bandwidth of 0.5 nm). The net gain of the FOPA is measured as the difference in signal powers between the output port 3 of the circulator (with pump on) and



(a)



(b)



(c)

**Figure 5.14:** (a) Average signal on-off gain spectra at  $P_p = 33$  dBm and  $P_p = 31.5$  dBm. (b) Spectra, after 20-dB coupler, at the output of the PM-HNLF showing the signal on-off gain the the generated idler with pump off and on at  $P_p = 33$  dBm and  $P_p = 31.5$  dBm. (c) Residual PDG of the FOPA with pump switched-off. OSA resolution bandwidth of 0.5 nm.

the signal power at the input of the circulator port 1. The net gain is found to be 5 dB less than the signal on-off gain due to the passive losses from port 1 to port 3 of the circulator via the diversity loop.

In order to measure the residual polarization dependence of the setup, the pump is switched off and the signal wavelength is set to 1544 nm. By varying the signal's state-of-polarization around the Poincaré sphere using the polarization scrambler, the polarization dependence of the FOPA is measured by using the zero-span function (span is set to 0 nm) of the optical spectrum analyzer. The scrambling rate of the polarization scrambler has been kept low enough (few kHz) in order to avoid power averaging at the optical spectrum analyzer and the maximum fluctuation within a temporal sweep of 50 seconds is found to be 0.4 dB as shown in Figure 5.14(c). The origin of this gain fluctuation (also known as PDG) will be explained later in this chapter.

The PDG is defined as the difference between the maximum and minimum signal gain as the signal's state-of-polarization is changed [122]. High levels of PDG cannot be acceptable in any optical network application. In order to determine the spectral dependence of the FOPA, the optimization of the pump splitting has been initially carried out for each signal wavelength at a pump power of 31.5 dBm. The summary of this optimization case is shown in Figure 5.15(a). Here, at a particular wavelength of the polarization scrambled signal, a total pump power of 31.5 dBm is sent to the diversity loop. The pump power equally divided in the arms of the loop (by adjusting the PC in front of the PBS). A minimum PDG indicates that the pump power has been equally divided into the arms of the diversity loop. This optimization of the pump splitting procedure has been carried out for all signal wavelengths (from 1530 nm to 1560 nm) and it can be seen from Figure 5.15(a) that the obtained individual PDG is less than 0.5 dB for signal wavelengths from 1536 nm to 1560 nm. Furthermore, the average PDG over the entire spectrum range (1530 nm to 1560 nm) is less than 0.4 dB. However, in a practical system, one has to set a particular pump splitting to achieve minimum PDG for all signal wavelengths at the same time. In order to do this, a signal wavelength at 1542 nm is chosen for the optimization of the pump splitting. After splitting the pump power at this wavelength, the signal wavelength is then adjusted from 1530 nm to 1560 nm and at each signal wavelength, the corresponding PDG is measured. Note that the pump splitting is carried out only once (at signal wavelength of 1544 nm). As depicted in Figure 5.15(b) the PDG is not constant over the entire spectrum and the maximum PDG is found to be

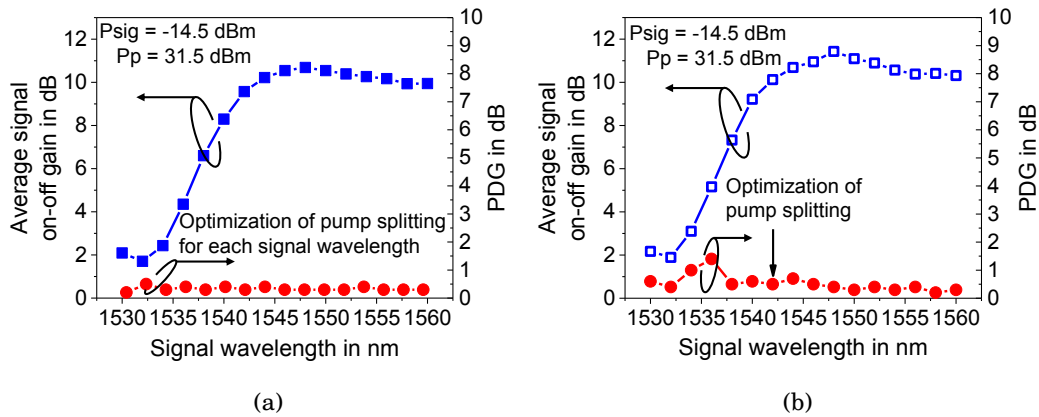


**Figure 5.15:** (a) At  $P_p = 31.5$  dBm: Optimization of pump splitting at each signal wavelength. (b) Optimization of pump splitting at a single signal wavelength of 1542 nm. Note that for a particular graph, the y-axis on the left hand side is for the average signal gain whereas the y-axis on the right hand side is for the PDG.

1.4 dB at a signal wavelength of 1536 nm whereas the average PDG is 0.5 dB. Nevertheless, the PDG is flat over the wavelength range of 1538 nm to 1560 nm with an average PDG of 0.4 dB.

In order to evaluate the performance of the optimization of the pump splitting at high gain conditions, the total pump power into the loop is increased to 33 dBm. The pump splitting is then performed individually for all the signal wavelength as is done in the low gain condition. Figure 5.16(a) is a summary of the measured PDGs values. It is clear that the obtained individual PDG is less than 1 dB for signal wavelengths from 1536 nm to 1560 nm. In addition, the PDG is higher at low signal wavelengths (e.g. 1530 nm) than in the case of higher wavelengths (1560 nm). This trend of wavelength-dependent PDG will be explained later in this Section.

Recall that in a practical system, one has to set a particular pump splitting to achieve minimum PDG for all signal wavelengths at the same time. Therefore the optimization of the pump splitting have been conducted at three additional signal wavelengths (i.e., at 1532 nm, 1540 nm, and 1544 nm). First, the optimization of the pump splitting has been performed at only a signal wavelength of 1532 nm. The measured on-off gain profile and the PDG values are as shown in Figure 5.16(b). A high PDG spectrum with an average value of 3 dB is experienced for almost all the measured wavelengths.

The additional two pump splitting optimizations are carried out at signal

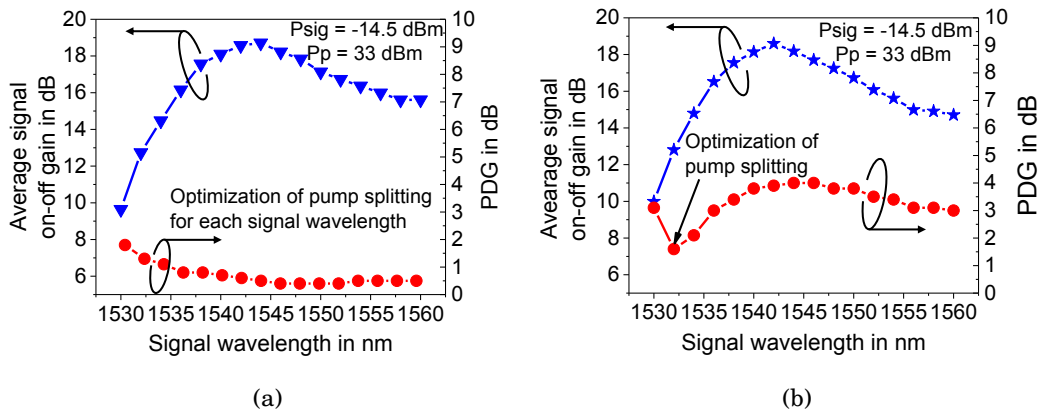


**Figure 5.16:** At  $P_p = 33$  dBm: (a) Optimization of pump splitting at each signal wavelength. (b) Optimization of pump splitting at a signal wavelength of 1532 nm. Note that for a particular graph, the y-axis on the left hand side is for the average signal gain whereas the y-axis on the right hand side is for the PDG.

wavelengths of 1540 nm (close to the gain maximum) and 1544 nm for a total pump power of 33 dBm in each case. In Figure 5.17(a), the optimization of the pump splitting has been carried out at a signal wavelength of 1540 nm. The PDG values are seen to be generally higher in this case compared to that in Figure 5.16(b), but the spectrum is sufficiently flat from 1538 nm to 1560 nm with an average PDG of 1.7 dB. However, it is clear that the signal wavelengths below 1538 nm experienced larger PDGs.

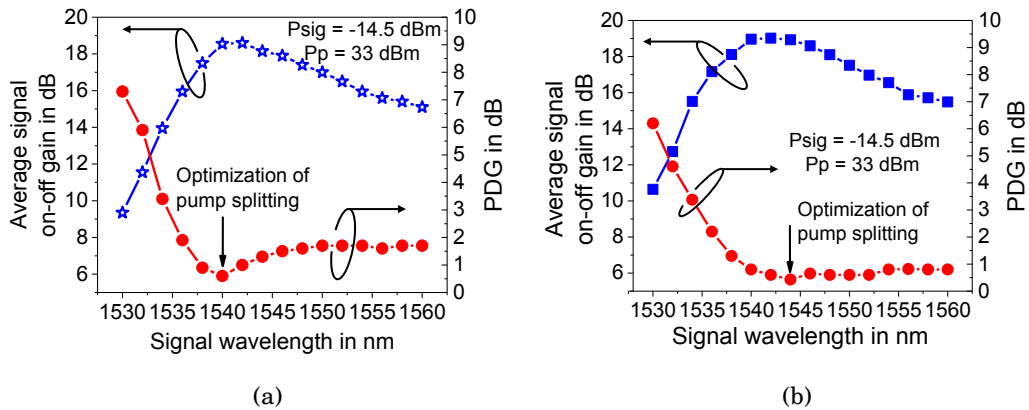


**Figure 5.17:** At  $P_p = 33$  dBm: Optimization of pump splitting at a signal wavelength of (a) 1540 nm. (b) 1544 nm. Note that for a particular graph, the y-axis on the left hand side is for the average signal gain whereas the y-axis on the right hand side is for the PDG.

Furthermore, a signal wavelength of 1544 nm is selected for the optimization of the pump splitting as shown in Figure 5.17(b). The signal wavelengths below 1540 nm showed large PDG values in this case while the PDG spectrum is seen to be almost constant among the signal wavelengths from 1542 nm to 1560 nm with an average PDG of 0.7 dB.

In all the above investigated PDG cases, it is obvious that minimization of the PDG is possible at a fixed signal wavelength by optimizing the pump power splitting at the diversity loop input. However, it will not lead to an overall minimized PDG over the amplification bandwidth. The origin of the PDG in the polarization-diversity loop, in general, will be explained in detail later in this chapter.

Nevertheless, the stability and reliability of the setup has been tested by operating the polarization-independent FOPA continuously without any interruption for 9 hours after the PDG had been optimized at a signal wavelength of 1544 nm. It is worth noting that the average room temperature has been about 25°C. The signal at 1544 nm with 19.2-dB initial gain and an initial PDG of 0.6 dB is monitored. Measurements of the signal on-off gain and the PDG are recorded every hour. It can be seen from Figure 5.18 that the average PDG after 7 hours of stable operation is 0.5 dB and the average drop in signal gain is less than 0.2 dB/hr. The reduction in gain over time is attributed to a drift of the pump polarization due to environmental changes.

Moreover, increase in PDG above the average value after 7 hours of continuous operation is observed but the values are still below 1 dB. The optimization of

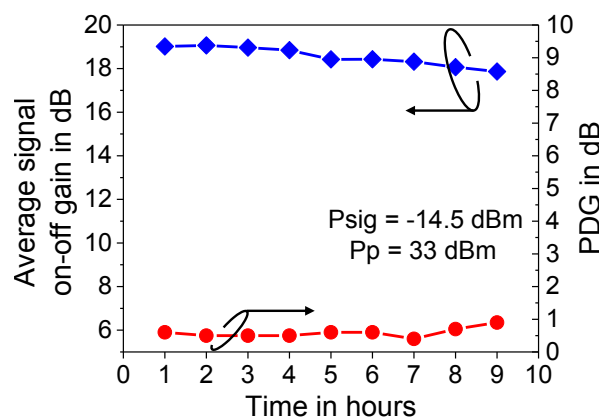


**Figure 5.18:** PDG stability monitoring of the polarization-independent FOPA over time. Note that the y-axis on the left hand side is for the average signal gain whereas the y-axis on the right hand side is for the PDG.

pump splitting in single-pump polarization-independent FOPA at high gain conditions show that it is not straightforward to achieve a low and flat PDG profile in a wide signal gain-bandwidth.

A trade-off exist between the bandwidth and lower PDGs. Also, it is seen that operating the FOPA at lower gain produced a lower and more flat PDG in a wider wavelength range compared to that obtained at high gain.

### **5.2.3 Non-reciprocal gain due to counter-propagating pumps in a polarization-independent FOPA with diversity loop**

The presence of PDG in optical amplifiers, for practical applications, is not desirable since it leads to signal distortions. Thus there is a need to investigate the source of PDG in the investigated polarization-independent FOPA. Gain reciprocity, i.e., equal gain in both directions of the polarization-diversity loop based FOPA, has been theoretically shown provided that pump depletion (or saturation regime), fiber loss, Brillouin and Raman scattering are negligible<sup>†</sup> [123]. A non-reciprocal gain has been experimentally observed in a polarization-dependent FOPA operating in the high pump-depletion regime (i.e., when one of the conditions for gain reciprocity is violated) [124]. In addition, as seen in Figure 5.8 of Section 5.2.1, the Brillouin scattering in the diversity loop can be very significant (depending on the input pump power).

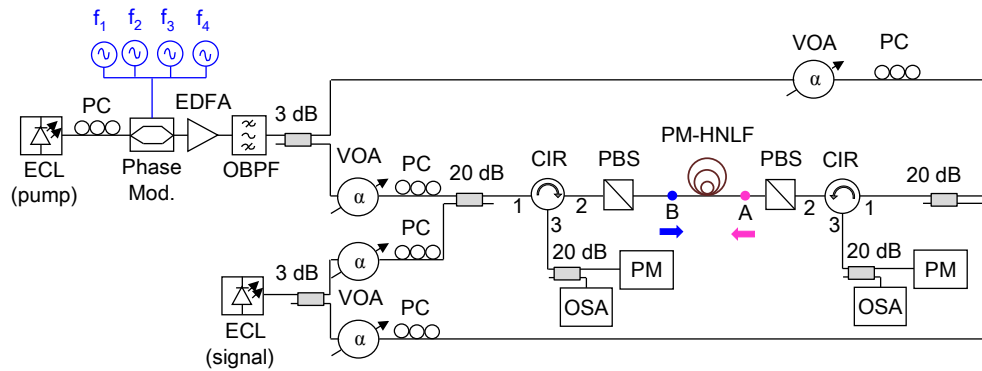
This section discusses the origin of PDG (as has been observed in Section 5.2.2) in FOPAs employing the polarization-diversity loop scheme by considering the contributions from SBS reflections in the diversity loop and also the variations of the local zero-dispersion wavelength of the used PM-HNLF.

#### **Experimental setup**

In order to investigate the measured PDG which has been discussed in the preceding section, the modified setup shown in Figure 5.19 is employed. The availability of only one high power EDFA resulted in a modification of the original setup in Figure 5.7(b). Therefore higher pump power levels (above 29 dBm) per direction of the PM-HNLF are not attainable due to the limited output power of the used single EDFA. Nevertheless, the setup still allows the independent control of the propagating pump waves in direction A to B and B to A in the polarization-independent FOPA. It is worth noting that the measurements in

---

<sup>†</sup>Remark that fulfilling all these conditions is not realistic and this indicates that practical realization of gain reciprocity in the diversity loop can be very challenging.



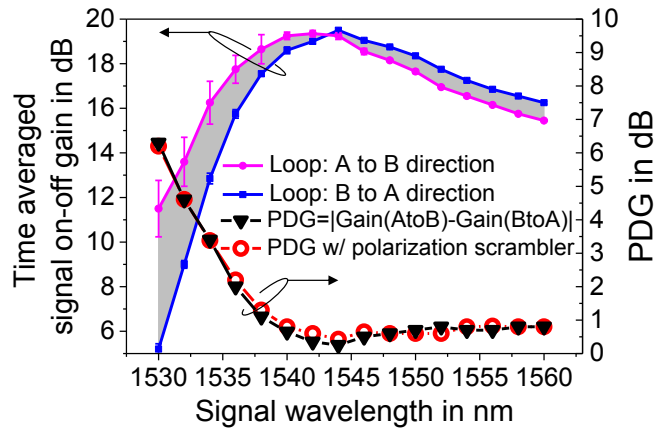
**Figure 5.19:** Schematic representation of the experimental setup depicting the modified setup of a single-pump polarization-independent FOPA based on the diversity loop scheme with four pump phase-dithering tones. (Note that a single high power EDFA is used).

Figure 5.20 and Figure 5.21 are obtained by using setup I in Figure 5.7 (and with 4-RF tones). The remaining measurements in this Section are obtained by using the new setup in Figure 5.19 unless otherwise stated.

### Discussion of results

Firstly, after optimization of pump splitting for minimum PDG of the polarization scrambled signal (using the polarization-diversity loop setup in Figure 5.7(a) and with 4 - RF tones) at 1544-nm wavelength, the polarization scrambler is switched - off after the pump splitting optimization. Then the total signal power is input to the A to B direction of the diversity loop. Note that the pump power and the signal power are still fixed at 33 dBm and -14.5 dBm, respectively. After measuring the signal gain spectrum on the optical spectrum analyzer, the total signal power is then aligned to the B to A direction and the corresponding gain spectrum is also measured. The two resulting gain spectra shapes are found to be different as shown in Figure 5.20.

Although the polarization scrambler has been switched off (and the signal aligned to one direction of the loop), the signal gain is found to fluctuate as can be seen in Figure 5.20. The magnitude of the fluctuation (which has a maximum of about 2.5 dB at 1530-nm wavelength on the A to B pump) is found to be smaller than as predicted in [68] and this may be due to: (i) the averaging of the pump oscillation by the OSA (although not fully) which is limited in tracking the nano-second fluctuations of the pump as shown in [68], (ii) the statistical nature



**Figure 5.20:** Gain spectra of the A to B and the B to A directions of the diversity loop with polarization scrambler switched-off and the absolute difference between the two gain profiles (PDG = shaded region). It also shows the comparison of the PDG due to the difference between the two gain profiles with the measured PDG when the signal is polarization-scrambled as shown in Figure 5.17(b). 0.5-nm OSA resolution bandwidth.

of the generated 10 GHz SBS on the pump, as discussed in Section 5.2.1, since the amplitude fluctuation of the side-band can lead to a change in the overall amplitude of the pump envelope. In addition, the gain fluctuations in one direction of the loop (B to A direction) is found to be smaller than that in the other direction (A to B direction) which is consistent with the theoretical work in [68]. The different gain fluctuations in both directions of the loop will be explained later in this section. Therefore the term time averaged signal on-off gain is used to indicate the averaging of the signal gain (due to pump oscillations) by the OSA.

The absolute difference between the two gain spectra resulting from both directions of the diversity loop is plotted and it is found to match the measured PDG in the polarization-independent operation (shown in Figure 5.17(b)). The two PDG curves are also shown in Figure 5.20. Therefore the cause of the PDG in the diversity loop is attributed to different gain spectral shapes in both directions of the diversity loop.

To establish the observed direction-dependent signal gain spectral shape of the PM-HNLF, the polarization-diversity loop is opened thus depicting a straight FOPA configuration (with no counter propagating pump). Initially the gain spectrum in the A to B direction is measured. Afterwards, the gain spectrum of the B to A direction is also measured. Since the FOPA is still operated in the linear

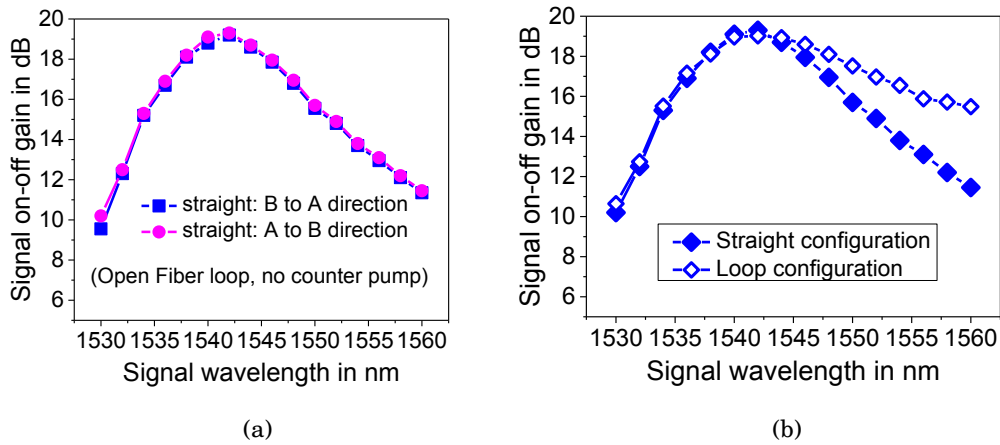


**Figure 5.21:** (a) Signal gain in an open diversity loop (i.e., depicting straight FOPA configuration) for both directions of the PM-HNLF. (b) Comparison of signal gain spectral shape of a FOPA with straight configuration and a FOPA in a polarization-diversity loop (i.e., with counter propagating pumps) at the same on-off gain. 0.5-nm OSA resolution bandwidth.

regime (no pump depletion), the signal power is still kept at -14.5 dBm per direction of the HNLF. In order to obtain the same signal on-off gain of  $\sim 20$  dB on-off gain just as in the case of the loop configuration, the pump power in one direction of the PM-HNLF (straight configuration) is increased from 30 dBm to 30.4 dBm. The measured gain spectra are found to be equal as shown in Figure 5.21(a). The measured signal gain profile obtained in the diversity loop is compared with the measured signal gain profile when the loop is opened (i.e., straight FOPA configuration) as shown in Figure 5.21(b). It is obvious that the two spectral shapes for the different cases are different. Therefore it is clear that the presence of counter propagating pumps in the diversity loop influences the signal gain spectral.

To confirm the dependence of the gain spectral shape on the presence of a counter-propagating pump in order to clarify the origin of the PDG, the modified experimental setup shown in Figure 5.19 is implemented. The maximum available pump power per HNLF direction has been 29 dBm. This pump power yields an on-off gain of  $\sim 13$  dB when both pumps are simultaneously turned-on (with counter-propagating pumps) as shown in Figure 5.22. Again, it is identified that with the presence of counter propagating pump, the gain spectral shapes per HNLF direction are different. This corresponds to the previous results of the obtained non-reciprocal spectral shape in the diversity loop as shown in Fig-

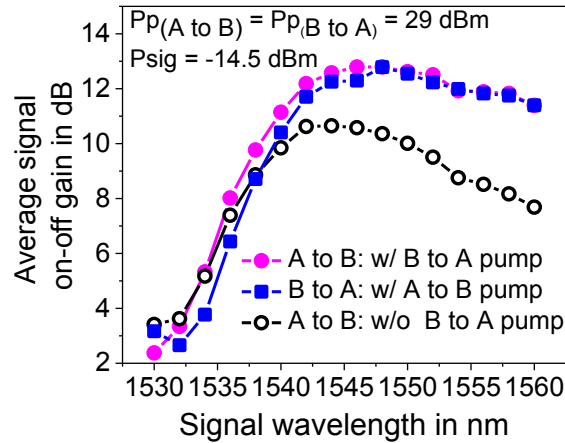


**Figure 5.22:** A to B direction gain spectra with and without B to A pump. It also shows the comparison of the gain spectra in each direction of the HNLF when both pumps are turned-on. 0.5-nm OSA resolution bandwidth.

ure 5.20. Figure 5.22 further shows the gain spectrum in the absence of the counter propagating pump (with no B to A pump) and it is clearly seen that a completely different gain spectrum is obtained. It has about 2 dB less gain than the case when there is a counter pump. The increase of the parametric gain in the case with counter pump is due to the additional instantaneous power that the 10-GHz side-band adds to the A to B pump thereby changing the overall pump envelope [68]. The parametric gain, which is an exponential function of the instantaneous pump power translates the slight increase in pump power to a higher average gain [1, 82].

### Interpretation of the origin of PDG in polarization-diversity based FOPA

In order to qualitatively explain the origin of PDG in the polarization-diversity loop, the schematic illustration in Figure 5.23 is used. Here, a 300 m HNLF is sectioned into three equal parts. A variation in the local profile of the zero-dispersion wavelength ( $\lambda_{zd}$ ) of the HNLF is assumed to be asymmetric with a 3-step profile and its wavelength is set to a lower value than the wavelength of the pump ( $\lambda_p$ ) as also shown in Figure 5.23. Where  $\lambda_{zd}^u$  and  $\lambda_{zd}^l$  are the zero-dispersion wavelength above and below the average zero-dispersion wavelength ( $\bar{\lambda}_{zd}$ ), respectively.

Initially, no Brillouin scattering is considered for both counter propagating pump waves (A to B and B to A pumps) and therefore no SBS is generated on either pump wave. In addition, the fiber loss is neglected. Thus, the total pump

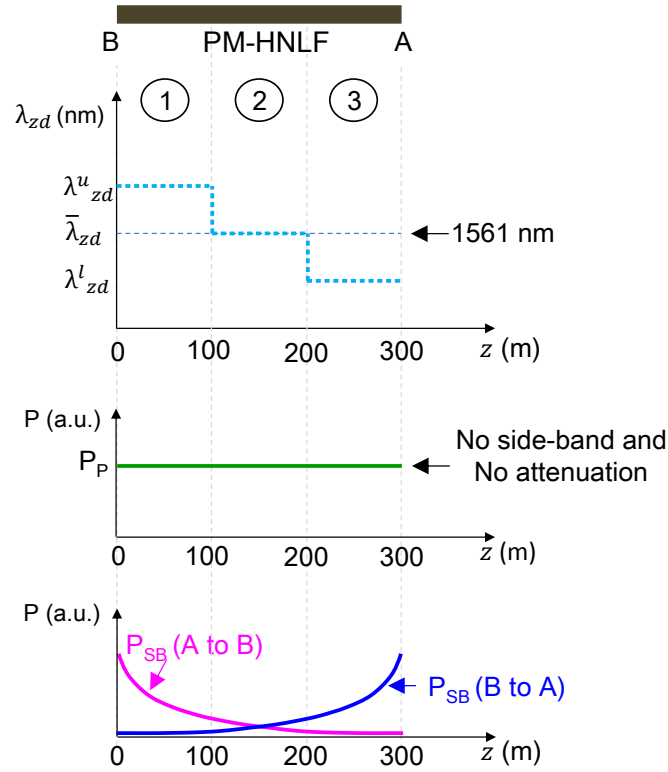


**Figure 5.23:** Illustration of non-reciprocal signal gain due to zero-dispersion wavelength ( $\lambda_{zd}$ ) variation and counter propagating pumps in polarization - diversity FOPA.

power in both directions of the HNLf are equal at any point in time (i.e., constant pump power). The total generated parametric gain (i.e., a cascade of the local parametric gain in the three sections of the HNLf) at each end of the fiber is shown as:

$$\bar{G}_{(AtoB)} = G_3[\omega_s, \lambda_{zd3}, P_p] \cdot G_2[\omega_s, \lambda_{zd2}, P_p] \cdot G_1[\omega_s, \lambda_{zd1}, P_p] \quad (5.1)$$

$$\bar{G}_{(BtoA)} = G_1[\omega_s, \lambda_{zd1}, P_p] \cdot G_2[\omega_s, \lambda_{zd2}, P_p] \cdot G_3[\omega_s, \lambda_{zd3}, P_p] \quad (5.2)$$

Where  $G_j$  ( $j = 1, 2, 3$ ) is the parametric gain per section of the HNLf. Recall from Section 4.2.1 and Section 5.1.2 that the parametric gain is a function of: (i) the signal wavelength ( $\omega_s$ ), (ii) the zero-dispersion wavelength ( $\lambda_{zd}$ ), and (iii) the pump power ( $P_p$ ), (i.e., when the FOPA is operated in a linear regime). Since  $\bar{G}_{(AtoB)} = \bar{G}_{(BtoA)}$  (from equations (5.1) and (5.2)), irrespective of the direction of the PM-HNLf, the average parametric gain ( $\bar{G}$ ) in both directions of the HNLf

(even in the presence of local zero-dispersion wavelength variation) will be the same.

Therefore the spectral shapes per direction of the fiber are the same. This is true in the absence of both attenuation and Brillouin scattering (i.e., no side-band generation) [123]. However, in the presence of Brillouin scattering, the side-band grows exponentially from the beginning of the HNLF to the end of the fiber as shown in Figure 5.23. This causes the parametric gain per section of the HNLF (especially at the extremities of the HNLF) to be different depending on the direction along the HNLF. Qualitatively, this can be represented as:

$$\begin{aligned} \bar{G}_{(AtoB)} = & G_3 \left[ \omega_s, \lambda_{zd3}, (P_p(z) + 0) \right] \cdot G_2 \left[ \omega_s, \lambda_{zd2}, (P_p(z) + \delta P_{SB}(z)) \right] \\ & \cdot G_1 \left[ \omega_s, \lambda_{zd1}, (P_p(z) + \Delta P_{SB}(z)) \right] \end{aligned} \quad (5.3)$$

$$\begin{aligned} \bar{G}_{(BtoA)} = & G_1 \left[ \omega_s, \lambda_{zd1}, (P_p(z) + 0) \right] \cdot G_2 \left[ \omega_s, \lambda_{zd2}, (P_p(z) + \delta P_{SB}(z)) \right] \\ & \cdot G_3 \left[ \omega_s, \lambda_{zd3}, (P_p(z) + \Delta P_{SB}(z)) \right] \end{aligned} \quad (5.4)$$

Where  $z$  is the fiber length.  $\delta P_p(z)$  indicates a slight increase of the SBS power, since the pump loses power to the Stokes wave (i.e., SBS) along the fiber length.  $\Delta P_p(z)$  also indicates a substantial increase of the SBS power (e.g. at the end of the fiber). It is clear from equations (5.3) and (5.4) that the parametric gain becomes a function of the side-band power of the pump. And this contributes to unequal gain per section of the HNLF (e.g. in section 3) due to the presence of asymmetry of the local zero-dispersion wavelength profile. Thus the average parametric gain ( $\bar{G}$ ), in this case, at the ends of the HNLF are different ( $\bar{G}_{(AtoB)} \neq \bar{G}_{(BtoA)}$ ) thereby rendering in a direction-dependent spectral shape.

Furthermore, the PDG values are seen to be relatively higher at lower signal wavelengths compared to those at higher signal wavelengths (e.g. Figure 5.17), relative to the pump wavelength. This wavelength-dependent PDG effect can be understood from the phase-matching condition (total phase mismatch parameter per unit length,  $\kappa = \Delta\beta + 2\gamma P$ ). Here, it is clear that in the lower signal wavelength regime (i.e., larger signal wavelength detuning from the pump), the dominant phase mismatch parameter is the linear phase term ( $\Delta\beta$ ) rather than the nonlinear phase term ( $2\gamma P$ ). Therefore the fluctuation of the local zero-dispersion wavelength parameter in the linear phase mismatch term (see Section 4.2.1) becomes the predominant source of gain fluctuation as the signal is located at much lower wavelengths from the average zero-dispersion wavelength.

This is consistent with the observations in Figure 5.4(a) and Figure 5.4(b) since signal wavelengths close to the pump (or the zero-dispersion wavelength) have less gain variation compared to the signals at lower wavelengths. Similarly, the variation of the local zero-dispersion wavelength contributes to the different gain fluctuations in Figure 5.20 and this can also be seen from the schematic representation in Figure 5.23 and from equations (5.3) and (5.4). It is worth noting that small changes in the zero-dispersion wavelength, even less than 0.1 nm, can produce large changes in the gain spectrum [59, p. 398].

It has been established that PDGs in polarization-independent FOPA based on the polarization-diversity loop scheme is as a result of the combined effect of Brillouin scattering (due to the counter propagating pumps in the diversity loop) and asymmetry of the local zero-dispersion wavelength variation in the HNLFF of the FOPA.

### **5.3 Impact of SBS-induced distortions on QPSK signal in a FOPA**

As already discussed in Section 5.2.1, the presence of Brillouin scattering in FOPAs based on the polarization-diversity loop scheme can severely distort the pump, depending on the amplitude of the 10-GHz generated side-band, as shown in Figure 5.8. Since the distortions on the pump are transferred to the signal via FWM and XPM in the FOPAs [47, 82], investigations of the impact of pump distortion, as a result of the SBS, on data signals is essential. Here, a 28-GBd single-polarization (SP) QPSK is used for the investigation.

#### **5.3.1 28-GBd single-polarization QPSK transmitter setup**

Figure 5.24 depicts the experimental setup of a 28-GBd single-polarization QPSK transmitter and it consists of an external cavity laser (ECL) with a line-width of 100 kHz. The external cavity laser is used as a CW signal source at a wavelength of 1544 nm. After amplification of the CW signal to about 18 dBm using an EDFA, the polarization of the signal is aligned, (using a polarization controller) to the principal axis of a single-polarization IQ modulator (IQ Mod.).

The IQ modulator is driven by a non-return-to-zero (NRZ)  $2^{17}$  De Bruijn sequence provided by a two channel 56 GS/s digital-to-analog converter (DAC). Specifically, the binary sequence are mapped to the in-phase and quadrature components of the IQ modulator. Two electrical amplifiers are used to boost the

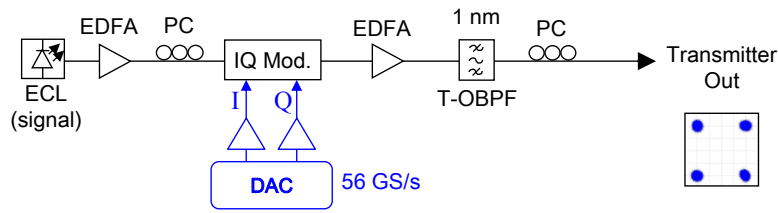


**Figure 5.24:** Experimental setup of a 28-GBd single-polarization (SP) QPSK transmitter.

power of the electrical data from the DAC to the IQ modulator. The two output channels of the DAC provided a single-polarization 28-GBd QPSK signals to the IQ modulator. After the IQ modulator, an EDFA is used to amplify the output modulated data. The out-of-band ASE noise has been suppressed using a tunable flat-top optical bandpass filter (T-OBPF) with a bandwidth of 1-nm. The polarization of the signal has been well aligned for maximum power before and after the modulator as well as at the output of the transmitter.

### 5.3.2 Coherent receiver for a 28-GBd single-polarization QPSK signal

Figure 5.25 is a schematic representation of the coherent receiver for the 28-GBd single-polarization QPSK signal that is used in the experiment. A noise loading stage is used which consists of a VOA and EDFA to set the desired OSNR of the modulated signal at the receiver. For the OSNR measurement, an optical noise bandwidth of 0.1 nm is used and a tunable flat-top optical bandpass filter with a bandwidth of 0.4 nm has been used to properly select the signal before it is coupled to a CW local oscillator in a single-polarization (2-by-4)  $90^\circ$  optical hybrid. The local oscillator (LO) had a line-width of 100 kHz.

Two balanced photo-detectors (BPD) are connected to the outputs of the optical hybrid, and a real-time sampling scope with 40-GS/s sampling rate, 20-GHz electrical bandwidth is used as analog-to-digital converter (ADC). Offline processing has been performed on a desktop computer including resampling to 2 samples per symbol,  $90^\circ$  hybrid correction, fast Fourier transform (FFT)-based frequency offset compensation, blind adaptive time domain equalization using a constant modulus algorithm, carrier phase estimation by blind phase search, de-mapping and bit-error counting [74, 75].

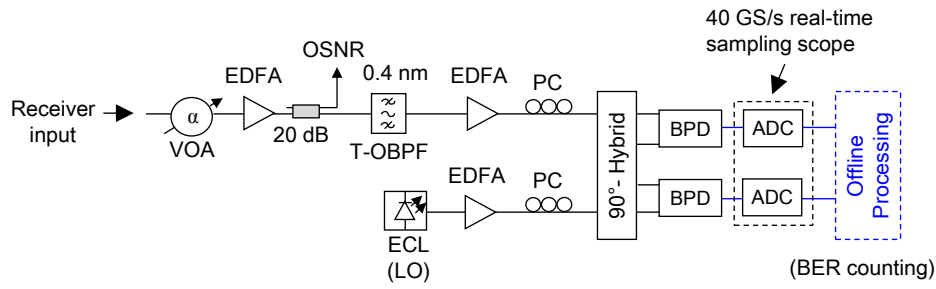


**Figure 5.25:** Experimental setup of a 28-GBd single-polarization QPSK coherent receiver.

### 5.3.3 Impact of pump distortion on 28-GBd SP QPSK signal

A modified setup of a single-pump polarization-independent FOPA based on the diversity loop scheme is implemented as a subsystem in a system experiment to investigate the impact of pump distortion transfer to a 28-GBd single-polarization (SP) QPSK data signal. Figure 5.26 shows the experimental setup. It should be noted that the fundamental description of the setup is similar to the description in Section 5.2.1. However, here, two different pump phase-dithering RF sinusoidal tone sets (frequency set I and set II) are independently used for the purpose of optimization criteria of the FOPA. For each frequency set, 3- and 4-RF tones are used for the optimization. In addition, before the receiver, a WDM coupler is used to filter only the modulated signal to the coherent receiver.

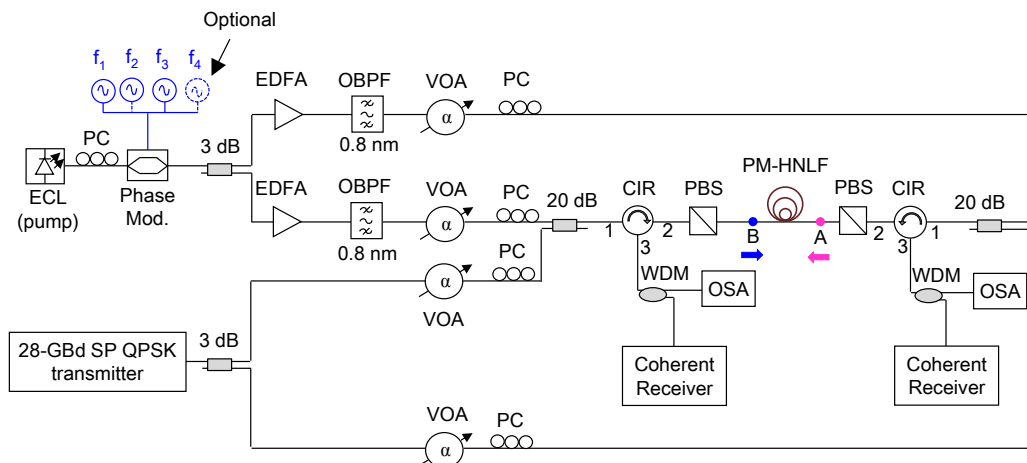


**Figure 5.26:** Experimental setup of a modified single - pump polarization - independent FOPA for the investigation of impact of pump distortion.

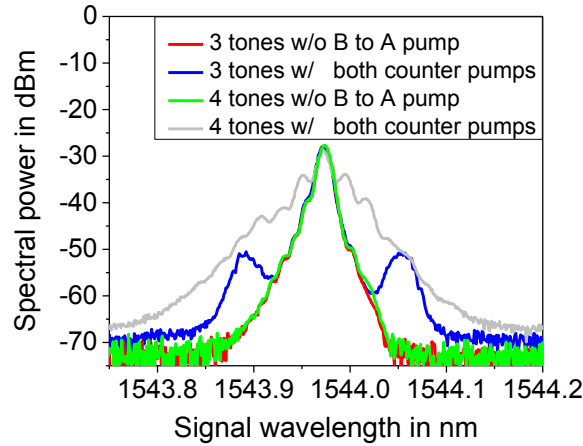


**Figure 5.27:** Optical spectra of the signal measured from the modified polarization - diversity loop with and without counter propagating pump (B to A pump). It shows the transfer of pump distortion due to pump phase-dithering (using frequency set I with up to 4-RF tones with frequencies 75, 275, 875 and 2710 MHz) to the modulated signal. OSA resolution bandwidth = 0.01 nm.

The used frequency set I is the same as the previously used pump phase-dithering tones (75 MHz, 275 MHz, 875 MHz and 2710 MHz). Whereas frequency set II consist of 55 MHz, 170 MHz, 520 MHz and 1570 MHz RF tones (i.e., with a smaller maximum frequency compared to frequency set I). The pump powers at the A to B and B to A directions of the PM-HNLF are each set to 27 dBm and the signal power per direction of the PM-HNLF is still kept at -14.5 dBm. This yields a signal on-off gain of 5 dB.

In order to verify the impact of pump distortion transfer to the data signal, initially, the optical spectra of the modulated signal is measured for frequency set I with the 3- and the 4-RF pump phase-dithering tones using the setup in Figure 5.26. Note that the spectra measurement has been obtained for only frequency set I. Figure 5.27 shows the measured spectra. It is evident from Figure 5.27 that the signal obtains stronger distortions from the pump in the case of 4-RF phase-dithering tones than in the case of 3-RF phase-dithering tones. In addition, the distortions are observed in the presence of the counter propagating pumps in both investigated RF tones. The signal distortion is due to both the pump distortion (resulting from the side-band and FWM) and XPM by the pump as discussed in Section 5.2.1.

Furthermore, the coherent receiver has been used to enable the measurement of the constellations of the modulated signal. Figure 5.28 shows a sum-

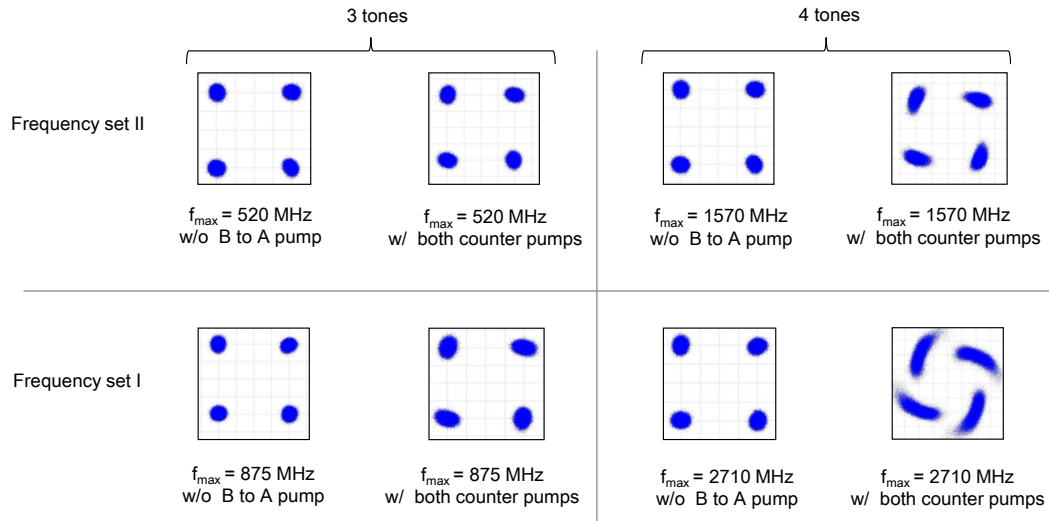


**Figure 5.28:** Constellation diagrams of the 28-GBd SP QPSK data signal (at 25-dB receiver OSNR) for the cases with and without counter propagating pump. The two different pump phase-dithering frequency sets (set I and set II) independently investigated at  $P_p = 27$  dBm and  $P_s = -14.5$  dBm per direction of the PM-HNLF. Average signal on-off gain = 5 dB.

mary of constellation diagrams of the 28-GBd single-polarization QPSK data signal for the various cases using pump phase-dithering frequency set I and set II. The observation from the constellation diagram (regarding the severity of signal distortion) is in agreement with the spectra plot in Figure 5.27. Remark that using 4-RF tones (higher number of RF tones) for the pump phase-dithering could increase the SBS threshold of the fiber, it however yields a pump with larger spectral width. The tails of the pump spectrum which are 10-GHz shifted from the main-band of the pump are amplified by the SBS of the counter propagating pump as also discussed in Section 5.2.1. Therefore the acquired signal constellation with 4-RF pump phase-dithering tones are more distorted compared to the case with 3-RF pump phase-dithering as shown in Figure 5.28. This observation is also consistent with the pump spectra in Figure 5.11. In addition, the constellation diagram of frequency set I with 3-RF tones (with maximum frequency of 875 MHz) is also worse compared to the constellation of set II with 3-RF tones of a lesser maximum frequency (i.e., 520 MHz). Therefore the larger the maximum frequency of the used pump phase-dithering tone, the wider the spectral width of the pump and the more severe the data signal is distorted. The special orientation of the constellation points is due to the fact that the phase and amplitude

distortions are correlated.

In general, the choice of the maximum frequency of the pump phase-dithering tone has a direct impact on the maximum pump power that can be transmitted through the HNLF with less pump distortion. Thus optimization of the maximum frequency of the pump phase-dithering tone and the achievable transmitted pump power is necessary. SBS threshold enhancement of HNLFs using pump phase-dithering technique employing three RF tones with reduced maximum frequency level (e.g. less than 800 MHz) such that the total pump bandwidth is well below 10 GHz, is a preferred choice for minimum pump degradation. Note that this will yield a limited polarization-independent parametric gain of about 10-15 dB [67].

It is worth mentioning that the SBS-induced pump distortion is more critical since it precedes the generation of PDG in the diversity loop. Therefore, the primary concern is to suppress the SBS in the diversity loop which will require the use of SBS-suppressed HNLFs with high nonlinear coefficients so that lower levels of pump power can yield appreciable signal gain.

## 5.4 HNLF requirement for system experiments

After a systematic characterization of a single - pump polarization-independent FOPA based on the polarization-diversity loop scheme, the following issues have to be addressed in order to implement the FOPA for system experiments:

1. SBS-induced pump distortion: In order to reduce the impact of SBS in the FOPA, HNLF with a high SBS threshold (i.e., SBS-suppressed HNLF) and with a high nonlinear coefficient can lead to better system performance. For instance, the investigated PM-HNLF has a SBS 1%-threshold (with no pump phase-dithering RF tone) of 16.5 dBm and a nonlinear coefficient of 11.2/(W·km). Thus higher pump powers will be required to obtain a significant signal gain (compared to HNLF with a higher SBS threshold and a higher nonlinear coefficient). However, as already discussed in Section 5.2.1, the higher the pump power, the higher the induced pump distortion (i.e., amplitude distortion of the pump as shown in [68]).

2. PDG: The presence of high SBS in the diversity loop is the *primary* problem since the occurrence of PDG in the diversity loop is dependent on SBS. SBS in the presence of asymmetric local zero-dispersion-wavelength fluctuations of the used HNLF yields PDG as discussed in Section 5.2.3. The higher the SBS in

Parameter	Symbol	Unit	PM-HNLF	non-PM-HNLF
SBS threshold at 1550 nm	$P_{th}$	dBm	16.5	18.4
Nonlinear coefficient	$\gamma$	/(W·km)	11.2	16.3
Length	$L$	m	300	300
Effective area at 1550 nm	$A_{eff}$	$\mu\text{m}^2$	11.9	8.6
Loss coefficient at 1550 nm	$\alpha$	dB/km	0.84	1.4
Dispersion slope at 1550 nm	$S$	ps/(nm <sup>2</sup> ·km)	0.02	0.019
Dispersion at 1550 nm	$D$	ps/(nm·km)	-0.22	-0.1
Zero-dispersion wavelength	$\lambda_{zd}$	nm	1561	1555.6

**Table 5.1:** Comparison of fiber specifications of a PM-HNLF and a non-PM-HNLF.

the diversity loop, the stronger the PDG. In addition, the higher the local zero-dispersion wavelength fluctuations, the higher the PDG. The presence of PDG in a FOPA also degrades the quality of the data signal.

Based on this analysis, another HNLF which is a non-PM-HNLF (i.e., conventional HNLF) has been selected and compared with the PM-HNLF using the fiber specifications as shown in Table 5.1. It can be seen that the conventional HNLF has a higher SBS threshold and a higher nonlinear coefficient values than that of the PM-HNLF. In conventional HNLF, the light waves do not travel in the same polarization mode as in the case of PM-HNLF (when implemented in a polarization-diversity loop scheme). Therefore, for the same pump power, the SBS-induced distortion of the pump in conventional HNLF is expected to be smaller than that in PM-HNLF. Nonetheless, for system experiments, a stable polarization in a FOPA employing conventional HNLF is challenging to achieve. However, based on the high nonlinear coefficient and SBS threshold, as shown in Table 5.1, the conventional HNLF will yield better performance since the expected SBS-induced pump distortion will be minimum. Therefore the conventional HNLF is selected for characterization and it is implemented in a polarization-independent FOPA employing the diversity loop scheme and the FOPA is used as an OPC device. The detailed discussion of the performance evaluation of the OPC device is presented in Chapter 6. The implementation of the OPC device in a transmission system for Kerr nonlinearity compensation is also discussed in Chapter 7.

## 5.5 Summary

In this chapter, systematic experimental characterizations of both a single-pump polarization-dependent FOPA and polarization-independent FOPA based on po-

larization - diversity loop scheme have been investigated. Particularly, since one of the main differences between a polarization-dependent FOPA and polarization-independent FOPA based on the polarization-diversity loop scheme is reflections in the loop, the impact of Brillouin reflections (in the polarization-diversity loop) on the FOPA pump was also investigated. Higher pump powers (which is desired for higher signal gain) in the diversity loop acquires significant distortions due to higher Brillouin reflections in both directions of the loop. A 10-GHz shifted Brillouin side-band is created on a pump by the counter propagating pump. The side-band experiences four-wave mixing with the main-band of the pump thereby distorting the pump spectral shape significantly. It was also observed that the wider the pump spectral width (due to pump phase dithering), the more severe the pump distortion in the loop due to the amplification of seed waves (i.e., spectral components which are 10-GHz shifted from the main-band of the pump) by the counter pump. The generation of a side-band on the pump has been shown to generate amplitude modulation of the pump [125]. The amplitude modulated pump and XPM generated by the pump eventually degrades the signal quality. Distortion of a 28-GBd single-polarization QPSK data signal due to Brillouin reflections in a single-pump FOPA employing the polarization-diversity loop scheme has been investigated.

Another parameter which also degrades the signal in the diversity loop scheme is PDG. The origin of PDG in a single-pump FOPA based on the polarization-diversity loop technique has also been experimentally investigated. The PDG was found to evolve from the combined effect of SBS and an asymmetric local profile of the zero-dispersion wavelength in the HNLF of the FOPA. This qualitative analysis is also consistent with the theoretical work in [125].

## Chapter 6

# Design of a FOPA-based OPC Device

Optical phase conjugation (OPC) is a well-known phase conjugation technique for compensation of chromatic dispersion and fiber nonlinear impairments of a signal in an optical transmission link [16, 37, 40, 126]. Phase conjugation of an electric field in the electrical domain has also been reported [13, 28, 127]. Recall that the optical domain provides real-time compensation without the need for electronic signal processing and with a reduced latency.

In order to design a good fiber-based OPC device employing the polarization-diversity loop scheme, the Brillouin-induced distortions which have been investigated in Chapter 5 must be considered. In this context, a fiber-based polarization-independent OPC device employing the diversity loop scheme is designed and investigated in this Chapter. The first section of the Chapter discusses the fundamentals of an OPC device in a transmission system. In order to realize an OPC device with a broad and flat gain-bandwidth, a dual-pump polarization-independent fiber-based optical parametric amplifier (FOPA) is used. A conventional HNL is used for the implementation of the FOPA. System performance and evaluation of the OPC device using a 28-GBd PDM 16-QAM signals for both single-channel and 5-channel WDM scenario at 50-GHz channel spacing in a back-to-back testbed is also investigated. The relative performances of the amplified signal and the idler are evaluated in terms of polarization sensitivity and the bit-error ratio (BER), highlighting the key optimization aspects for the successful design of a black-box OPC device.

## 6.1 Fundamentals of optical phase conjugation

The physical phenomenon governing OPC operation in HNLF (or third-order nonlinear susceptibility effect,  $\chi^{(3)}$ , media) is four-wave mixing [128]. However, the use of second-order nonlinear susceptibility effect,  $\chi^{(2)}$ , based on difference - frequency generation, in other nonlinear media such as periodically-poled lithium-niobate (PPLN) to realize phase conjugation has also been reported [16, 40–42].

Basically, application of OPC in a transmission link for distortion compensation relies on the mid-link spectral inversion technique [37, 40, 126]. In this configuration, the OPC device is placed in the *middle* of the entire transmission link or *symmetrically* placed between the fiber spans in the transmission link (in the case of cascaded OPCs). Specifically, precise middle-point location of the OPC in link is not the criteria to achieve optimum OPC performance but symmetric accumulated dispersion and signal power profiles around the OPC device is required [14]. Different link configurations with OPC will be discussed in detail in Chapter 7. Nevertheless, different position allocation of the OPC unit in the transmission link other than the mid-link technique have also been studied [83].

Recalling the nonlinear Schrödinger equation (NLSE), from Chapter 3 Section 3.3.2, the evolution of the propagation of a signal with an electric field,  $A$ , in a transmission link in the presence of fiber nonlinearity is described as [59, p. 35]:

$$\frac{\partial A(z, T)}{\partial z} = -\frac{\alpha}{2}A(z, T) - j\frac{\beta_2}{2}\frac{\partial^2 A(z, T)}{\partial T^2} + \frac{\beta_3}{6}\frac{\partial^3 A(z, T)}{\partial T^3} + j\gamma|A(z, T)|^2 A(z, T) \quad (6.1)$$

$$\frac{\partial A^*(z, T)}{\partial z} = -\frac{\alpha}{2}A^*(z, T) + j\frac{\beta_2}{2}\frac{\partial^2 A^*(z, T)}{\partial T^2} + \frac{\beta_3}{6}\frac{\partial^3 A^*(z, T)}{\partial T^3} - j\gamma|A^*(z, T)|^2 A^*(z, T) \quad (6.2)$$

Equation (6.1) describes the evolution of the signal field,  $A(z, T)$ , in the fiber and the evolution of the conjugated field,  $A^*(z, T)$ , after the OPC device is also described by equation (6.2). The parameters in equations (6.1) and (6.2) have been discussed in Section 3.3.2. It is worth noting that as a result of the phase conjugation achieved by the OPC device, the signs of the GVD ( $\beta_2$ ) and the nonlinear coefficient ( $\gamma$ ) in the NLSE are reversed. Therefore, these two effects can be compensated at the end of the transmission by the OPC. A schematic analogy is shown in Figure 6.1.

As shown in Figure 6.1, the total transmission link is made of 2-spans with total length of  $L$  km (i.e., each span is  $L/2$  long) and the OPC is placed in the

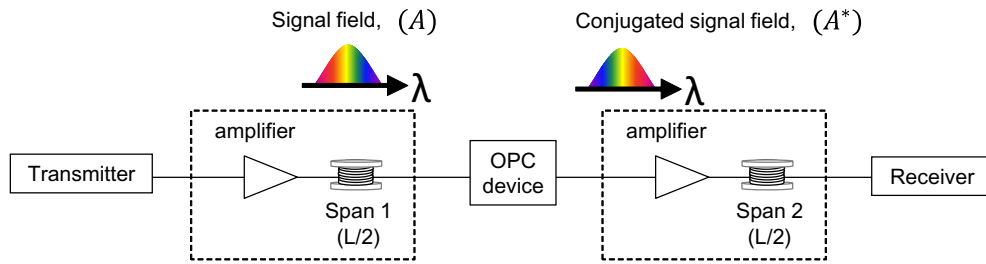


**Figure 6.1:** Schematic representation of a mid-link OPC device in a 2-span transmission link showing the spectrum of the signal before and after the OPC unit.

middle of the link. After the signal has propagated over a length of  $L/2$ , the conjugated signal copy which is generated by the OPC is propagated (signal is suppressed at the output of the OPC) over the remaining transmission length of  $L/2$ . The accumulated chromatic dispersion and the nonlinear impairments, resulting from a nonlinear phase-shift due to SPM and XPM, in the first half (i.e., before the OPC device) can be compensated for in the second half of the link (i.e., after the OPC device) by propagating the conjugated signal (instead of the signal) in the second half of the transmission link. The fiber loss,  $\alpha$ , in equations (6.1) and (6.2) is compensated for by the gain of the optical amplifier (e.g., EDFA) in the transmission link.

### 6.1.1 Limitations of OPC based on mid-link spectral inversion

It is clear from equations (6.1) and (6.2) that, after transmission over the entire transmission length, the OPC is capable of compensating for both the second-order dispersion (i.e., GVD or  $\beta_2$ ) and the fiber nonlinear impairments (i.e.,  $\gamma$ ). However, the magnitude of the third-order dispersion ( $\beta_3$ ), which also related to the dispersion slope, doubles at the end of the link. Therefore, efficient distortion compensation by the OPC is compromised by the accumulated dispersion slope. Since the signal and its conjugated copy have different wavelengths, they experience different dispersions due to the dispersion slope. Hence slope compensation is necessary in order to maximize the efficiency of the OPC device for distortion compensation [33, 129, 130]. Another limiting parameter of the mid-link OPC is the inter-channel nonlinear cross-talk. As a result of dispersion slope, neighboring channels in a WDM system experience different nonlinear inter-channel cross-talk before and after the OPC device in the link [33, 129, 130].

The impact of PMD also becomes significant especially in long transmission lengths and also in fibers with high PMD coefficients. As discussed in Section 3.2.3, PMD causes the propagating wave to broaden and as a result of its stochastic nature, its compensation by OPC can be challenging [16].

### **6.1.2 Requirements for an efficient OPC device**

A practical OPC device should provide broadband (capable of WDM operation) with flat gain-bandwidth profile. In addition, a polarization-independent operation as well as wavelength and modulation format transparency of the OPC is a pre-requisite. Furthermore, the OSNR implementation penalty of the OPC device must be sufficiently low. One way to achieve low OSNR implementation penalty is by using an OPC device which has a positive conversion efficiency (CE) [45]. The conversion efficiency in this thesis is defined as the ratio of the idler power at the output of the HNLF to the signal power also at the output of the HNLF with pump switched-off [47, p. 48].

It is worth noting that for efficient OPC operation, the dispersion map of the used fiber spans and the power profile of the propagating signal have to be symmetric around the mid-link OPC and this can be achieved by a proper design of the entire transmission link. This will be discussed in Chapter 7.

## **6.2 Experimental realization of OPC device**

Practical implementation of OPC device does not only require polarization - independent operation, but also a flat gain-bandwidth of the OPC device is desirable for WDM applications. A dual-pump polarization-independent FOPA fulfills these requirements as discussed in Chapter 4. In addition, a dual-pump FOPA allows the provision of counter-phasing mechanism which enables the suppression of pump phase-dithering tones transferred from the pumps to the generated idler(s) in the OPC as already discussed in Section 4.4.2. It is worth noting that based on the optimization measurements in Chapter 5 Section 5.3.3, two pump phase-dithering tones are used in this experiment so as to minimize the Brillouin-induced pump distortion in the diversity loop. Therefore, the maximum frequency of the pump phase-dithering tones (i.e., 253 MHz) has been selected. This frequency is smaller than that of the investigated frequencies in Section 5.3.3.

Furthermore, a non-PM-HNLF (see Table 5.1 in Section 5.4) with high SBS

threshold (18.4 dBm) and high nonlinear coefficient (16.3 /(W·km)) has been used in this experiment. Since a lower pump power is required (for this conventional HNLF) in order to achieve the same parametric gain compared to that of the already investigated PM-HNLF in Chapter 5, a less SBS-induced pump distortion is expected. However, with regards to polarization, a stable polarization in a FOPA employing conventional HNLF is challenging to achieve. In addition, as a result of low birefringence of conventional fibers, polarization rotation of the light waves (due to the random variation of the birefringence of the fiber) is undesirable since any polarization misalignment between the interacting waves in the FOPA affects the phase-matching condition [131], [82, p. 343]. Note that the polarization-diversity loop scheme in Figure 4.6(ii) (Section 4.3) is implemented in order to realize the dual-pump polarization-independent FOPA. It is worth mentioning that the type of dual-pump FOPA (i.e., OPC device) configuration (i.e., regarding allocation of the pumps and the signal frequencies) used in this experiment is similar to that shown in Figure 4.3 in Chapter 4.

### **6.2.1 28-GBd PDM 16-QAM transmitter setup**

The experimental setup of a 28-GBd PDM 16-QAM transmitter is shown in Figure 6.2. It consists of five ECLs which are used as CW WDM signal sources. The signals are placed 50-GHz apart on the International Telecommunication Union -Telecommunication Standardization Sector (ITU - T) grid with wavelengths 1549.32 nm, 1549.72 nm, 1550.12 nm, 1550.52 nm and 1550.92 nm. The WDM channels are combined with an optical coupler and after amplification with an EDFA, the total signal is modulated with a single-polarization IQ modulator (IQ Mod). The IQ modulator is driven by a NRZ  $2^{18}$  De Bruijn sequence provided by a two channel 56 GS/s DAC. Specifically, the binary sequence are mapped to the in-phase and quadrature components of the IQ modulator. Two electrical amplifiers are used to boost the power of the electrical data from the DAC to the IQ modulator. The two output channels of the DAC provided a single-polarization 28-GBd 16-QAM signals to the IQ modulator. The two output channels of the DAC provide the in-phase (I) and quadrature (Q) components of a single-polarization 28-GBd 16-QAM signals to the IQ modulator.

A polarization multiplexing emulator (PolMux) is used to generate a polarization - division multiplexed (PDM) signal. Specifically, the polarization beam splitter (PBS) at the input of the polarization multiplexing emulator splits the single-polarization data into its orthogonal polarization components by adjust-

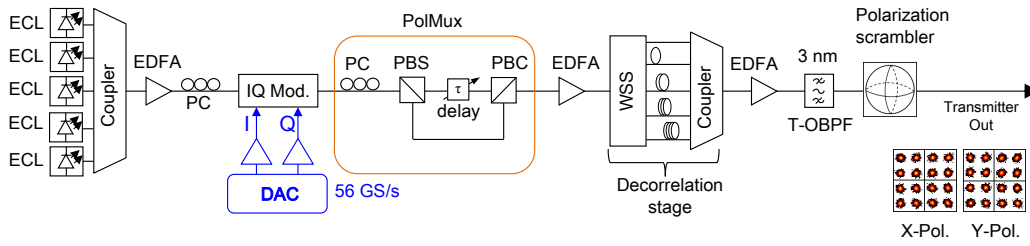


**Figure 6.2:** Experimental setup of a 5 - channel 28 - GBd PDM 16-QAM transmitter.

ing the polarization controller (PC) in front of the polarization beam splitter. After delaying one of the polarizations by 500 symbols, using a delay line, the polarizations of the delayed and undelayed data are recombined by a polarization beam combiner (PBC). Thus a PDM data signal is obtained at the output of the polarization multiplexing emulator stage. After separating all the WDM channels using a wavelength-selective switch (WSS), the channels are individually decorrelated by delaying the symbols of the neighboring channels by a minimum of 100 symbols using various lengths of standard single-mode fiber (SSMF) patch cords in the individual optical paths [132]. All five WDM channels are recombined with an optical coupler and the 28-GBd PDM 16-QAM signals are amplified with an EDFA. After suppressing the out-of-band ASE noise with an optical bandpass filter (OBPF) with a bandwidth of 3 nm, the SOP of the data signal is randomized on a Poincaré sphere using a polarization scrambler before the data signal is sent out from the transmitter.

### 6.2.2 Setup of a coherent receiver for a PDM 16-QAM signals

Figure 6.3 shows the experimental setup of a standard polarization-diverse [72, p. 103] coherent receiver. The coherent receiver uses a VOA and EDFA for the purpose of noise-loading on the data signal in order to set the desired OSNR of the signal at the receiver. For the OSNR measurement, an optical reference noise bandwidth of 0.1 nm is used.

A tunable flat-top optical bandpass filter (T-OBPF) with a bandwidth of 0.4 nm is used to select the data signal channel under test before it is combined with a CW local oscillator in a (2-by-8)  $90^\circ$  optical hybrid. The LO has a line-width of 100 kHz. Four balanced photo-detectors (BPD) are connected to the hybrid outputs, and a real-time sampling scope (RTO) with 40-GS/s sampling rate and 20-GHz electrical bandwidth is used as analog-to-digital converter (ADC). Offline

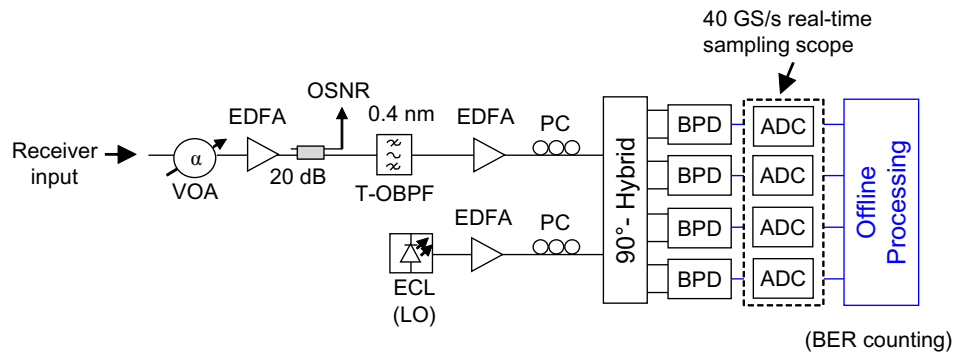


**Figure 6.3:** Experimental setup of a 28-GBd PDM 16-QAM coherent receiver.

processing of the data is performed on a desktop computer. The receiver DSP includes resampling,  $90^\circ$  optical hybrid correction, frequency offset compensation, blind adaptive time-domain equalization using a constant-modulus algorithm and multi-modulus algorithm, carrier-phase estimation by blind phase search, de-mapping, and bit-error counting [74, 75].

### 6.2.3 Design of a FOPA-based OPC device

A dual-pump polarization-independent FOPA is employed for the design of the OPC device. The experimental setup of the OPC unit is as shown in Figure 6.4. It consists of two external cavity lasers (ECLs) which serve as CW pump sources at the C-band and L-band windows with wavelengths of 1534 nm and 1574 nm, respectively. The C-band laser has a line-width and relative intensity noise (RIN) of 25 kHz and -165 dB/Hz, respectively. Whereas the L-band laser has a line-width and RIN of 100 kHz and -145 dB/Hz, respectively. The pumps are separately modulated using the phase modulators (Phase Mod.) in order to increase the SBS threshold of the used HNLF of the OPC device as also discussed in Section 5.1.1. The phase modulators are driven in a counter-phasing fashion (see Section 4.4.2 in Chapter 4) by two sinusoidal tones of frequencies 69 MHz and 253 MHz, generated by a two-channel arbitrary waveform generator (AWG), at a modulation index of about 1.4 radians. A smaller maximum frequency of the pump phase-dithering tones (i.e., 253 MHz) has been selected in order to minimize the impact of SBS-induced pump distortion as already discussed in Section 5.3.3. In addition, the focus of the FOPA is not for in-line amplification (i.e., high parametric gain). Thus low signal gain with positive conversion efficiency will be sufficient to realize good performance of the OPC device. In order to achieve the targeted modulation index, independent control of the amplitude and phase

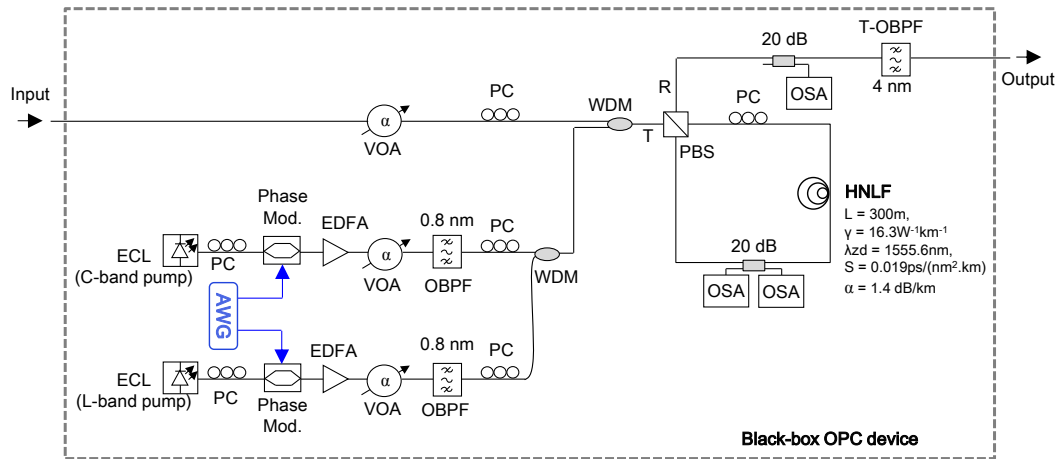


**Figure 6.4:** Experimental setup of a black-box OPC device based on a dual-pump polarization-independent FOPA. Note that a non-PM-HNLF is used.

of the frequency tones are necessary. This optimization procedure is enabled by the arbitrary waveform generator.

After amplifying the pumps with EDFAs, the pumps OSNR are measured to be 59 dB and 56 dB for the C- and L-band pumps, respectively. The pump power levels are controlled using the variable optical attenuators (VOAs) thus ensuring constant pumps OSNR values. The out-of-band ASE from the EDFAs is suppressed by using an optical bandpass filter with a bandwidth of 0.8 nm. The C- and L-band pumps are combined together using a WDM coupler before the signal (from the transmitter) is added to the pumps, by using a second WDM coupler, before being sent to the polarization-diversity loop via the polarization beam splitter (PBS). A conventional HNLF has been used as a nonlinear medium and it has length ( $L$ ), zero-dispersion wavelength ( $\lambda_{zd}$ ), nonlinear coefficient ( $\gamma$ ), attenuation ( $\alpha$ ), dispersion slope ( $S$ ) of 300 m, 1555.6 nm, 16.3  $/(W \cdot km)$ , 1.4 dB/km, and 0.019 ps/(nm<sup>2</sup>·km), respectively. The HNLF also has a 1%-SBS threshold of 18.4 dBm (i.e., without any SBS threshold enhancement technique) and after pump phase-modulation (with 2-RF tones) the SBS threshold of the fiber increased to 27.5 dBm (indicating 9.1 dB increase of the SBS threshold).

Using the variable optical attenuator (VOA), the total power of the polarization-scrambled signal at the PBS input or the transmit port (i.e., port-T) is kept constant at -5 dBm throughout the evaluation, except for the saturation analysis. This power is used in order to operate the FOPA in the linear regime [108]. In addition, the total pump power into the loop has been set to 28.2 dBm, 29.9 dBm,

and 30.8 dBm in order to achieve 5-dB, 10-dB, and 13-dB signal on-off gain values, respectively. The signal and pump power levels have been chosen such that the difference between the pump power and the total signal power at the output of the HNLF is well above 17 dB so as to avoid high nonlinear distortions in the FOPA as demonstrated in [108].

In order to match the parametric signal gain in both directions of the diversity loop at a particular pump power, the SOP of the pumps has been properly set by adjusting the polarization controllers (PCs) on each pump path before the polarization beam splitter, while monitoring the power levels on an optical spectrum analyzer (OSA) via the 20-dB coupler in the diversity loop. Proper adjustment of the PC in the loop ensures that the light waves at the output of the HNLF exit at the reflect port (i.e., port-R) of the polarization beam splitter. The output spectra after the diversity loop are monitored by an optical spectrum analyzer via a 20-dB coupler at the output of the diversity loop. At the output of the diversity loop, a tunable flat-top optical bandpass filter with 4-nm bandwidth has been used to suppress the pumps. At the same time, the filter selects either the amplified signal or the idler bands depending on the channel(s) of interest .

#### **6.2.4 OPC device performance evaluation**

The transfer of pump phase-dithering tones to the generated idler in a FOPA strongly degrades the quality of the idler. Therefore after connecting the OPC device between the transmitter and the coherent receiver, the undesirable effect of pump phase-modulation transfer to the generated idler has been minimized.

In order to do this, the counter-phasing technique (as discussed in Section 4.4.2) is implemented and optimized using a single-channel CW (unmodulated) signal at a wavelength of 1550.12 nm injected into the FOPA. Note that the IQ modulation has been turned-off and the polarization-division multiplexing emulator is by-passed so as to obtain an unmodulated signal from the transmitter. The pumps and the CW signal are aligned in one state-of-polarization and propagated in one direction of the HNLF of the FOPA. By heterodyning the local oscillator and the generated idler at the receiver, the spectrum of the idler is detected and monitored, using the real-time oscilloscope. The real-time oscilloscope enables the assessment of the strength of phase-modulation RF tones at 69 MHz and 253 MHz being transferred from the pumps to the idler.

Proper adjustment of the phase delay and amplitude parameters of the RF modulation tones, using the arbitrary waveform generator, ensure substantial

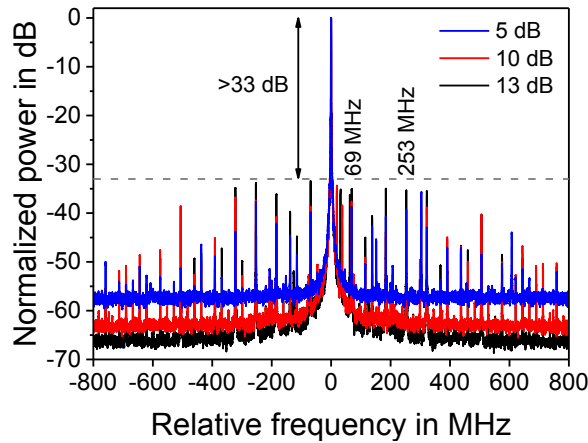


**Figure 6.5:** Acquired idler electrical spectra from real-time oscilloscope (RTO) showing suppression of pump phase - dithering tones on the generated idler.

suppression of the pump phase-modulation on the idler as shown in Figure 6.5. The suppression technique of the pump phase-modulation on the idler is carried out for 5-dB, 10-dB, and 13-dB signal on-off gain values. It is clear from the electrical spectrum of the idler, shown in Figure 6.5, that regardless of the gain values, the suppression ratio between the carrier and the two modulation tones (69 MHz and 253 MHz) and their harmonics is higher than 33 dB. This indicates that low pump phase-modulation tones are transferred to the idler.

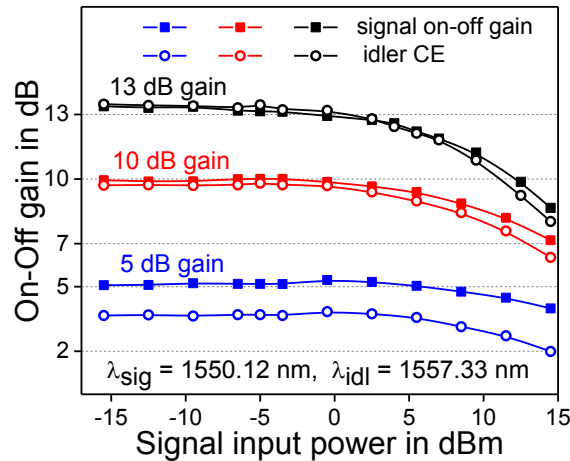


**Figure 6.6:** Gain saturation characteristics of the FOPA-based OPC device.

Figure 6.6 shows the signal on-off gain and idler CE as functions of the signal power at the polarization beam splitter input. This particular characterization has been done in a polarization-dependent configuration (the polarizations of the

pumps and the CW signal at 1550.12 nm are aligned to propagate in only one direction of the diversity loop without polarization scrambling). As expected, the difference between the signal on-off gain and the idler CE decreases with increasing the parametric gain [1]. Again, higher signal gains begin to saturate at lower input powers than lower gain levels as also discussed in Chapter 5 Section 5.1.3. However, gain reduction of 1 dB is obtained at a signal input power of 5 dBm even when the gain is 13 dB.

For the gain-bandwidth measurement of the polarization-independent OPC device, the second WDM coupler for combining the signal and the pumps in Figure 6.4 is temporarily replaced with a 10-dB coupler. After pump splitting optimization using a polarization-scrambled cw-probe signal at a wavelength of 1550.12 nm, the gain-bandwidth characterization is performed. It is worth noting that the pump splitting technique is carried out for both pumps one at a time (see Chapter 5 Section 5.2.1 for discussions on pump splitting). Then the wavelength of the single-channel CW signal is swept from 1535 nm to 1572 nm. The results of the polarization-independent average gain-bandwidth measurement are summarized in Figure 6.7(a) and it can be seen that a flat gain with 1-dB bandwidth of 24 nm at 5-dB on-off gain reduces to 18 nm when the gain is increased to 13 dB. Furthermore, a slight gain-tilt resulting from the Raman effect is also visible though its impact is kept low by setting the C-band pump power  $\sim 1.8$  dB higher than the L-band pump power.

In order to evaluate the PDG performance of the device, the IQ modulation is turned-on and the polarization-division multiplexing emulator is still by-passed.

This indicates a single-polarization 28-GBd 16-QAM single-channel polarization-scrambled data at the output of the transmitter. By using the zero-span function (span is set to 0 nm), the PDG is measured as also discussed in Section 5.2.2. Averaging effects in the PDG measurement are minimized by the use of a low scrambling rate. The wavelength of the polarization-scrambled data signal has been varied from 1542.5 nm to 1565 nm, i.e., the flat region of the gain-bandwidth profile.

Figure 6.7(b) illustrates the measured PDG for the modulated signal and its idler. The measurement is done for 5-dB, 10-dB, and 13-dB gain showing low PDG values ranging from 0.2 dB to 0.5 dB with similar signal and idler values. This indicates the effectiveness of the implemented counter-phasing techniques for suppression of the pump phase-dithering tones on the idler (see Figure 6.5).

At higher gain, the SBS-induced distortions of the pump, in the diversity loop, becomes more critical resulting in slightly higher PDG values especially at higher pump powers as also discussed in Chapter 5 Section 5.2.1 and Section 5.2.3.

The single-channel optical spectra at the output of the diversity loop with pumps on and off for 5-dB, 10-dB, and 13-dB gain levels have been captured with an optical spectrum analyzer as shown in Figure 6.8(a). The corresponding generated idlers are also shown in the Figure 6.8(a).

During the WDM performance evaluation of the device, all the five channels of the modulated data are launched into the FOPA with a total power of -5 dBm into the diversity loop. This power has been used in order to operate the FOPA in the linear regime [108]. The wavelengths of the WDM channels are selected to be within the flat range of the gain-bandwidth spectra of the FOPA as indicated in Figure 6.7(b). The optical spectra for the WDM channels at the output of the diversity loop for the investigated signal on-off gain levels are shown in Figure 6.8(b). The spectrum is obtained from an optical spectrum analyzer (at a resolution bandwidth of 0.1 nm) after a 20-dB coupler.

The BER performance for the amplified signals and their corresponding generated idlers are measured for the 5-channel WDM as well as for a single-channel scenario. Initially, the single-channel BER performance is evaluated. Figure 6.9(a) and 6.9(b) show the summary of the BER performance as a function of receiver OSNR. It is worth noting that the BER evaluation has been performed for the polarization-scrambled PDM data. It can be seen from the BER graph

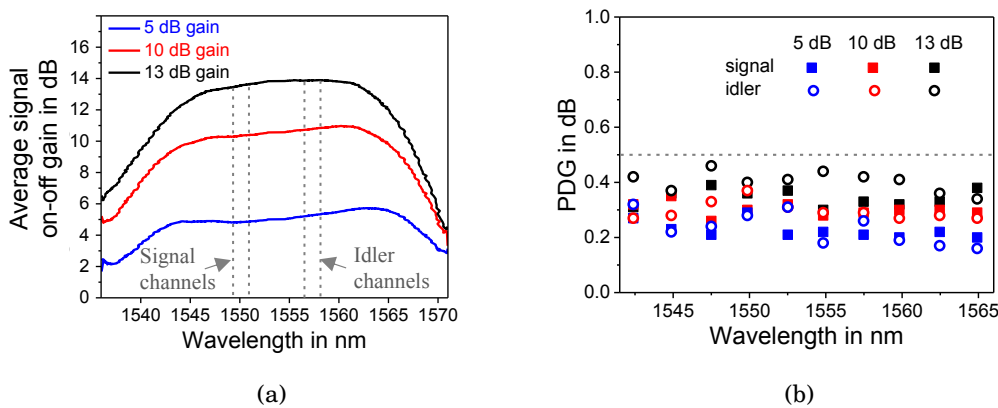
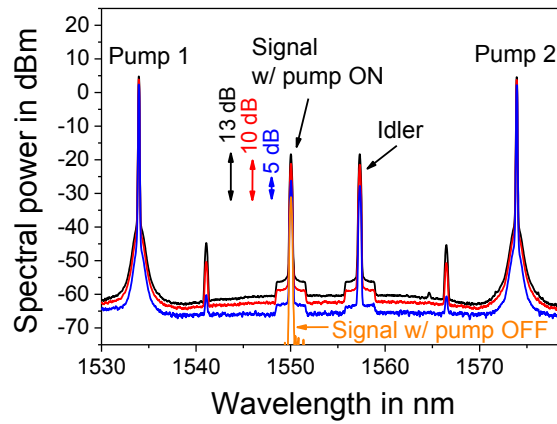
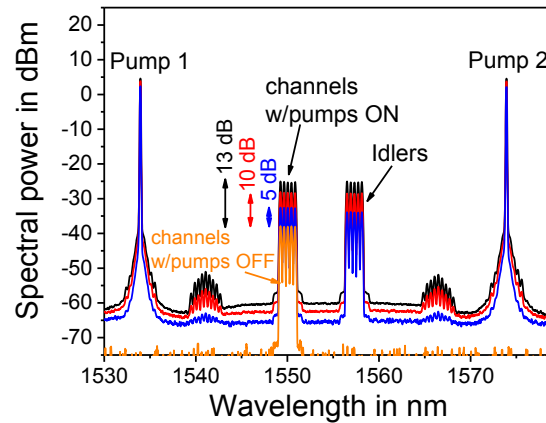


**Figure 6.7:** (a) OPC device gain-bandwidth showing the regions of the signal and idler channels that is used for WDM performance analysis. (b) PDG evaluation of the OPC unit for the amplified signals and their corresponding idlers.



(a)



(b)

**Figure 6.8:** Optical spectra at the HNLf output of the OPC device, after a 20-dB coupler, showing the generated idlers and the signals at different on-off gain for: (a) signal-channel case. (b) 5-channel WDM scenario. OSA resolution bandwidth of 0.1 nm.

that the back-to-back measurement (i.e., b2b w/o FOPA) deviates from the theory. This is due to the non-ideal components used to generate the signal at the transmitter. The OSNR penalties at a BER of  $1 \times 10^{-4}$  for the different signal gain levels are 0.5 dB, 0.9 dB, and 1.6 dB for the 5-dB, 10-dB, and 13-dB gain values, respectively. It is worth to note that in the WDM investigation, the WDM center-channel (signal wavelength at 1550.12) is used for the evaluations. Here, the OSNR implementation penalties at a BER of  $1 \times 10^{-4}$  for the different signal gain levels are found to 0.9 dB, 1.4 dB, and 2.1 dB for the 5-dB, 10-dB, and 13-dB gain values, respectively, as shown in Figure 6.9(b).

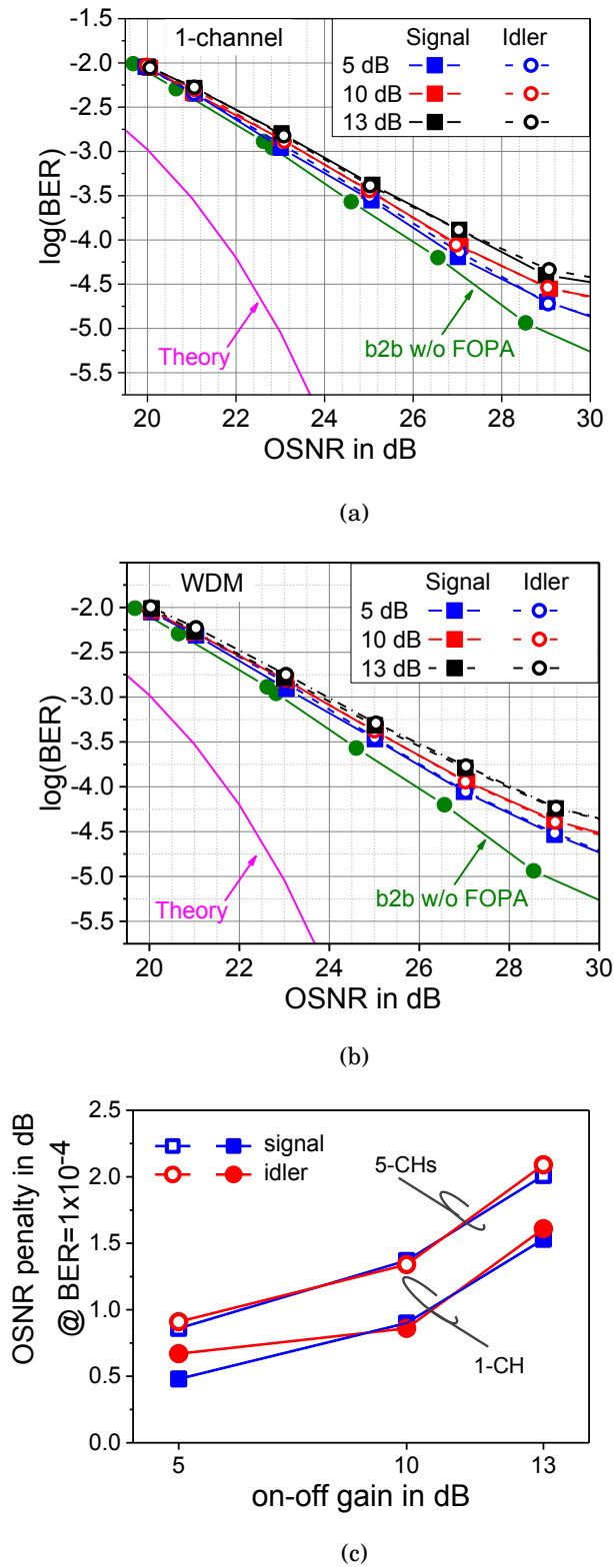


**Figure 6.9:** Receiver BER curves for signal and idler at different gain levels: (a) Single-channel. (b) 5-channel WDM system. (c) OSNR penalties at a BER of  $1 \times 10^{-4}$  for both signal and idler as functions of on-off gain.

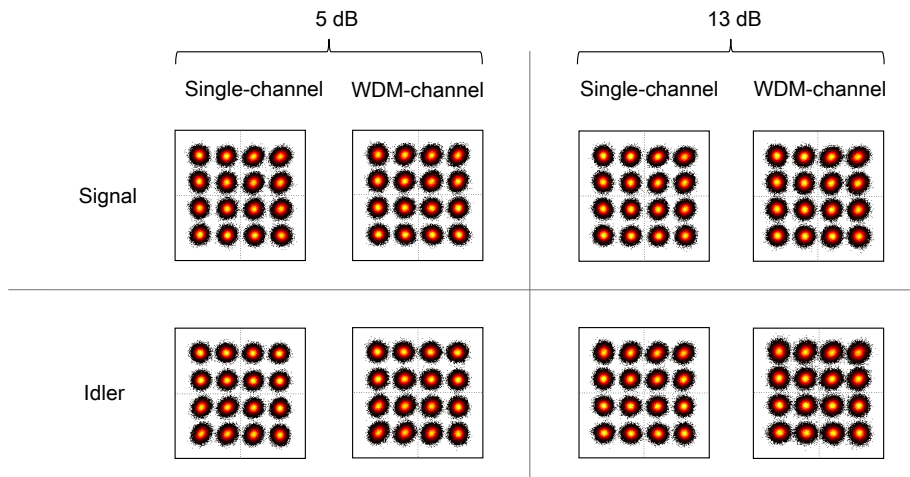


**Figure 6.10:** 29-dB receiver OSNR of  $x$ -polarization of the polarization-scrambled 28-GBd PDM 16-QAM signal and idler constellation diagrams at 5-dB and 13-dB on-off gain for both single-channel and 5-channel WDM scenario.

A summary of the measured OSNR penalties for both single and WDM scenarios at a BER of  $1 \times 10^{-4}$  is depicted in Figure 6.9(c) for the investigated on-off gain values. It is clear that the distortion experienced in the FOPA increased with increasing pump power and is stronger in the case of WDM [108], indicating that a limited signal gain of 5 dB would be more beneficial for a practical implementation of the OPC device since signal and idler show OSNR penalties below 1 dB for both the single-channel and the 5-channel WDM case at 5-dB on-off gain and at a BER of  $1 \times 10^{-4}$ . In all the measurements, the dependence of the OSNR penalty on the parametric gain is attributed to the fact that at high gain levels, the total pump powers are high thus the SBS-induced pump distortion in the diversity loop is relatively high as discussed in Section 5.2.1. Nevertheless, it can be seen from Figure 6.9 that the performances of the signal and idler, in both the single-channel and the WDM scenario, are very similar as also shown in the constellation diagram in Figure 6.10. This indicates the effectiveness of the suppression of the pump phase-modulation transfer to the idler.

### 6.3 Summary

A dual-pump polarization-independent FOPA for OPC has been experimentally demonstrated at 5 dB, 10 dB, and 13 dB signal on-off gain values for 28-GBd PDM 16-QAM signals in a 5-channel WDM system with 50-GHz spacing. Signal

and idler investigations showed OSNR penalties below 1 dB, at a BER of  $1 \times 10^{-4}$ , for both single-channel and the 5-channel WDM cases at 5-dB on-off gain. The maximum PDG was also measured to be below 0.5 dB across a 22.5-nm wavelength range (from 1542.5 nm to 1565 nm) of the gain-bandwidth of the OPC device. It was also noted that the differences in the BER between the WDM channels were insignificant. This makes the OPC well applicable for WDM transmission systems.

The designed FOPA-based polarization-independent OPC is well suited for in-line OPC applications, especially at 5-dB gain (since the total passive losses in the OPC is 5 dB) for gain-transparent operation with minimal penalty from the FOPA. For practical implementation, OPC operation with a stable polarization is required. Thus, the conventional HNLF, which have been used in the OPC design, has to be replaced with a polarization-maintaining highly nonlinear fiber (PM-HNLF) with a high SBS threshold (e.g. about 33 dBm) and a high nonlinear coefficient (e.g. above 20  $/(W \cdot km)$ ).

## Chapter 7

# Kerr Nonlinearity Mitigation Using a FOPA-based OPC Device

The use of fiber-based optical phase conjugation (OPC) to provide Kerr nonlinearity distortion compensation of lower spectrally efficient modulation formats (e.g. BPSK, QPSK) has been widely studied [25, 34, 133]. It has been reported that higher-order modulation formats are more prone to Kerr nonlinearity distortions and are severely degraded in densely packed channels [8]. Moreover, modulation formats with higher symbol rates are easily affected by dispersion-induced distortion, which can interact with nonlinear effects even over short fiber lengths. Therefore, experimental investigation of fiber-based OPC for Kerr nonlinearity compensation of higher-order modulation formats with higher symbol rates, which has not been extensively studied so far, is necessary.

This chapter discusses nonlinear distortion compensation of  $5 \times 28$ -GBd PDM 16-QAM signals in a laboratory prototype transmission system. Prior to the experimental investigations, a brief description of OPC-based transmission link designs are discussed in Section 7.1. The dual-pump polarization-independent FOPA, which has been characterized in Chapter 6, is used as the OPC device to provide the mid-link spectral inversion of  $5 \times 28$ -GBd PDM 16-QAM signals.

Initially, the nonlinearity compensation is performed in up to 800-km of a dispersion - compensated transmission with lumped amplification of EDFAs. A digital back-propagation algorithm based on the split-step Fourier method is also employed for the mitigation of fiber nonlinearities. The  $Q^2$ -factor performance is compared with that of the OPC-based compensation scheme. The performance comparison has been done both in the single-channel and WDM scenario.

Finally, in Section 7.3, the transmission link is changed to a 400-km link

with dispersion - uncompensated fibers. The transmission system utilizes a backward-pumped distributed Raman amplification (DRA) scheme. Fiber non-linearity compensation of  $5 \times 28$ -GBd PDM 16-QAM signals with 50-GHz spacing, using a fiber-based OPC based on the mid-link spectral inversion, is also experimentally investigated. Note that investigation of Brillouin scattering in the fiber spans of the transmission link is not considered in the experiments.

## 7.1 Transmission link design based on mid-link OPC

In order to fully experience the benefits of distortion compensation provided by mid-link OPC, the entire transmission link must be well designed such that the propagating signal's power profile is symmetric around the mid-link OPC. In addition, the dispersion profile of the fiber spans before and after the OPC device must also be symmetric around the OPC unit [14, 133, 134]. These criteria, when fulfilled, together with a low OSNR penalty of the OPC device is expected to yield a high distortion compensation efficiency which can tremendously increase the transmission reach.

### 7.1.1 Mid-link OPC-based transmission links utilizing EDFAs

Figure 7.1 shows a schematic representation of various dispersion maps of transmission links utilizing lumped amplification by EDFAs. In Figure 7.1(a), the transmitted signal power and the accumulated dispersion profiles are plotted as functions of the transmission distance. Here, the link is basically made of dispersion-uncompensated fiber spans (e.g., standard single-mode fiber) with EDFAs. The high power regions are shaded and marked as effective length ( $L_{eff}$ ). The effective length of a fiber has been discussed in Chapter 3 Section 3.3.1. It is clear from Figure 7.1(a) that optical domain nonlinear distortion compensation is not possible since there is no OPC (or any black-box regeneration) device in the link. The accumulated nonlinear distortion of the signal can be significant for longer transmission lengths. An advantage of this kind of link configuration is that, as a result of the walk-off effect, due to dispersion in the fiber spans, XPM among WDM channels is minimized. This is due to the averaging of crosstalk between neighboring channels (especially for multiple spans). Thus nonlinear crosstalk in dispersion-uncompensated links is expected to be less than the nonlinear crosstalk in their dispersion-compensated counterpart links [135].

A mid-link OPC device is inserted in the transmission link as shown in Figure

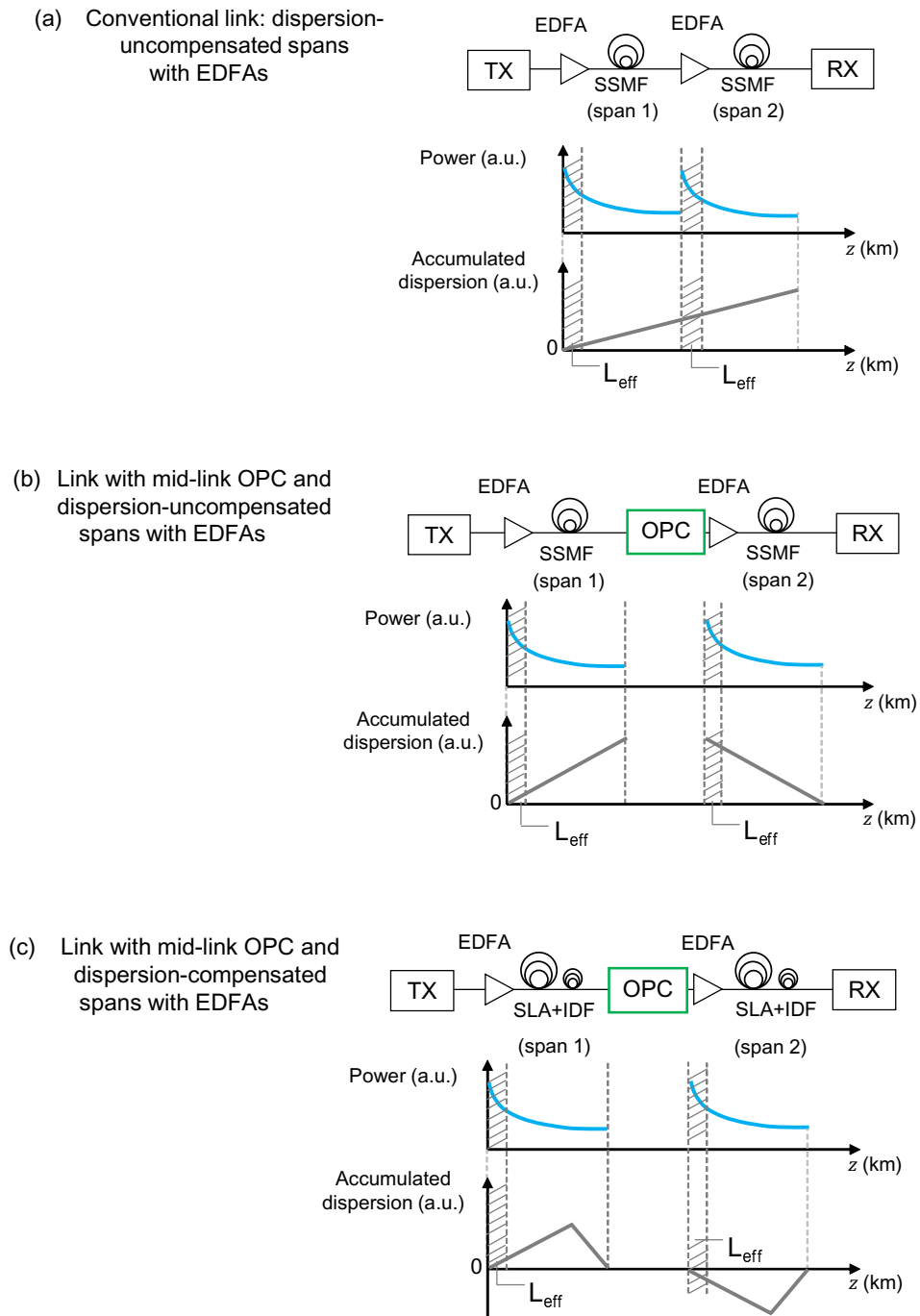


**Figure 7.1:** Transmission link utilizing only EDFAs with: (a) dispersion - uncompensated spans. (b) dispersion - uncompensated spans with mid - link OPC. (c) dispersion - compensated (SLA+IDF) spans with mid-link OPC, (Tx: transmitter, Rx: receiver).

7.1(b). It can be seen that, based on the NLSE in equation (6.2), the dispersion map after the OPC device is reversed. The accumulated dispersion in span 1 and span 2 (i.e., before and after the OPC) are seen to be symmetric around the OPC unit. However, the accumulated dispersion in the high power regions (i.e., shaded areas) are not the same. Hence, a poor nonlinear distortion compensation by the OPC is expected in such a link configuration. And this is due to the unfulfilled simultaneous conditions of the power and dispersion symmetry of the mid-link OPC [14, 133, 134].

Another well-known transmission link configuration is the use of dispersion-compensated fiber spans employing mid-link OPC as depicted in Figure 7.1(c). Here, the dispersion-compensated fiber spans are made from super large area (SLA) fiber and an inverse dispersion-shifted fiber (IDF). The SLA fiber has a positive dispersion slope whereas the IDF has a negative dispersion slope. The OPC device reverses the dispersion profile after span 1. Although dispersion compensated fiber spans are used, it is clear that both the accumulated dispersion and the signal power profiles are not symmetric around the OPC device. Nevertheless, the accumulated dispersion in the high power regions (before and after the OPC), in this case, are seen to be relatively similar. Thus, the efficiency of nonlinear distortion compensation by the OPC is expected to be relatively better, although not optimum due to the asymmetry of the accumulated dispersion in the high power regions, compared to the previously discussed links. In the absence of OPC, the transmission link is expected to degrade WDM signals severely due to lack of walk-off among WDM channels. However, with the implementation of mid-link OPC, substantial nonlinear distortion compensation should be achieved. Note that experimental investigation for nonlinearity compensation using this transmission link type will be discussed later in this Chapter.

### **7.1.2 Mid-link OPC-based transmission links utilizing DRA**

To be able to achieve a symmetric signal power profile in the transmission fiber spans, distributed Raman amplification (DRA) with backward pumping is a suitable amplification technology compared to the other amplification schemes [136]. In addition, the large bandwidth of Raman amplifiers makes them attractive for optical transmission networks [78]. Backward-pumped distributed Raman amplification provides lower signal power excursion which eventually yields a near symmetric power profile than that of EDFAs as also discussed in [16, 136–138]. Figure 7.2 shows several link configurations utilizing backward-pumped dis-

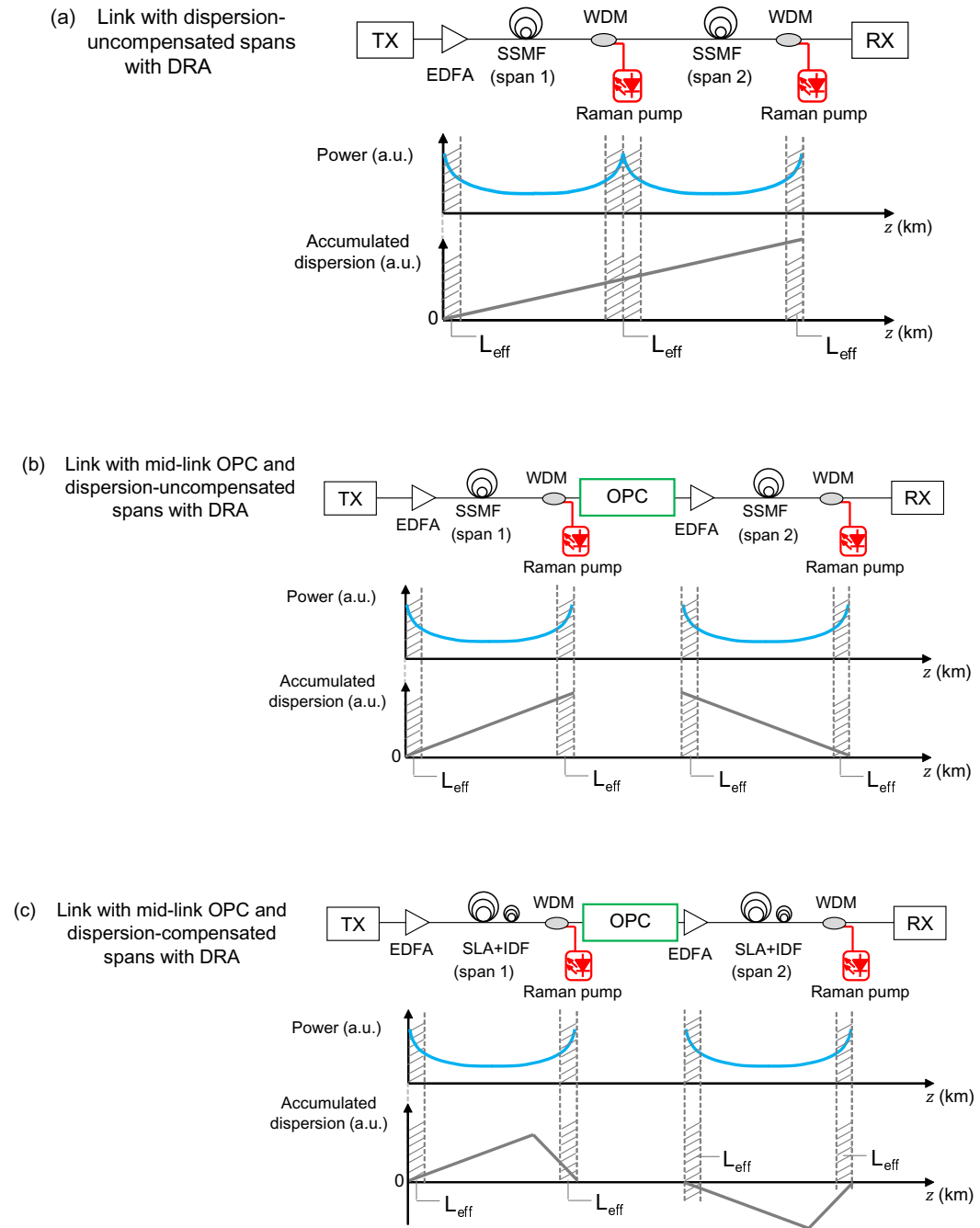


**Figure 7.2:** Transmission link utilizing backward-pumped distributed Raman amplification (DRA) with: (a) dispersion-uncompensated spans. (b) dispersion-uncompensated spans with mid-link OPC. (c) dispersion-compensated spans (SLA+IDF) with mid-link OPC, (Tx: transmitter, Rx: receiver).

tributed Raman amplification.

In Figure 7.2(a), a transmission link made of dispersion-uncompensated (e.g. SSMF) spans with Raman amplification utilizing backward pumping schemes is shown. In this kind of link configuration, an approximately symmetric power profile is achieved (i.e., with the application of the backward-pumped distributed Raman amplification). However, nonlinear distortion compensation is not possible since the accumulated dispersion increases monotonically. A mid-link OPC device is placed in the transmission link, as shown in Figure 7.2(b). It is clear that symmetric dispersion and signal power profiles, around the OPC device, are achieved. Therefore, this kind of link configuration represents a suitable configuration for nonlinear distortion compensation using mid-link OPC. It is worth noting that due to the walk-off in standard fibers, accumulated XPM among neighboring channels is reduced compared to their dispersion-compensated counterpart links.

In practice, the power symmetry expected from the implementation of distributed Raman amplification is difficult to achieve, especially in longer transmission fiber spans [27]. Therefore, a complete nonlinearity compensation will not be achieved even in this configuration. However, in transmission links with shorter fiber spans (e.g. less than 70 km), the performance of the OPC for nonlinearity compensation can be closer to the optimum [26, 27].

Distributed Raman amplification can also be implemented in a transmission link with dispersion-compensated fiber spans. Employing a mid-link OPC in such a link, as shown in Figure 7.2(c), can compensate for a significant amount of nonlinear distortions. The accumulated dispersion in the high power regions are relatively similar, although not ideal. Due to the use of DRA, however, the signal power profile is symmetric around the OPC. Therefore, in Figure 7.2(c), the benefits of the OPC device for nonlinearity compensation is expected to be slightly worse than the link design shown in Figure 7.2(b).

Based on the different transmission link configurations which have been qualitatively considered here, the preferred transmission link design for nonlinearity compensation utilizing mid-link OPC is as shown in Figure 7.2(b). This is due to: (i) the walk-off in dispersion - uncompensated fibers yielding less XPM among neighboring channels, (ii) the power and dispersion symmetry provided by the link design fulfills the performance efficiency of mid-link OPC for nonlinearity compensation. It is worth noting that this kind of link design (i.e., Figure 7.2(b)) is also experimentally investigated in this Chapter.

## 7.2 Mitigation of nonlinear effects in a dispersion - compensated link

### 7.2.1 Experimental setup: Link with mid-link OPC and dispersion-compensated spans with EDFAs.

Figure 7.3 shows the experimental setup which is similar to the link design shown in Figure 7.1(c). It has been discussed in Section 7.1.1 that this kind of link configuration will not provide the maximum nonlinearity compensation provided by the mid-link OPC. And this is due to the asymmetry of both the power and the dispersion profiles of the link. However, there exist in practice legacy transmission links utilizing this type of link configuration. Therefore, experimental investigation of the performance of a mid-link OPC in such a link design is paramount.

In the experimental setup, a  $5 \times 28$ -GBd PDM 16-QAM transmitter and a standard polarization-diverse coherent receiver have been implemented for the experimental investigation. The complete setup and description of both the transmitter and the receiver have been described in Chapter 6 Sections 6.2.1 and 6.2.2, respectively. The generated PDM 16-QAM signals from the transmitter are sent to the coherent receiver over the dispersion-compensated link (i.e., SLA+IDF spans). The transmission link is a dispersion-compensated link which basically consists of fiber spans made from SLA and IDF fibers. Table 7.1 shows the specifications of a representative span of the link. In order to set the propagating signal power in the fiber span (referred to as launch power under test), an EDFA in front of each span is used. The EDFA after the first half of the link ( $N$  spans in link part 1) is set to a constant output power of 17 dBm so as to keep the input signal power into the FOPA constant. The accumulated ASE generated

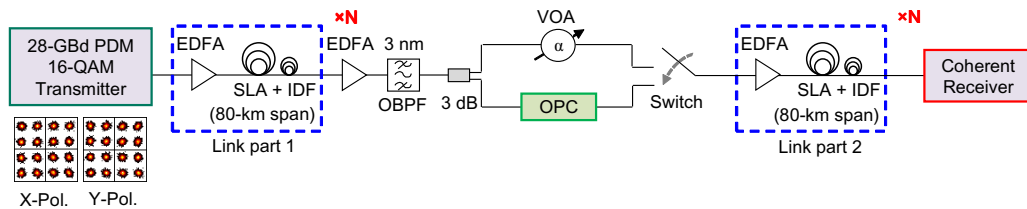


**Figure 7.3:** Experimental setup showing the  $5 \times 28$ -GBd PDM 16-QAM transmitter, the dispersion-managed fiber spans (SLA+IDF), the dual-pump polarization-independent FOPA, which is used as OPC device, and the coherent receiver.

by the link EDFAs is suppressed by using a 3-nm optical bandpass filter and the signal is split into two portions by a 3-dB optical coupler. One portion of the signal goes through the OPC device, whereas the other portion bypasses the OPC device, which is referred to, here, as *straight* transmission. The detailed design and performance evaluation of the used polarization-independent OPC device is already discussed in Chapter 6. In order to keep the OPC penalty low in this experiment, a total pump power of 28.2 dBm and a total signal power of -5 dBm (for either single-channel or WDM case) are launched into the diversity loop via the polarization beam splitter (PBS) as discussed in Section 6.2.4. This provided polarization-independent parametric signal on-off gain of 5-dB and 4-dB idler conversion efficiency at the output of the OPC. A variable optical attenuator (VOA) in the path without OPC ensures that the same input power is injected to the first EDFA of link part 2 in both scenarios, thereby resulting in the same noise accumulation behavior in the second half of the link.

Parameter (properties at 1550 nm)	Symbol	Unit	SLA	IDF
Length	$L$	km	55.57	25.68
Effective area	$A_{eff}$	$\mu\text{m}^2$	107	31
Loss coefficient	$\alpha$	dB/km	0.186	0.234
Dispersion slope	$S$	ps/(nm <sup>2</sup> ·km)	0.06	-0.13
Dispersion	$D$	ps/(nm·km)	20.2	-44
Nonlinear refractive index	$n_2$	$\times 10^{-20}$ m <sup>2</sup> /W	2.23	2.36

**Table 7.1:** Specifications of the dispersion-compensated fiber (each span consists of SLA and IDF fibers).

Due to the low-loss operation of the OPC device, the additional attenuation introduced by the variable optical attenuator in the path without OPC is about 5 dB and it is mainly due to the loss of the optical bandpass filter (5 dB) which has been used to select the idler channel(s) at the output of the OPC. A conventional link without OPC would not consist of the interface between the link part 1 and link part 2 in Figure 7.3. Note that link part 1 and link part 2, respectively, indicate the link before and after the OPC device. However, this interface has a negligible effect on the noise performance of the link since as mentioned before, the first EDFA in the interface is set to a large constant output power and the signal level is high during the optical processing in the interface and reduces only to about 2 dBm measured at the input of the first EDFA in link part 2. Therefore, the interface causes a negligible signal OSNR penalty. An optical switch, before

link part 2, is used to either select the output of the OPC device (the idler) or the signal which bypasses the OPC device (straight transmission) before launching the selected data into the remaining half of the link ( $N$  spans in link part 2). Detection of the signal or the idler after transmission over the entire link is performed with a standard polarization-diverse coherent receiver. It also worth noting that the entire transmission experiments in the thesis have been carried-out in a straight transmission link (i.e., without recirculating loop). Recall that investigation of Brillouin scattering in the fiber spans of the transmission link is not considered in the experiments.

## 7.2.2 Results and discussion

### Single-channel

In the single-channel scenario, the nonlinearity compensation performance by using the OPC in a transmission link with total lengths of 480 km, 640 km, and 800 km (corresponding to  $N = 3, 4,$  and  $5$  spans before the OPC and  $3, 4,$  and  $5$  spans after the OPC) have been individually investigated with a single-channel 28-GBd PDM 16-QAM signal at 1550.12 nm (center-channel in the WDM experiment).

In the link, the signal launch power per span is adjusted from -6 dBm to +4 dBm and after the transmission, the signal quality factor ( $Q^2$ -factor) has been derived for each signal launch power from the measured BER at the receiver using the relation [23, 76, 139]:

$$Q^2(\text{dB}) = 20 \times \log_{10} \left[ \sqrt{2} \operatorname{erfc}^{-1} \left( 2 \times \text{BER} \right) \right] \quad (7.1)$$

Where  $\operatorname{erfc}$  is the complementary error function. It is customary to relate the BER to the signal-to-noise ratio (SNR) since in an ideal linear transmission system, the  $Q^2$ -factor scales linearly with SNR. Hence  $Q^2$ -factor margin corresponds to the SNR margin. For instance, improvement in the  $Q^2$ -factor intuitively suggest an increment in the transmission reach since the SNR will be improved.

The calculated  $Q^2$ -factors, for the various transmission lengths, are plotted as a function of the signal launch power per polarization as shown in Figure 7.4(a). As expected, since the accumulated dispersion compensation is achieved by the used dispersion-compensation fibers, the OPC does not provide any compensation in the linear regime (at lower launch powers) in all the three investigated transmission lengths. However, a significant compensation is achieved in the

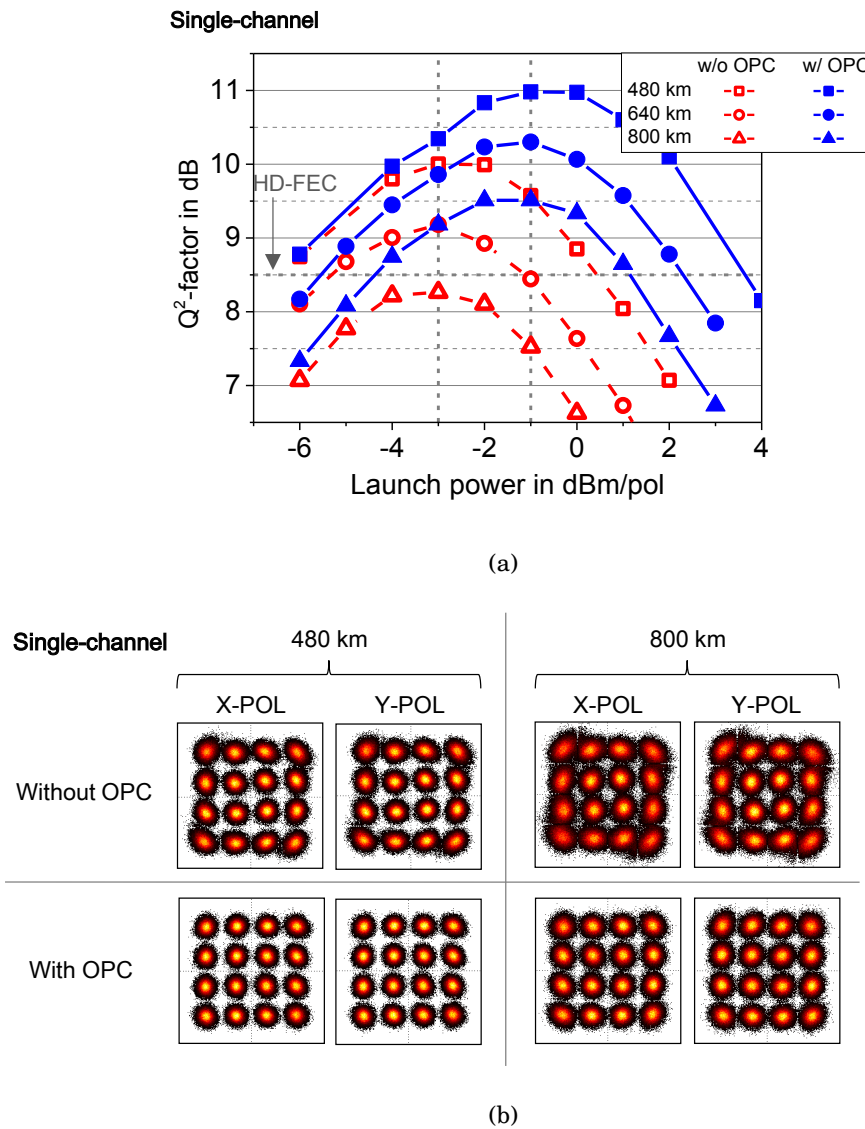


**Figure 7.4:** (a) Single-channel plot of  $Q^2$ -factor versus launch power per polarization over 480 km, 640 km, and 800 km of dispersion-compensated transmission link showing the performances for the cases of straight transmission without nonlinearity mitigation and with OPC operation. (b) single-channel X- and Y-polarization constellation diagrams at 480 km and 800 km at signal launch power of  $P_{\text{launch}} = -1$  dBm/pol.

nonlinear regime (at higher launch powers). It can be seen from Figure 7.4(a) that the maximum  $Q^2$ -factors for the 480 km, 640 km, and 800 km without OPC operation are 10 dB, 9.2 dB, and 8.3 dB, respectively, at a launch power of -3 dBm/pol. The application of OPC increases the maximum  $Q^2$ -factors for the 480

km, 640 km, and 800 km to 11 dB, 10.3 dB, and 9.6 dB, respectively, at a launch power of -1 dBm/pol. Thanks to the OPC implementation at a transmission of 800 km, the maximum  $Q^2$ -factor is found to be well above the hard-decision forward error correction (HD-FEC) threshold of  $BER = 3.8 \times 10^{-3}$  [140] (corresponding to  $Q^2 = 8.5$  dB). The observed maximum  $Q^2$ -factor improvement is 1.3 dB and this is not possible in the case without OPC (maximum  $Q^2$ -factor is below the HD-FEC). Moreover, it is also clear that the nonlinear threshold for each transmission length increased about 2 dB with OPC operation. Note that the nonlinear threshold, in this thesis, is defined as the launch power at the maximum  $Q^2$ -factor [141]. The constellation diagrams for the received single-channel 28-GBd PDM 16-QAM signal at a launch power of -1 dBm/pol for the 480-km and 800-km transmission lengths for the cases with and without OPC operation is as shown in Figure 7.4(b). It is clear that although the power-dependent nonlinear phase-shift causes the outer constellation points to be rotated and also with higher nonlinear noise with respect to the inner constellation points, the nonlinear phase distortion squeezing by OPC operation is visible from the constellation diagrams.

### **WDM scenario**

During the WDM performance evaluation, all five WDM channels are launched into the transmission link. The total WDM signal power and pump power into the OPC are still kept at -5 dBm and 28.5 dBm, respectively, since the FOPA is still operated in a linear regime as discussed in Section 6.2.4. The signal launch power per channel is adjusted from -8 dBm to +1 dBm and the corresponding BERs at the receiver are measured. The  $Q^2$ -factors are calculated from the measured BERs as in the single-channel case. The center-channel at a wavelength of 1550.12 nm has been used for the WDM performance evaluation. It can be seen in Figure 7.5(a) that using signal transmission without OPC for the 480-km, 640-km, and 800-km transmission lengths, the maximum  $Q^2$ -factors are 9.4 dB, 8.5 dB, 7.7 dB, respectively, at a launch power of -4 dBm/ch/pol. With the application of OPC, the maximum  $Q^2$ -factor improves to 10.1 dB, 9.2 dB, and 8.6 dB for the 480-km, 640-km, and 800-km transmission lengths, respectively. Again, the OPC operation provides a maximum  $Q^2$ -factor above the HD-FEC threshold, in the 800 km transmission length, and this is not possible in the case without OPC. Furthermore, the nonlinear threshold for each transmission length increased about 1 dB with OPC operation. More interestingly, it is worth to note

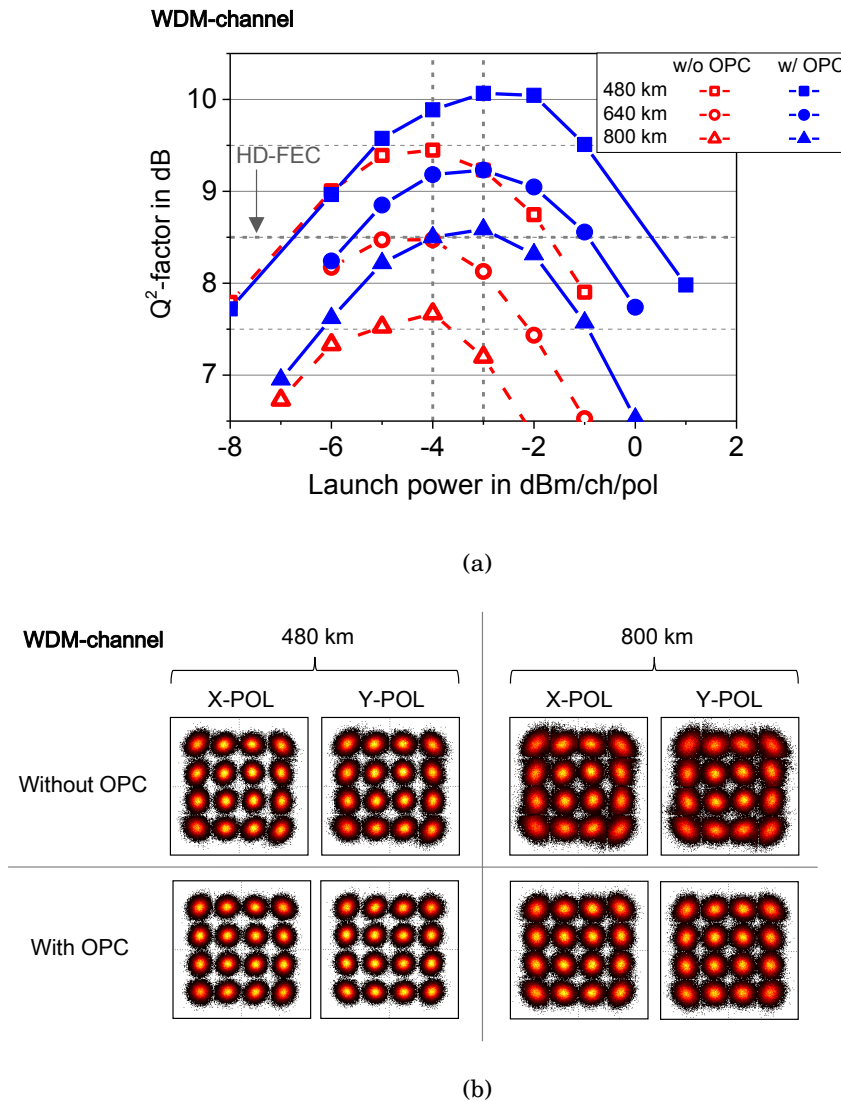


**Figure 7.5:** (a) Five-channel WDM (center-channel): plot of  $Q^2$ -factor versus launch power per channel per polarization over the 480 km, 640 km, and 800 km of dispersion-compensated transmission link showing the performances for the cases of straight transmission without nonlinearity mitigation and with OPC operation. (b) WDM-channel (center-channel): X- and Y-polarization constellation diagrams at 480 km and 800 km at signal launch power of  $P_{\text{launch}} = -3$  dBm/ch/pol.

that the implementation of OPC in the 800-km transmission length enables the same  $Q^2$ -factor performance as in the 640-km transmission length without OPC operation. This indicates an increase of the transmission reach, thanks to the OPC operation, by 25%. The  $5 \times 28$ -GBd PDM 16-QAM constellation diagrams for

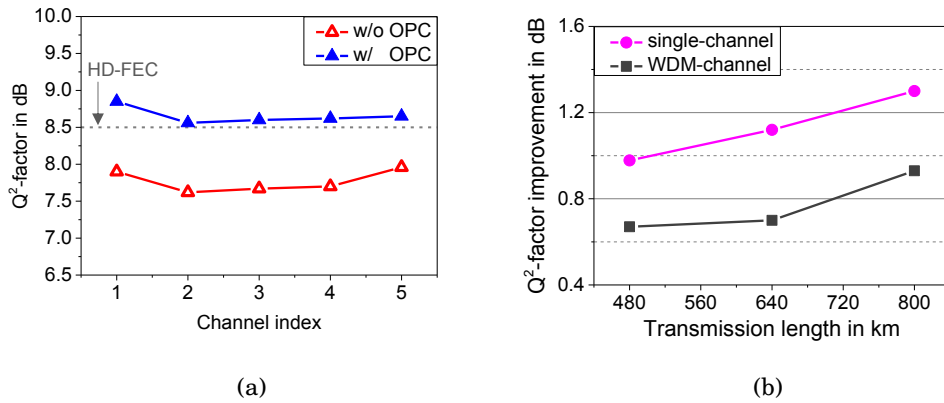


**Figure 7.6:** (a) Plot of  $Q^2$ -factor as a function of channel index for the cases with and without OPC operation over the 800-km transmission length. (b) Summary of single-channel and WDM  $Q^2$ -factor improvements for the 480-km, 640-km, and 800-km transmission lengths.

the cases of signal transmission with and without OPC at a launch power of -3 dBm/ch/pol is shown in Figure 7.5(b). The nonlinear phase distortion squeezing by the OPC can be clearly seen from the constellations.

The  $Q^2$ -factor performances at a launch power per channel of -3 dBm/ch/pol for all the five WDM channels have been also investigated as shown in Figure 7.6(a). It can be seen that the  $Q^2$ -factor performance of the inner channels (ch-2, ch-3, and ch-4) are slightly worse compared to the outer channels. This observation is to be attributed to the high nonlinear contributions from neighboring channels to the inner channels therefore leading to slightly lower performances compared to that of the outer channels. Furthermore, the  $Q^2$ -factors of all the WDM channels are found to be above the hard-decision forward error correction (HD-FEC) with the OPC operation but are not possible without the OPC.

Figure 7.6(b) shows a summary of the  $Q^2$ -factor improvements for the single-channel and WDM scenario over the investigated transmission lengths. It can be seen that the benefits of OPC for nonlinearity compensation is more realized at longer transmission reach (for both single and WDM channels) as also shown numerically in [27]. This is due to the compensation of higher magnitudes of accumulated nonlinear distortions over longer transmission lengths.

The  $Q^2$ -factor improvements in the single-channel case are higher than that in the WDM scenario. This observation may be attributed to the residual dispersion mismatch as a result of the difference in dispersion slope (signal and idler wavelength difference = 7.2 nm) before and after the OPC device. Note that since

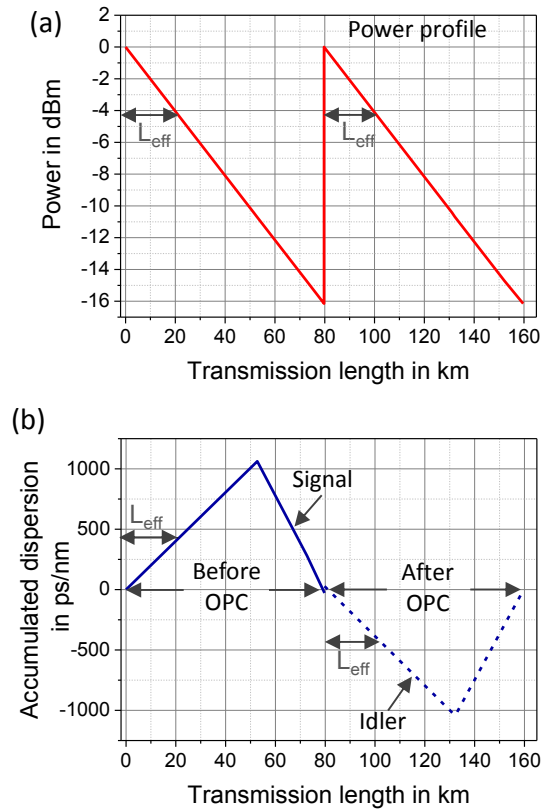


**Figure 7.7:** Power and dispersion map of the transmission link showing: (a) evolution of EDFA amplified signal power at 0 dBm, (b) signal and idler dispersion profiles before and after the OPC device, respectively.

such a difference will cause a sub-optimum inter-channel nonlinearity compensation in the WDM scenario. Furthermore, it is seen from both Figure 7.4(a) and Figure 7.5(a) that the  $Q^2$ -factor performance degrades as the transmission distance increases, even for the case with OPC implementation. This observation can be explained by using the dispersion and power profiles, as shown in Figure 7.7, obtained from the data sheet of the transmission fibers. Specifically, the accumulated dispersions of the signal and idler (signal at 1550.12 nm, idler at 1557.32 nm) at the end of the effective length (i.e., 21 km) are 423.3 ps/nm and -429.7 ps/nm, respectively. It is worth noting that the properties of the used dispersion-compensated fibers are similar, thus profiles of only two spans are shown in Figure 7.7. The absolute difference in the accumulated dispersion is therefore 853 ps/nm at the end of the effective length ( $L_{eff}$ ). Remark that this large dispersion value is due to the use of the inverted  $\beta_2$  for the conjugated sig-

nal in the NLSE as also shown in Figure 7.7(b). The bandwidth of each channel is  $\sim 0.26$  nm, hence the corresponding dispersion mismatch between the signal and the idler will be  $\sim 217$  ps (about 6 symbols). The nonlinearity compensation of the OPC technique is degraded by effects such as fiber-length mismatch before and after OPC, non-symmetrical power distribution versus the fiber length, as observed in [27, 34]. The PMD coefficient of the used dispersion-compensated link is  $0.1 \text{ ps}/\sqrt{\text{km}}$ , therefore the accumulated differential group delay (DGD) after 800 km of transmission is 2.8 ps which is negligible comparing it to the symbol slot of 35.7 ps (symbol rate of 28-GBd). Thus, the main performance limiting factor for the nonlinearity compensation is the wavelength-dependent accumulated dispersion profiles of the signal and the idler which are not perfectly symmetric.

### 7.2.3 Nonlinearity mitigation: mid-link OPC versus digital back-propagation (DBP)

The degree of nonlinearity compensation efficiency of the OPC in the transmission link, investigated in section 7.2, has been quantified by conducting a performance comparison of the OPC and a split-step Fourier method digital back-propagation algorithm. In this comparison, the standard digital back-propagation based on a split-step Fourier method serves as a reference benchmark for the compensation of nonlinear impairments.

Specifically, a non-iterative symmetric split-step Fourier method based on coupled nonlinear Schrödinger (NLSE) equations has been employed for the realization of the back-propagation [11, 31]. The theoretical modeling of back-propagation algorithm has been explained in Appendix A. The dispersion - compensated fibers are modeled using the measured parameters from the fibers used in the experiment and a typical specification of a fiber span is shown in Table 7.1. Note that only the second-order and the third-order dispersion parameters have been taken into consideration. The ASE noise from the link EDFAs and the PMD of the fiber spans have not been considered [31]. The super large area fiber (SLA) and inverse dispersion-shifted (IDF) fibers in each span are modeled separately by performing the split-step Fourier method on each fiber type and each fiber is modeled with a number of  $m$  steps in the split-step Fourier method back-propagation algorithm. It is worth noting that the value of  $m$  has been optimized on a 480-km transmission scenario under WDM operation. Increasing the number of steps per fiber beyond  $m = 10$  did not provide further improvements.

Therefore, the number of steps per fiber is kept fixed at  $m = 10$  and corresponds to ten steps per SLA and ten steps per IDF. A higher number of steps can improve the DBP performance up to a certain level at the expense of higher complexity and computational effort [9, 11]. The split-step Fourier method (SSFM) back-propagation algorithm has been performed on the center-channel of the received  $5 \times 28$ -GBd PDM 16-QAM signal and the results are compared to those obtained from the OPC operation. Remark that two million samples have been processed in both OPC measurements and back-propagation computation. In addition, transmission lengths of 480 km and 800 km are considered for the nonlinearity performance comparison.

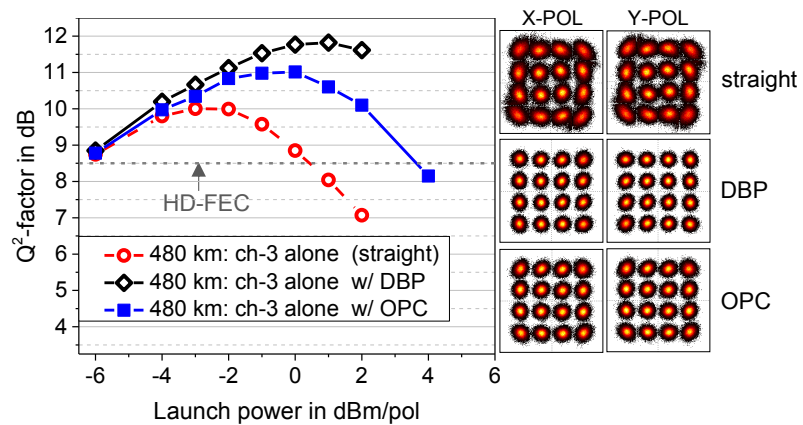
### Single-channel

The received single-channel 28-GBd PDM 16-QAM data of the straight signal transmission over 480 km is back-propagated in the modeled back-propagation algorithm. It is seen from Figure 7.8(a) that the maximum  $Q^2$ -factor for the case with back-propagation increases to 11.8 dB (at a launch power of 1 dBm/pol) comparing to the maximum  $Q^2$ -factor of straight signal transmission. Therefore an improvement in performance of 0.8-dB is achieved compared to the maximum  $Q^2$ -factor for the OPC compensation technique. The 28-GBd PDM 16-QAM constellation diagrams at a launch power of 1 dBm/pol for the cases of: straight transmission without any compensation scheme, with OPC operation, and with back-propagation are also shown in Figure 7.8(a).

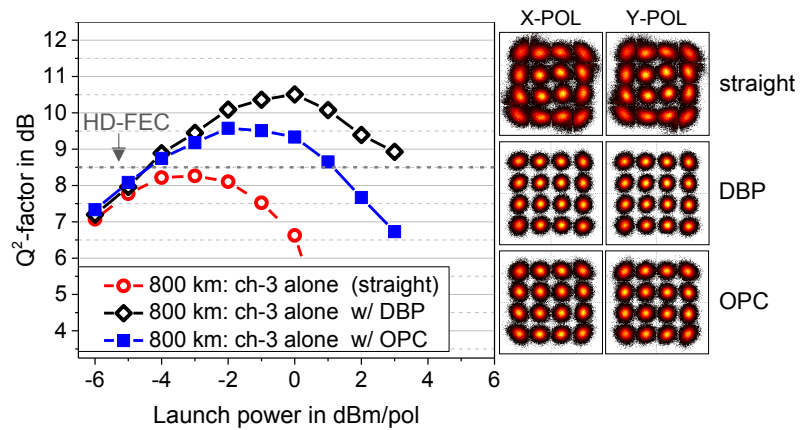
After increasing the transmission length to 800 km, the calculated  $Q^2$ -factors are plotted as a function of the signal launch power per polarization as shown in Figure 7.8(b). It is clear that straight signal transmission without any nonlinearity mitigation scheme is not possible with  $Q^2$ -factors below the hard-decision forward-error correction (HD-FEC) threshold. However, with the implementation of the OPC the maximum  $Q^2$ -factor increased from 8.3 to 9.6 dB resulting in a  $Q^2$ -factor improvement of 1.3 dB. Moreover, application of the back-propagation increases the maximum  $Q^2$ -factor to 10.5 dB. This yields an improvement of the maximum  $Q^2$ -factor improvement of 2.2 dB when compared to the straight signal transmission and is 0.9 dB better than the OPC scheme. The nonlinear threshold is also seen to be increased considerably thanks to the use of the back-propagation algorithm.

It is observed that the OPC compensation scheme shows poorer performance than the back-propagation. This is attributed to the asymmetric power evolu-

tion over the EDFA-based transmission link as shown in Figure 7.7. In addition, locating the OPC exactly in the middle of the link such that the accumulated dispersion is symmetrical around the OPC device can be very difficult, and therefore, any asymmetry regarding the position of the OPC will affect the performance [14, 16]. The back-propagation algorithm, however, does not have such constraints. In addition, the generation of an idler at a different wavelength in the OPC scheme (signal at 1550.12 nm, idler at 1557.32 nm) results in a dispersion mismatch between signal and idler which can lead to inefficient distort-



(a)



(b)

**Figure 7.8:** Single-channel: plot of  $Q^2$ -factor versus launch power per polarization, showing the performances for the cases of straight transmission without nonlinearity mitigation, with OPC operation and with split-step Fourier method digital back-propagation (DBP) (a) over the 480-km transmission link at  $P_{\text{launch}} = 1$  dBm/pol. (b) over the 800-km transmission link at  $P_{\text{launch}} = 0$  dBm/pol.

tion compensation as already discussed in 7.2.2. The 28-GBd PDM 16-QAM constellations diagrams at a launch power of 1 dBm/pol for the cases of: straight transmission without any compensation scheme, with OPC operation, and with back-propagation are also shown in Figure 7.8(b).

### **WDM scenario**

During the WDM performance evaluation, all five WDM channels have been initially launched into a transmission link of 480-km length and the signal launch power per channel per polarization is adjusted from -7 to 0 dBm. The center-channel (at 1550.12 nm) is evaluated in the WDM investigations. The calculated  $Q^2$ -factors are plotted as a function of the signal launch power as shown in Figure 7.9(a).

A maximum  $Q^2$ -factor of 9.4 dB at a launch power of -5 dBm/ch/pol is achieved in the straight signal transmission without nonlinearity compensation. However, with the application of the back-propagation, the maximum  $Q^2$ -factor improves to 9.9 dB and the implementation of the OPC increases the maximum  $Q^2$ -factor to 10.1 dB. This indicates an improvement of the maximum  $Q^2$ -factor of 0.5 dB and 0.7 dB (compared to the straight transmission without any compensation scheme) for the back-propagation and OPC operation, respectively. An improvement in the nonlinear threshold by the OPC is obviously seen in Figure 7.9(a) to be about 1 dB compared to the back-propagation and by 2 dB compared to the straight transmission. The 28-GBd PDM 16-QAM constellations diagrams at a launch power of -3 dBm/ch/pol for the cases of: straight transmission without any compensation scheme, with OPC operation, and with back-propagation are also shown in Figure 7.9(a).

After increasing the transmission length to 800 km, the  $Q^2$ -factor performances for the three cases (straight transmission without any nonlinearity compensation, with OPC, and with back-propagation) are shown in Figure 7.9(b). The maximum  $Q^2$ -factor obtained from straight transmission without the implementation of any nonlinear compensation scheme is 7.7 dB, which is well below the hard-decision forward-error correction (HD-FEC) threshold, as shown in Figure 7.9(b). Implementation of DBP, although, improves the maximum  $Q^2$ -factor to 8.2 dB but it is still below the HD-FEC threshold. However, OPC operation increases the maximum  $Q^2$ -factor to 8.6 dB, which is above the HD-FEC threshold. Therefore, in this experiment, signal transmission over the 800-km length is only possible with OPC operation with a  $Q^2$ -factor improvement of 0.5 dB,

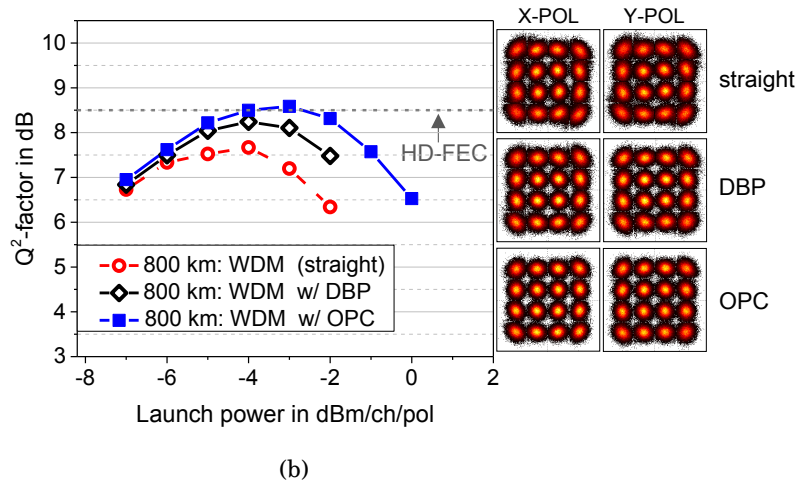
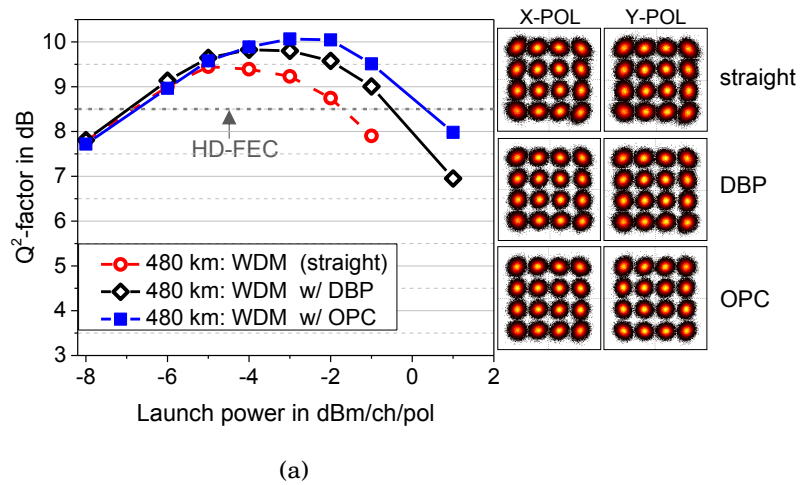


**Figure 7.9:** Five-channel WDM (center-channel): plot of  $Q^2$ -factor versus launch power per polarization, showing the performances for the cases of straight transmission without nonlinearity mitigation, with OPC operation and with split-step Fourier method back-propagation (DBP) (a) over the 480-km transmission link at  $P_{\text{launch}} = -3$  dBm/ch/pol. (b) over the 800-km transmission link at  $P_{\text{launch}} = -3$  dBm/ch/pol.

compared to straight transmission without any nonlinearity mitigation. However, for the same HD-FEC threshold, signal transmission is not possible with the back-propagation algorithm. The constellation diagrams of the 28-GBd PDM 16-QAM data at a launch power of -3 dBm/ch/pol for the cases of: straight transmission without any compensation scheme, with OPC operation, and with back-propagation can also be seen in Figure 7.9(b).

This experiment shows that, in the WDM scenario, the OPC outperforms the

back-propagation algorithm. Ideally, back-propagation can work efficiently for WDM signals if the full-field of the WDM band is back-propagated in the algorithm. Therefore the lower performance of the back-propagation in the WDM scenario is due to the detection bandwidth of the employed coherent reception which is limited to a single WDM channel. In other words, the full-field of the WDM channels cannot be received at the same time due to the limited bandwidth (e.g. the used real-time scope has 20-GHz electrical bandwidth). Hence, the DBP scheme compensated here is for only intra- channel but not for inter-channel distortions [69]. Whereas the OPC compensates for both intra- and inter-channel impairments. The same behavior has been observed for a different dispersion-compensated link configuration in numerical simulations [9]. The performance of the OPC might be further improved in the WDM case over the DBP algorithm if the power profile is made more symmetrical with respect to the middle of the transmission link, a condition which is very critical to attain by using only EDFAs [16].

### **7.3 Mitigation of nonlinear effects in a dispersion - uncompensated link**

As discussed in Section 7.1, both the symmetry of the signal power and fiber dispersion around the OPC is essential for nonlinearity compensation performance enhancement of a mid-link OPC. In order to achieve this, distributed Raman amplification (DRA) with backward pumping has been employed in a dispersion-uncompensated transmission link (similar to Figure 7.2(b)).

#### **7.3.1 Experimental setup: Link with mid-link OPC and dispersion-uncompensated spans with backward-pumped DRA.**

Figure 7.10 shows the experimental setup, consisting of a 28-GBd PDM 16-QAM transmitter, two 100-km standard single-mode fiber spans forming the first half of the link, the FOPA (the OPC device), another two 100-km standard single-mode fiber spans forming the second half of the link, and a digital coherent receiver. It is worth noting that with the exception of the transmission link; the transmitter, the OPC device, and the coherent receiver used in this investigation are the same as those used in Section 7.2 and have been described in detail in Chapter 6. The entire transmission link consists of 400-km standard single-mode fiber, and it is divided into four spans, and four Raman pumps (one for each span) as shown

### Section 7.3. Mitigation of nonlinear effects in a dispersion - uncompensated link

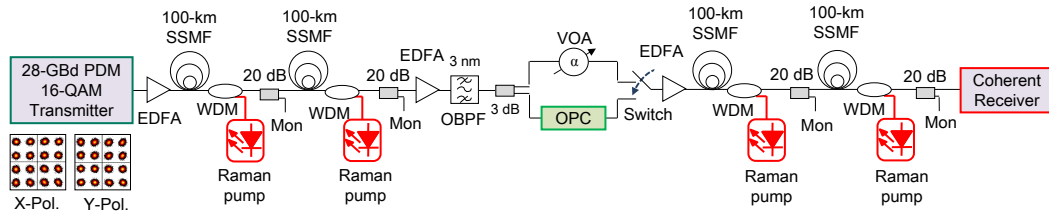


**Figure 7.10:** Experimental setup showing the  $5 \times 28$ -GBd PDM 16-QAM transmitter, the 400-km dispersion-uncompensated link with backward-pumped distributed Raman amplification (DRA), the OPC device, and the coherent receiver.

in Figure 7.10.

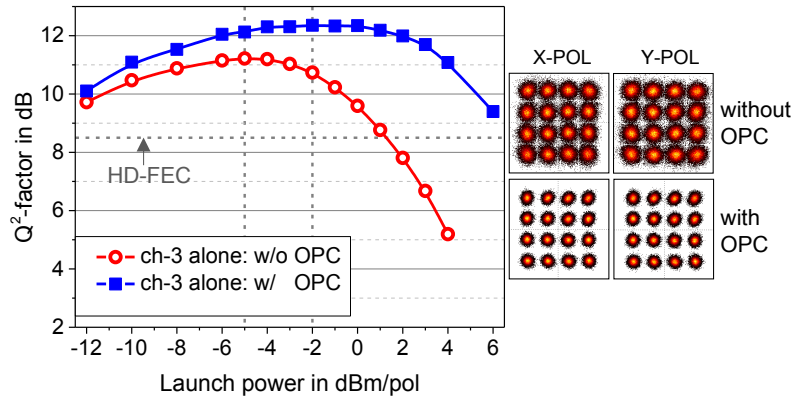
After the transmitter, the signal is launched into an EDFA that enables changing the launch power into the first span. The Raman pumps are implemented in the backward distributed pumping scheme [99, 136]. The wavelengths of the Raman pumps are 1428 nm, 1448 nm, 1450 nm, and 1466 nm. The pumps have been coupled to the end of each span via WDM couplers such that the pump wave propagates in a counter-direction to the signal in the fiber span and this scheme provides a near symmetric power profile per span [99, 136]. The output power of an EDFA, after 200-km of transmission (after two spans), is set to a constant output power of 17 dBm so as to keep the input signal power into the FOPA (the OPC device) constant. Recall that the OPC has an attenuator at the input in order to ensure a linear regime operation (see Section 6.2.3). Note that amplification of the signal power to 17 dBm gives two advantages: (i) high EDFA noise performance and (ii) the required constant -5 dBm signal power at the OPC input is not dependent on the adjustment of the signal launch power. The ASE noise from the link EDFAs is suppressed using a 3-nm optical bandpass filter. A 3-dB coupler is used to split the signal into two parts with one part going through the OPC device whereas the other portion bypasses the OPC device. The used pump and signal powers into the OPC are the same those used in Section 7.2. Similar to the discussion in Section 7.2, a variable optical attenuator is used to ensure that the input powers (for the cases with and without OPC) into the EDFA at the beginning of the second half of the link are the same. To select either the idler (the conjugated signal after the OPC device) or the straight signal which bypasses the OPC device, an optical switch is implemented for the selection before launching the selected data into the remaining 200-km standard single-mode fiber link. The data after the transmission link is detected with a polarization-diverse coherent receiver.

### 7.3.2 Results and discussion

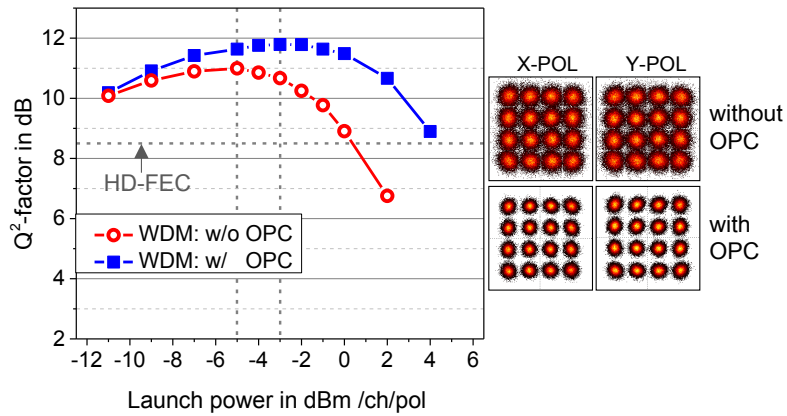
The BER performance for a single-channel scenario has been initially measured. Here, only the center-channel (at 1550.12 nm) from the transmitter is allowed to propagate along the transmission link and either the signal or the corresponding idler is then detected at the receiver. The launch power per polarization of the polarization-scrambled signal into the first span of the link has been adjusted from -12 dBm to +6 dBm by tuning the gain of the EDFA located at the output of the transmitter. In order to obtain, approximately, a symmetric signal power profile, the launch powers at the input and output of the fiber span must be the same. To do this, the power of the Raman pump has been adjusted (whilst monitoring the power at the output of the 20-dB tap coupler after the span) until the launch power into the second span is equal to the launch power under test (considering the low total insertion losses of the WDM coupler and of the 20-dB monitor coupler of about 0.6 dB). Similarly, the launch power at both the input and output of the second span are also set equal by adjusting the output power of the Raman pump after that span. It is worth to note that since the FOPA is operated in the low-gain regime (i.e., idler conversion efficiency is 4 dB) to avoid signal degradation [108,119], an additional EDFA at the input of span 3 (after the mid-link OPC) is required. Therefore, the launch power into the third span is set with the EDFA after the OPC. The previous procedure has been used in setting the launch power per span (following adjustment of the backward-pumped Raman amplifiers) for the remaining half of the link.

The calculated single-channel (ch-3 alone)  $Q^2$ -factor is plotted as a function of the launch power per polarization into the fiber spans. The receiver DSP dispersion compensation is required for signal transmission without OPC in order to recover the constellations to measure the BER. However, DSP-assisted dispersion compensation is not required in the case of OPC operation since OPC operation inherently compensates for chromatic dispersion. It can be seen from Figure 7.11(a) that without the OPC implementation, a maximum  $Q^2$ -factor of 11.2 dB at a launch power of -5 dBm is obtained. However, with the implementation of the OPC, the maximum  $Q^2$ -factor improves to 12.4 dB (indicating about 1.2 dB improvement) at 3-dB increased optimum launch power. In addition, the case with OPC operation is also seen to improve the nonlinear threshold significantly. The experimentally measured 28-GBd PDM 16-QAM constellations diagrams for the cases with and without OPC are also shown in Figure 7.11(a).

Comparing the dispersion-compensated link utilizing only EDFAs (as discussed



(a)



(b)

**Figure 7.11:** (a) Single-channel: plot of  $Q^2$ -factor as a function of launch power per polarization, showing the performances for the cases with and without OPC with the corresponding experimental constellation diagrams at a launch power of 2 dBm/pol. (b) Five-channel WDM (center-channel): plot of  $Q^2$ -factor as a function of launch power per polarization, showing the performances for the cases with and without OPC with the corresponding constellation diagrams at a launch power of 2 dBm/pol.

in Section 7.2) with this Raman-based link, it is clear that the dispersion - uncompensated link utilizing DRAs is better in terms nonlinearity mitigation performance. This observation is consistent with the qualitative description in Section 7.1.2.

In order to investigate the performance evaluation in the WDM scenario, all five channels are then enabled, by the wavelength selective switch (WSS) in the

transmitter, to propagate over the transmission link. Similar signal launch power setting procedure as in the single-channel case has been used to adjust the launch power per channel per polarization into the fiber spans from -11 dBm to +4 dBm. Remark that the center-channel (ch-3) is investigated in the WDM performance analysis. Figure 7.11(b) shows the calculated  $Q^2$ -factor plot versus launch power per channel per polarization. It can be seen that without the OPC operation, a maximum  $Q^2$ -factor of 11 dB at a launch power of -5 dBm is obtained, whereas with the implementation of the OPC, the  $Q^2$ -factor improves to 11.8 dB (0.8 dB improvement) at 2-dB increased optimum launch power. Moreover, OPC operation shows a much higher nonlinear threshold.

In [27], the experimental parameters have been matched to a numerical simulation. The simulation results indicated that, using the HD-FEC, the transmission reach can be extended from the 400 km to 1300 km without OPC and to 2400 km with OPC. This indicates  $\sim 85\%$  increase of the transmission reach at the HD-FEC threshold. The experimental constellation diagrams, after 400 km of transmission, at a launch power of 2 dBm/ch/pol for the cases with and without OPC is also shown in Figure 7.11(b). It is also worth to note that all the five WDM channels show similar performances with a difference between the maximum and minimum  $Q^2$ -factors of only 0.1 dB.

It has also been shown in [27] that the longer the fiber spans, the more asymmetric the signal power evolution with respect to the middle of the span, even if both forward- and backward-pump DRA are employed (i.e., the power symmetry condition is not fulfilled). This power-length asymmetry in longer span designs reduces the full benefits of OPC, especially in long-haul transmission systems as also seen in these experiments. In order to obtain a near symmetric signal power profile over the span, the recommended length of the fiber span, in the presence of DRA, was shown to be about 70 km [27]. Moreover, shorter lengths will result in lower maximum loss per span. This has the tendency to improve the noise performance and therefore it is expected to lead to higher  $Q^2$ -factors. However, shorter spans are not cost attractive since more amplifiers will be required over the entire transmission link.

## 7.4 Summary

This chapter is mainly concerned with the experimental implementation of mid-link optical phase conjugation (OPC) in a transmission link for Kerr nonlinearity

compensation of 28-GBd PDM 16-QAM signals in a 5-channel WDM system with 50-GHz spacing with a net capacity of 1.12 Tb/s.

Initially, the OPC-based nonlinearity compensation was conducted in up 800-km transmission over dispersion-compensated transmission spans for both the single-channel and the WDM scenario. The  $Q^2$ -factor improvement over 480 km was  $\sim 1$  dB in a single-channel case and 0.7 dB in a 5-channel WDM, compared to the case without OPC. The WDM transmission over 800 km indicated a  $Q^2$ -factor improvement of 0.9 dB (compared to the signal transmission without nonlinearity compensation) enabled by the OPC. This allowed 1.12 Tb/s signal transmission above the hard-decision forward-error correction threshold (i.e., BER =  $3.8 \times 10^{-3}$ ), which was not possible without the OPC.

Furthermore, the nonlinearities in the received  $5 \times 28$ -GBd PDM 16-QAM signals were compensated for by employing digital back-propagation nonlinearity compensation scheme based on the split-step Fourier method. The measured results were compared with that of the OPC. The OPC compensation scheme shows an inferior performance compared to back-propagation in the single-channel case. However, in the WDM scenario over the same link length, the OPC-based compensation scheme outperformed back-propagation. This is due to the fact that the back-propagation algorithm can practically compensate for only intra-channel cross-talk. This is due to receiver bandwidth limitations. However, the OPC compensates for both inter- and intra-channel impairments. Thus, in the investigations, the optical domain signal processing proves to be a better approach than its digital domain counterpart for nonlinearity compensation of WDM signals.

Finally, chromatic dispersion and nonlinearity compensation of  $5 \times 28$ -GBd PDM 16-QAM signals with 50-GHz spacing using OPC have been experimentally demonstrated in a 400-km dispersion-uncompensated link. The transmission link consists of standard single-mode fiber (SSMF) spans with distributed Raman amplification with backward pumping scheme. The compensation was conducted for both single-channel and WDM cases. Signal  $Q^2$ -factor improvement of 1.1 dB in a single-channel case and 0.8 dB in a 5-channel WDM compared to the case without OPC have been experimentally measured.

Based on the foregoing investigations, Kerr nonlinearity compensation of 28-GBd PDM 16-QAM signals employing fiber-based polarization-independent OPC which utilizes the polarization-diversity scheme is possible. For practical systems, it is recommended that transmission systems consisting of dispersion-

uncompensated fiber spans employing backward-pumped distributed Raman amplification is the preferred link design. Optimum performance of a mid-link OPC devices, in such a link configuration, for Kerr nonlinearity compensation can be realized.

## Chapter 8

# Summary and Conclusion

In this thesis, the impact of SBS reflections and the origin of polarization dependent gain (PDG) in a single-pump polarization-independent fiber-based optical parametric amplifier (FOPA) employing the polarization-diversity loop scheme are experimentally investigated at high gain conditions.

In addition, the regenerative capabilities of a mid-link optical phase conjugation (OPC), laboratory prototype, has been employed for Kerr nonlinearity compensation of 28-GBd polarization-division multiplexed (PDM) 16-QAM signal. Practical implementation of OPC device does not only require polarization-independent operation, but also a flat gain-bandwidth of the OPC device is desirable for WDM applications. A dual-pump polarization-independent FOPA fulfills these requirements. Therefore, a dual-pump polarization - independent FOPA, employing the polarization-diversity loop scheme, has been used to realize the polarization-independent OPC device. Kerr nonlinearity distortion compensation in modern optical transmission system with a net capacity of 1.12 Tb/s has been experimentally investigated using the dual-pump FOPA-based OPC device.

### 8.1 Summary

#### 8.1.1 SBS-induced pump distortion

A polarization-maintaining highly nonlinear fiber (PM-HNLF) was used as a nonlinear medium for a single-pump polarization-independent FOPA which employed the polarization-diversity loop scheme. The experimental investigation was conducted for up to 20-dB on-off gain with a maximum pump power of 33 dBm. In an unsaturated operation of the FOPA, the presence of Brillouin reflections in the diversity loop was found to distort the pumps traveling in a counter-direction

fashion (i.e., bidirectional) in the diversity loop. Specifically, a 10-GHz shifted Brillouin side-band is created on a pump traveling in one direction by the pump traveling in the opposite direction in the loop. Four-wave mixing (FWM) between the main-band of the pump and the side-band creates new frequency bands on the pump envelope thereby distorting its spectral shape. The degree of pump distortion was found to scale with the pump power (i.e., the higher the pump power, the more severe the pump distortion). This is due to the fact that the side-band (i.e., SBS) power increases with pump power.

Furthermore, it was observed that if the total pump spectral width (due to pump phase-dithering in an attempt to increase the SBS threshold of the used HNLF) is larger than 10 GHz, the pump spectrum in the loop is severely distorted. Specifically, a pump which already contains *seeds* degrade more quickly (i.e., pumps with large spectral width). Note that seeds are spectral components at 10 GHz relative to the main-band of the pump. The seeds experience amplification by the SBS of the counter propagating pump. For the same pump power, pumps with smaller spectral width (i.e., smaller maximum frequency of the pump phase-dithering tones) also degrades the pump due to high levels of SBS in the HNLF. The resulting high amplitude of the side-band interacts with the main-band of the pump by FWM which eventually distorts the pump. The generated 10-GHz side-band creates oscillations (at the Brillouin frequency) on the pump (i.e., amplitude modulation of the pump) which induces a gain modulation of the signal by FWM. Since the parametric gain has an exponential dependence of the pump power, a slight amplitude modulation of the pump has severe impact on the signal gain.

In addition, the pump causes cross-phase modulation (XPM) on the signal. The polarization-independent FOPA was investigated in a back-to-back system test-bed using a 28-GBd single-polarization QPSK signal. It was found that the distortion of the pump (due to SBS) in addition to the XPM by the pump degrades the signal BER.

However, there exist an optimization point where the pump distortion is minimal. The optimization parameters are the total pump spectral width and the generated SBS side-band on the pump. Since the SBS power grows with the pump power, an optimum pump power (at an optimum spectral width) will be required to minimize the pump distortion, however, at the expense of the parametric gain [67]. Therefore, in FOPAs employing the polarization-diversity loop scheme, there exist a trade-off between the pump power (i.e., parametric gain)

and the signal quality [67].

### **8.1.2 Polarization dependent gain (PDG) in diversity loop scheme**

Another parameter which also degrades the signal quality in the diversity loop is the presence of polarization dependent gain (PDG). The dependence of PDG on the pump splitting in the diversity loop was investigated using a continuous wave (CW) signal. The polarization-independent FOPA provided a flat and low PDG of maximal 0.7 dB in a 16-nm wavelength range (1544 nm to 1560 nm) and maximal 1.7 dB in a 22-nm wavelength range of (1538 nm to 1560 nm).

Minimization of the PDG was possible at a fixed signal wavelength by optimizing the pump power splitting at the diversity loop input. However, it did not lead to an overall minimized PDG over the amplification bandwidth. The origin of the PDG in the diversity loop was then investigated and it was found that a 10-GHz shifted spectral component of a propagating pump causes a gradual increase of the pump peak power along the PM-HNLF. The combined effect of SBS of the pump and the presence of asymmetric HNLF's local zero-dispersion wavelength profile, create different local gain spectra in both directions of the diversity loop leading to direction-dependent gain (or non gain-reciprocity) and therefore PDG.

### **8.1.3 Transmission links with mid-link fiber-based OPC**

A dual-pump polarization-independent FOPA employing the polarization-diversity loop scheme was designed, characterized, and implemented as a mid-link OPC device. The FOPA-based OPC device was used for nonlinearity compensation of 28-GBd PDM 16-QAM signal in a 5-channel WDM transmission system with 50 GHz spacing. In order to minimize the SBS in the FOPA, a non-PM-HNLF (i.e., conventional HNLF) with a high nonlinear coefficient and a high SBS threshold was used as a nonlinear medium for the FOPA. During the OPC performance evaluation, both signal and idler investigations showed OSNR penalties below 1 dB, at a BER of  $1 \times 10^{-4}$ , for both the single-channel and the 5-channel WDM cases at 5-dB on-off gain. The maximum PDG was also measured to be below 0.5 dB across a 22.5-nm wavelength range (from 1542.5 nm to 1565 nm) of the gain-bandwidth of the OPC device. It was also noted that the differences in the BER between the WDM channels were insignificant, showing similar performances for all WDM channels. Initially, the mid-link OPC-based nonlinearity compensation was experimentally conducted in up to 800-km transmission over dispersion-compensated transmission spans for both single-channel and the WDM scenario.

In the case of WDM transmission, the OPC operation allowed 1.12 Tb/s signal transmission above the hard-decision forward-error correction (HD-FEC) threshold of  $3.8 \times 10^{-3}$  which was not possible without the OPC. The implementation of OPC in the 800-km transmission length enables the same  $Q^2$ -factor performance as in the 640-km transmission length without OPC operation. This indicates an increase of the transmission reach, as a result of OPC operation, by 25%.

The nonlinearities in the received  $5 \times 28$ -GBd PDM 16-QAM signals were compensated for by employing digital back-propagation scheme based on the split-step Fourier method. The results obtained from the digital back-propagation were compared with that of the OPC. Specifically, the OPC compensation scheme shows an inferior performance compared to the back-propagation in the single-channel case. However, in the WDM scenario over the same link length, the OPC-based compensation scheme outperformed the back-propagation. This is due to the fact that the back-propagation algorithm can practically compensate for only intra-channel cross-talk, due to receiver bandwidth limitations. The OPC, on the other hand, is capable of compensating for both intra-channel and inter-channel nonlinear impairments. However, as a result of effects such as non-perfect symmetry of dispersion and power profiles, polarization mode dispersion (PMD), and residual dispersion slope, the nonlinear compensation by the OPC was not optimum. Nevertheless, the OPC showed slightly better performance than the single-channel back-propagation algorithm which compensates for only intra-channel nonlinear impairments. Thus, the optical domain signal processing proves to be a better approach than its digital domain counterpart for nonlinearity compensation of WDM signals.

Finally, nonlinearity compensation of  $5 \times 28$ -GBd PDM 16-QAM signals with 50-GHz spacing using the mid-link OPC device was experimentally demonstrated in a 400-km dispersion-uncompensated link. The transmission link consisted of standard single-mode fiber (SSMF) spans utilizing distributed Raman amplification with backward-pumped scheme. The compensation was conducted for both single-channel and WDM cases. As a rule of thumb for the nonlinearity performance comparison, the Raman-based link (400 km) improves the signal quality than the EDFA-based link (480 km), even without OPC implementation. This is due to the effective noise figure improvement of the link offered by the use of distributed Raman amplification (DRA) compared to the noise figure provided by the use of discrete amplifiers (e.g. EDFAs) [99, 136].

## 8.2 Conclusion

Pragmatic application of polarization-independent FOPA based on the polarization - diversity loop scheme will require SBS-suppressed HNLFs. This is because the presence of SBS can lead to pump distortions in the diversity loop. This in effect degrades the signal quality. Therefore, the primary concern is to suppress the SBS in the diversity loop. This will require the use of SBS-suppressed HNLFs with high nonlinear coefficients so that lower levels of pump power can yield appreciable signal gain. For instance, aluminum - doped HNLFs with high nonlinear coefficients and with high SBS threshold will provide a reduced pump distortion in the diversity loop. The recently developed stable phase-matching for improved nonlinear efficiency (SPINE) HNLF [142] has lower loss (0.8 dB/km) compared to aluminum-doped HNLF (6-dB/km loss) [97]. However, both the SPINE and the aluminum-doped HNLFs are not polarization - maintaining. A PM-HNLF is required for a practical FOPA implementation. Furthermore, the 26-dBm 1%-SBS threshold of the SPINE HNLF can be improved, if possible, to 33 dBm by manufacturers and this, presumably, will not require further SBS suppression. SBS threshold enhancement of HNLFs using pump phase-dithering technique employing three RF tones with reduced maximum frequency level (e.g. less than 800 MHz) such that the total pump bandwidth is well below 10 GHz (i.e., Brillouin frequency), is a preferred choice for minimum pump degradation. Note that this will yield a limited polarization-independent parametric gain of about 10-15 dB [67].

A secondary issue is to use HNLFs with little (well below 0.1 nm) [143] zero-dispersion wavelength variation. Note that such HNLFs are not easy to manufacture with high precision of the core diameter. As indicated in [47, p. 14], for large pump powers, short fibers can be used so as to avoid large variations of the zero-dispersion wavelength. Based on the the qualitative analysis in this thesis, and the analytical work in [68], a fiber with minimum zero-dispersion wavelength variation will lead to minimum PDG in a FOPA based on the polarization-diversity loop.

The current implementation of OPCs (whether single or cascaded OPCs) in transmission links reduces the spectral efficiency by half. This is because half of the spectral bandwidth before and after the OPC device is not used. Parallel OPCs can be implemented such that the signal spectrum, before the OPC devices, are split into two parts (one part for each OPC). After the OPC devices, the two portions of the idler spectrum can be transmitted without wasting half of the

spectral bandwidth but at the expense of more OPCs. Such a scheme has recently been experimentally demonstrated [58]. Furthermore, a mid-link OPC in a more symmetrical link, through the use of shorter transmission spans (up to 70 km), with distributed Raman amplification with backward pumping [26, 27] and in the presence of third-order dispersion (dispersion slope) compensation [129] will yield better nonlinearity compensation improvements.

It is worth noting that the state-of-the-art of mid-link OPC implementation in optical transmission systems is only applicable in point-to-point transmission links. Implementation of OPC devices in systems with reconfigurable optical add-drop multiplexer (ROADM) is challenging. This is due to the power and the dispersion symmetry requirements of mid-link OPCs. Therefore, future optical transmission systems would require innovative ways to implement mid-link OPCs (for nonlinearity compensation) in ROADMs.

In general, for practical systems, it can be concluded that in transmission systems consisting of shorter spans of dispersion-uncompensated fibers utilizing backward-pumped distributed Raman amplification, the presence of a well optimized mid-link polarization-independent OPC (based on the polarization-diversity loop scheme) can lead to a high Kerr nonlinearity compensation. The FOPA-based OPC device will require SBS-suppressed PM-HNLF with a high nonlinear coefficient. It is recommended that in place of the PM-HNLF, a conventional HNLF can be used in the diversity loop. However, there should be a feedback from the diversity loop (e.g. using a coupler) in order to stabilize the input polarization of the pump.

# Bibliography

- [1] J. Hansryd, P. A. Andrekson, M. Westlund, J. Li, and P. O. Hedekvist, "Fiber-based optical parametric amplifiers and their applications," *IEEE Journal of Selected Topics in Quantum Electronics*, vol. 8, no. 3, pp. 506-520, May/June, 2002.
- [2] P. J. Winzer, "Beyond 100G Ethernet," *IEEE Communications Magazine*, 2010.
- [3] P. J. Winzer, A. H. Gnauck, S. Chandrasekhar, S. Draving, J. Evangelista, and B. Zhu, "Generation and 1,200-km transmission of 448-Gb/s ETDM 56-Gbaud PDM 16-QAM using a single I/Q modulator," in *proc. European Conference on Optical Communication (ECOC)*, 2010, paper PD 2.2.
- [4] R.-J. Essiambre, G. Kramer, P. J. Winzer, G. J. Foschini, and B. Goebel, "Capacity limits of optical fiber networks," *Journal of Lightwave Technology*, vol. 28, no. 4, pp. 662-701, 2010.
- [5] P. J. Winzer, "High-spectral-efficiency optical modulation formats," *Journal of Lightwave Technology*, vol. 30, no. 24, pp. 3824-3835, 2012.
- [6] E. Agrell, M. Karlsson, A. R. Chraplyvy, D. J. Richardson, P. M. Krummrich, P. J. Winzer, M. Secondini, F. R. Kschischang, K. Roberts, J. K. Fischer, S. J. Savory, B. J. Eggleton, A. Lord, I. Tomkos, J. Prat, J. E. Bowers, S. Srinivasan, M. Brandt-Pearce, and N. Gisin, "Roadmap of optical communications," *Journal of Optics*, vol. 18, 2016.
- [7] A. D. Ellis, J. Zhao, and D. Cotter, "Approaching the non linear Shannon limit," *Journal of Lightwave Technology*, vol. 28, no. 4, pp. 423-433, 2010.
- [8] C. Behrens, R. I. Killey, S. J. Savory, M. Chen, and P. Bayvel, "Nonlinear distortion in transmission of higher order modulation formats," *IEEE Photonics Technology Letters*, vol. 22, no. 15, pp. 1111-1113, 2012.

- [9] D. Rafique and A. Ellis, "Nonlinearity compensation in multi-rate 28 Gbaud WDM systems employing optical and digital techniques under diverse link configurations," *Optics Express*, vol. 19, no. 18, pp. 16919-16929, 2011.
- [10] E. Ip, "Nonlinearity compensation using backpropagation for polarization-multiplexed transmission," *Journal of Lightwave Technology*, vol. 28, no. 6, pp. 939-950, 2010.
- [11] A. Napoli, Z. Maalej, V. A. J. M. Sleiffer, M. Kuschnerov, D. Rafique, E. Timmers, B. Spinnler, T. Rahman, L. D. Coelho, and N. Hanik, "Reduced complexity digital back-propagation methods for optical communication systems," *Journal of Lightwave Technology*, vol. 32, no. 7, pp. 1351-1362, 2014.
- [12] M. Morshed, A. J. Lowery, and L. B. Du, "Improving performance of optical phase conjugation by splitting the nonlinear element," *Optics Express*, vol. 21, no. 4, pp. 4567-4577, 2013.
- [13] X. Chen, X. Liu, S. Chandrasekhar, B. Zhu, and R. W. Tkach, "Experimental demonstration of fiber nonlinearity mitigation using digital phase conjugation," in *proc. Optical Fiber Communication Conference (OFC)*, 2012, paper OTh3c.1.
- [14] S. Watanabe and M. Shirasaki, "Exact compensation for both chromatic dispersion and Kerr effect in a transmission fiber using optical phase conjugation," *Journal of Lightwave Technology*, vol. 14, no. 3, pp. 243-248, 1996.
- [15] A. Chowdhury, G. Raybon, R. J. Essiambre, J. Sinsky, A. Adamiecki, J. Leuthold, C. R. Doerr, and S. Chandrasekhar, "Compensation of intra channel nonlinearities in 40 Gb/s pseudo linear systems using optical phase conjugation," in *proc. Optical Fiber Communication Conference (OFC)*, 2004, paper PDP32.
- [16] S. L. Jansen, D. van den Borne, P. M. Krummrich, S. Spälter, G. D. Khoe, and D. de Waardt, "Long-haul DWDM transmission system employing optical phase conjugation," *IEEE Journal of Selected Topics in Quantum Electronics*, vol. 12, no. 4, pp. 505-520, July/August, 2006.

- [17] M. F. C. Stephens, M. Tan, I. D. Phillips, S. Sygletos, P. Harper, and N. J. Doran, "1.14 Tb/s DP-QPSK WDM popolarization-diverse optical phase conjugation," *Optics Express*, vol. 22, no. 10, pp. 11840-11848, 2014.
- [18] L. Du, B. Schmidt, and A. Lowery, "Efficient digital backpropagation for PDM-CO-OFDM optical transmission systems," in *proc. Optical Fiber Communication Conference (OFC)*, 2010, paper OThE2.
- [19] X. Liu, A. R. Chraplyvy, P. J. Winzer, R. W. Tkach, and S. Chandrasekhar, "Phase-conjugated twin waves for communication beyond the Kerr non-linearity limit," *Nature Photonics*, vol. 7, pp. 560-568, May 2013.
- [20] F. P. Guiomar, S. B. Amado, N. J. Muga, J. D. Reis, A. L. Teixeira, and A. N. Pinto, "Simplified Volterra series nonlinear equalizer by intra channel cross phase modulation oriented pruning," in *proc. European Conference on Optical Communication (ECOC)*, 2013, paper We.3.C.6.
- [21] M. Shtaif, R. Dar, A. Mecozzi, and M. Feder, "Nonlinear interference noise in WDM systems and approaches for its cancelation," in *proc. European Conference on Optical Communication (ECOC)*, 2014, paper We.1.3.1.
- [22] W. Pieper, C. Kurtzke, R. Schnabel, D. Breuer, R. Ludwig, K. Petermann, and H. G. Weber, "Nonlinearity-insensitive standard-fibre transmission based on optical-phase conjugation in a semiconductor-laser amplifier," *Electronics letters*, vol. 30, no. 9, pp. 724-726, 1994.
- [23] S. L. I. Olsson, B. Corcoran, C. Lundström, T. A. Eriksson, M. Karlsson, and P. A. Andrekson, "Phase sensitive amplified transmission links for improved sensitivity and nonlinearity tolerance," *Journal of Lightwave Technology*, vol. 33, no. 3, pp. 710-721, 2015.
- [24] F. D. Ros, I. Sackey, R. Elschner, T. Richter, C. Meuer, M. Nölle, M. Jazayerifar, K. Petermann, C. Peucheret, and C. Schubert, "Kerr nonlinearity compensation in a  $5 \times 28$ -GBd PDM 16-QAM WDM system using fiber-based optical phase conjugation," in *proc. European Conference on Optical Communication (ECOC)*, 2014, paper P.5.3.
- [25] H. Hu, R. M. Jopson, A. H. Gnauck, M. Dinu, S. Chandrasekhar, X. Liu, C. Xie, M. Montoliu, S. Randel, and C. J. McKinstrie, "Fiber nonlinearity compensation of an 8-channel WDM PDM-QPSK signal using multi-

- 
- ple phase conjugations,” in *proc. Optical Fiber Communication Conference (OFC)*, 2014, paper M3C.2.
- [26] K. Solis-Trapala, M. Pelusi, H. N. Tan, T. Inoue, and S. Namiki, “Transmission optimized impairment mitigation by 12 stage phase conjugation of WDM  $24\times 48$  Gb/s DP-QPSK signals,” in *proc. Optical Fiber Communication Conference (OFC)*, 2015, paper Th3C.2.
- [27] I. Sackey, F. D. Ros, Jazayerifar, T. Richter, C. Meuer, M. Nölle, L. Molle, C. Peucheret, K. Petermann, and C. Schubert, “Kerr nonlinearity mitigation in  $5\times 28$ -GBd PDM 16-QAM signal transmission over a dispersion-uncompensated link with backward-pumped distributed Raman amplification,” *Optics Express*, vol. 22, no. 22, pp. 27381-27391, 2014.
- [28] X. Liu, S. Chandrasekhar, P. J. Winzer, R. W. Tkach, and A. R. Chraplyvy, “Fiber-nonlinearity-tolerant superchannel transmission via nonlinear noise squeezing and generalized phase-conjugated twin waves,” *IEEE Journal of Lightwave Technology*, vol. 32, no. 4, pp. 766-775, 2005.
- [29] Y. Tian, Y. K. Huang, S. Zhang, P. R. Prucnal, and T. Wang, “Demonstration of digital phase-sensitive boosting to extend signal reach for long-haul WDM systems using optical phase-conjugated copy,” *Optics Express*, vol. 21, no. 4, pp. 5099-5106, 2013.
- [30] R. Tang, J. Lasri, P. S. Devgan, V. Grigoryan, P. Kumar, and M. Vasilyev, “Gain characteristics of a frequency nondegenerate phase-sensitive fiber optic parametric amplifier with phase self-stabilized input,” *Optics Express*, vol. 13, no. 26, pp. 10483-10493, 2005.
- [31] E. Ip and J. M. Kahn, “Compensation of dispersion and nonlinear impairments using digital backpropagation,” *Journal of Lightwave Technology*, vol. 26, no. 20, pp. 3416-3425, 2008.
- [32] L. B. Du and A. J. Lowery, “Improved single channel backpropagation for intra-channel fiber nonlinearity compensation in long-haul optical communication systems,” *Optics Express*, vol. 18, no. 16, pp. 17075-17088, 2010.
- [33] A. Chowdhury, G. Raybon, R.-J. Essiambre, , and C. Doerr, “Optical phase conjugation in a WDM CSRZ pseudo-linear 40 Gb/s system for 4,800 km
-

- transmission,” in *proc. European Conference on Optical Communication (ECOC)*, 2004, paper PD Th4.5.6.
- [34] I. D. Philips, M. Tan, M. F. C. Stephens, M. E. McCarthy, E. Giacomidis, S. Sygletos, P. Rosa, S. Fabbri, S. Randel, S. T. Le, T. Kanesan, S. K. Turitsyn, N. J. Doran, P. Harper, and A. D. Ellis, “Exceeding the nonlinear-Shannon limit using Raman laser based amplification and optical phase conjugation,” in *proc. Optical Fiber Communication Conference (OFC)*, 2014, paper M3C.1.
- [35] A. Yariv, D. Fekete, and D. Pepper, “Compensation for channel dispersion by nonlinear optical phase conjugation,” *Optics Letters*, vol. 4, no. 2, pp. 52-54, 1979.
- [36] D. M. Pepper and A. Yariv, “Compensation for phase distortions in nonlinear media by phase conjugation,” *Optics Letters*, vol. 5, no. 2, pp. 59-60, 1980.
- [37] S. Watanabe, T. Naito, and T. Chikama, “Compensation of chromatic dispersion in a single-mode fiber by optical phase conjugation,” *Optics Letters*, vol. 5, no. 1, pp. 92-95, 1993.
- [38] M. Tatham, G. Sherlock, and L. Westbrook, “Compensation fibre chromatic dispersion by optical phase conjugation in a semiconductor laser amplifier,” *Electronics letters*, vol. 29, no. 21, pp. 1851-1852, 1993.
- [39] S. Y. Set, R. Girardi, E. Riccardi, B. E. Olsson, M. Puleo, M. Ibsen, R. I. Laming, P. A. Andrekson, F. Cisternino, and H. Geiger, “40 Gbit/s field transmission over standard fiber using mid-span spectral inversion for dispersion compensation,” *Electronics letters*, vol. 35, pp. 581-582, 1999.
- [40] A. Chowdhury, G. Raybon, R. J. Essiambre, J. H. Sinsky, A. Adamiecki, J. Leuthold, C. R. Doerr, and S. Chandrasekhar, “Compensation of intrachannel nonlinearities in 40-Gb/s pseudolinear system using optical-phase conjugation,” *Journal of Lightwave Technology*, vol. 23, no. 1, pp. 172-177, 2005.
- [41] I. Brener, B. Mikkelsen, G. Raybon, R. Harel, K. Parameswaran, J. Kurz, and M. Fejer, “160 Gbit/s wavelength shifting and phase conjugation using periodically poled LiNbO<sub>3</sub> waveguide parametric converter,” *Optics Letters*, vol. 36, no. 21, pp. 1788-1790, 2000.

- [42] H. Hu, R. Nouroozi, R. Ludwig, C. Schmidt-Langhorst, H. Suche, and C. Schubert, "110 km transmission of 160 Gbit/s RZ-DQPSK signals by mid-span polarization-insensitive optical phase conjugation in a Ti:PPLN waveguide," *Optics Letters*, vol. 35, no. 17, pp. 2867-2869, 2010.
- [43] S. Ayotte, H. Rong, S. Xu, O. Cohen, and M. J. Paniccia, "Multi-channel dispersion compensation by optical phase conjugation in silicon waveguide," in *proc. European Conference on Optical Communication (ECOC)*, 2007.
- [44] D. Vukovic, J. Schröder, F. D. Ros, L. B. Du, C. J. Chae, D. Y. Choi, M. D. Pelusi, and C. Peucheret, "Multichannel nonlinear distortion compensation using optical phase conjugation in a silicon nanowire," *Optics Express*, vol. 23, no. 3, pp. 3640-3646, 2015.
- [45] I. Sackey, F. D. Ros, T. Richter, M. Jazayerifar, C. Meuer, C. Peucheret, K. Petermann, and C. Schubert, "Design and performance evaluation of an OPC device using a dual-pump polarization-independent FOPA," in *proc. European Conference on Optical Communication (ECOC)*, 2014, paper Tu.1.4.4.
- [46] H. Hu, R. M. Jopson, A. H. Gnauck, M. Dinu, S. Chandrasekhar, X. Liu, C. Xie, M. Montoliu, S. Randel, and C. J. McKinstrie, "Parametric amplification and wavelength conversion of a 2.048-Tb/s WDM PDM 16-QAM signal," in *proc. European Conference on Optical Communication (ECOC)*, 2014, paper We.2.5.2.
- [47] M. E. Marhic, *Fiber optical parametric amplifiers, oscillators and related devices*. 1st edition, Cambridge University press, New York, USA, 2008.
- [48] Thorlabs, "C-band optical amplifiers (SOAs), 1550 nm." Online service, 2015, [https://www.thorlabs.de/newgrouppage9.cfm?objectgroup\\_id=3901](https://www.thorlabs.de/newgrouppage9.cfm?objectgroup_id=3901).
- [49] I. Brener, M. H. Chou, G. Lenz, R. Scotti, E. E. Chaban, J. Shmulovich, D. L. Philen, S. Kosinski, K. R. Parameswaran, and M. M. Fejer, "High efficiency (-7 dB), wideband (70 nm) and tunable LiNbO<sub>3</sub> waveguide mid-span spectral inverter and its use for dispersion compensation in 4×10Gbit/s," in *proc. European Conference on Optical Communication (ECOC)*, vol. II, pp. 16-17, 1999.

- [50] A. Gajda, L. Zimmermann, M. Jazayerifar, G. Winzer, H. Tian, R. Elschner, T. Richter, C. Schubert, B. Tillack, and K. Petermann, "Highly efficient CW parametric conversion at 1550 nm in SOI waveguides by reverse biased p-i-n junction," *Optics Express*, vol. 20, no. 12, pp. 13100-13107, June, 2012.
- [51] F. D. Ros, D. Vukovic, A. Gajda, K. Dalgaard, L. Zimmermann, B. Tillack, M. Galili, K. Petermann, and C. Peucheret, "Phase regeneration of DPSK signals in a silicon waveguide with reverse-biased p-i-n junction," *Optics Express*, vol. 22, no. 5, pp. 5029-5136, 2014.
- [52] K. K. Y. Wong, K. Shimizu, K. Uesaka, G. Kalogerakis, M. E. Marhic, and L. G. Kazovsky, "Continuous wave fiber optical parametric amplifier with 60 dB gain using a novel two-segment design," *IEEE Photonics Technology Letters*, vol. 15, pp. 1707-1709, 2003.
- [53] T. Torounidis, P. A. Andrekson, and B. E. Olsson, "Fiber-optical parametric amplifier With 70-dB Gain," *IEEE Photonics Technology Letters*, vol. 18, no. 10, pp. 1194-1196, 2006.
- [54] M. E. Marhic, K. K. Y. Wong, and L. G. Kazovsky, "Wide-band tuning of the gain spectra of one-pump fiber optical parametric amplifiers," *IEEE Journal of Selected Topics in Quantum Electronics*, vol. 10, no. 5, pp. 1133-1141, Sept./Oct., 2004.
- [55] M. Jamshidifar, A. Vedadi, and M. E. Marhic, "Continuous-wave one-pump fiber optical parametric amplifier with 270 nm gain bandwidth," in *proc. European Conference on Optical Communication (ECOC)*, 2009, paper 1.1.4.
- [56] Z. Tong, C. Lundström, P. A. Andrekson, C. J. McKinstrie, M. Karlsson, D. J. Blessing, E. Tipsuwannakul, B. J. Puttnam, H. Toda, and L. Grüner-Nielsen, "Towards ultrasensitive optical links enabled by low-noise phase-sensitive amplifiers," *Nature Photonics*, vol. 5, pp. 430-436, 2011.
- [57] T. Richter, R. Elschner, A. Gandhe, K. Petermann, and C. Schubert, "Parametric amplification and wavelength conversion of single- and dual-polarization DQPSK signals," *IEEE Journal of Selected Topics in Quantum Electronics*, vol. 18, no. 2, pp. 988-995, March/April, 2012.

- [58] A. D. Ellis, I. D. Philips, M. Tan, M. F. C. Stephens, M. E. McCarthy, M. A. Z. A. Kahteb, M. A. Iqbal, A. Perentos, S. Fabbi, V. Gordienko, D. Lavery, G. Liga, G. Saavedra, M. R. Maher, S. Sygletos, P. Harper, N. J. Doran, P. Bayvel, and S. K. Turitsyn, "Enhanced superchannel transmission using phase conjugation," in *proc. European Conference on Optical Communication (ECOC)*, 2015, paper We.2.6.4.
- [59] G. P. Agrawal, *Nonlinear fiber optics*. 4th edition, Elsevier Science and Technology, San Diego, USA, 2006.
- [60] R. Jopson and R. Tench, "Polarisation-independent phase conjugation of lightwave signals," *Electronics letters*, vol. 29, no. 25, pp. 2216-2217, 1993.
- [61] K. Inoue, "Polarization independent wavelength conversion using fiber four-wave mixing with two orthogonal pump lights of different frequencies," *Journal of Lightwave Technology*, vol. 12, no. 11, pp. 1916-1920, 1994.
- [62] T. Hasegawa, K. Inoue, and K. Oda, "Polarization independent frequency conversion by fiber four-wave mixing with a polarization diversity technique," *IEEE Photonics Technology Letters*, vol. 5, no. 8, 1993.
- [63] K. K. Y. Wong, M. E. Marhic, K. Uesaka, and L. G. Kazovsky, "Polarization-independent one-pump fiber-optical parametric amplifier," *IEEE Photonics Technology Letters*, vol. 14, no. 11, pp. 1506-1508, 2002.
- [64] S. Radic, C. J. McKinstrie, and R. Jopson, "Polarization dependent parametric gain in amplifiers with orthogonally multiplexed optical pumps," in *proc. Optical Fiber Communication Conference (OFC)*, 2003, paper ThK3.
- [65] T. Tanemura and K. Kikuchi, "Polarization-independent wavelength conversion with a gain using two-pump fiber parametric amplification with idler broadening," in *proc. Conference on Lasers and Electro-Optics (CLEO)*, 2003, paper CWA64.
- [66] Q. Lin, F. Yaman, and G. P. Agrawal, "Raman-induced polarisation-dependent gain in parametric amplifiers pumped with orthogonally polarized lasers," *IEEE Photonics Technology Letters*, vol. 18, no. 2, pp. 397-399, 2006.

- [67] M. Jazayerifar, I. Sackey, R. Elschner, S. Warm, C. Meuer, C. Schubert, and K. Petermann, "Impact of SBS on polarization-insensitive single-pump optical parametric amplifiers based on a diversity loop scheme," in *proc. European Conference on Optical Communication (ECOC)*, 2014, paper Tu.4.6.4.
- [68] I. Sackey, M. Jazayerifar, R. Elschner, T. Richter, C. Meuer, K. Petermann, and C. Schubert, "Non-reciprocal gain due to counter-propagating pumps in a polarization-independent FOPA with diversity loop," in *proc. European Conference on Optical Communication (ECOC)*, 2015, paper We.2.4.6.
- [69] S. J. Savory, G. Gavioli, E. Torrenco, and P. Poggiolini, "Impact of inter-channel nonlinearities on a split-step intrachannel nonlinear equalizer," *IEEE Photonics Technology Letters*, vol. 20, no. 10, pp. 673-675, 2010.
- [70] J. M. Kahn and E. Ip, "Principles of digital coherent receivers for optical communications," in *proc. Optical Fiber Communication Conference (OFC)*, 2009, paper OTuG5.
- [71] M. Seimetz, *Higher-order modulation for optical fiber transmission*. Heidelberg: Springer-Verlag, Berlin, Germany, 2009.
- [72] I. P. Kaminov, T. Li, and A. E. Willner, *Optical fiber telecommunications V B: systems and networks*. Elsevier Inc. academic press, San Diego, USA, 2008.
- [73] D. Derickson, *Fiber optic test and measurement*. Prentice-Hall, Inc., Upper Saddle River, New Jersey, USA, 1998.
- [74] E. Ip, A. P. T. Lau, D. J. F. Barros, and J. M. Kahn, "Coherent detection in optical fiber systems," *Optics Express*, vol. 16, no. 2, pp. 753 -794, Jan., 2008.
- [75] S. J. Savory, "Digital coherent optical receivers: algorithms and subsystems," *IEEE Journal of Selected Topics in Quantum Electronics*, vol. 16, no. 5, pp. 1164-1179, Sept./Oct., 2010.
- [76] K. Roberts, S. H. Foo, M. Moyer, M. Hubbard, A. Sinclair, J. Gaudette, and C. Laperle, "High capacity transport-100G and beyond," *Journal of Lightwave Technology*, vol. 33, no. 3, pp. 563-578, 2015.

- [77] P. Poggiolini, G. Bosco, A. Carena, V. Curri, Y. Jiang, and F. Forghieri, "The GN-model of fiber non-linear propagation and its applications," *Journal of Lightwave Technology*, vol. 32, no. 4, pp. 694-721, 2014.
- [78] G. P. Agrawal, *Fiber-optic communication systems*. 4th edition, John Wiley and Sons, Inc., New Jersey, USA, 2010.
- [79] K. Petermann, *Einführung in die optische Nachrichtentechnik*. Vorlesungsskript, TU Berlin, 2003.
- [80] G. Keiser, *Optical fiber communication*. 2nd edition, McGraw-Hill Book Co., Singapore, 1991.
- [81] K. Nagayama, M. Kakui, M. Matsui, T. Saitoh, and Y. Chigusa, "Ultra-low-loss (0.1484 dB/km) pure silica core fibre and extension of transmission distance," *Electronics letters*, vol. 38, no. 20, pp. 1168-1169, 2002.
- [82] G. P. Agrawal, *Nonlinear fiber optics*. 3rd edition, Academic Press, San Diego, CA, 2001.
- [83] S. L. Jansen, S. Spälter, G. D. Khoe, H. deWaardt, D. Zhou, Q. Shu, and L. Marshall, "The impact of asymmetric placement of a spectral inverter in a 40Gbit/s system," in *proc. European Conference on Optical Communication (ECOC)*, 2004, paper Th2.5.6.
- [84] A. Galtarossa and C. R. Menyuk, *Polarization mode dispersion*. Springer science and business media, New York, 2005.
- [85] P. Bayvel and P. M. Radmore, "Solutions of the SBS equations in single-mode optical fibers and implications for fiber transmission systems," *Electronics letters*, vol. 26, no. 7, pp. 434-436, 1990.
- [86] R. Billington, "Measurement methods for stimulated Raman and Brillouin scattering in optical fibers," *National Physical Laboratory Report COEM 31*, 1999.
- [87] ITU-T, "Recommendation G.650.2, definitions and test methods for statistical and nonlinear related attributes of single-mode fibre and cable," 2007.
- [88] R. G. Smith, "Optical power handling capacity of low loss optical fibers as determined by stimulated Raman and Brillouin scattering," *Applied Optics*, vol. 11, no. 11, pp. 2489-2494, 1972.

- [89] Y. Aoki, K. Tajima, and I. Mito, "Input power limit of single-mode optical fibers due to stimulated Brillouin scattering in optical communication systems," *Journal of Lightwave Technology*, vol. 6, no. 5, pp. 710-719, 1988.
- [90] T. Schneider, *Nonlinear optics in telecommunications*. Heidelberg: Springer-Verlag, Berlin, Germany, 2004.
- [91] J. Hansryd, F. Dross, M. Westlund, P. A. Andrekson, and S. N. Knudsen, "Increase of the SBS threshold in a short highly nonlinear fiber by applying a temperature distributions," *Journal of Lightwave Technology*, vol. 19, no. 11, pp. 1691-1696, 2005.
- [92] J. M. C. Boggio, J. D. Marconi, and H. L. Fragnito, "Experimental and numerical investigation of the SBS-threshold increase in an optical fiber by applying strain distributions," *Journal of Lightwave Technology*, vol. 23, no. 11, pp. 3808-3814, 2005.
- [93] M. Takahashi, M. Tadakuma, and T. Yagi, "Dispersion and Brillouin managed HNLFs by strain control techniques," *Journal of Lightwave Technology*, vol. 28, no. 1, pp. 59-64, 2010.
- [94] L. Grüner-Nielsen, S. Dasgupta, M. D. Mermelstein, D. Jakobsen, S. Herstrom, M. E. V. Pedersen, E. L. Lim, S. Alam, F. Parmigiani, D. Richardson, and B. Pálsdóttir, "A silica based highly nonlinear fibre with improved threshold for stimulated Brillouin scattering," in *proc. OptoElectronics and Communications Conference (OECC)*, 2010, paper Tu.4.D.3.
- [95] Y. Takushima and T. Okoshi, "Suppression of stimulated Brillouin scattering using isolators," in *proc. Optical Fiber Communication Conference (OFC)*, 1992, paper WM6.
- [96] M. J. Li, X. CheX, J. Wang, S. Gray, A. Liu, J. A. Demeritt, A. B. Ruffin, A. M. Crowley, D. T. Walton, and L. A. Zenteno, "Al/Ge co-doped large mode area fiber with high SBS-threshold," *Optics Express*, vol. 15, no. 13, pp. 8290 -8299, 2007.
- [97] L. Grüner-Nielsen, D. Jakobsen, S. Herstrom, B. Pálsdóttir, S. Dasgupta, D. Richardson, C. Lundström, S. Olsson, and P. A. Andrekson, "Brillouin suppressed high nonlinear fibers," in *proc. European Conference on Optical Communication (ECOC)*, 2012, paper We.1.F.1.

- [98] S. K. Korotky, P. B. Hansen, L. Eskildsen, and J. J. Veselka, "Efficient phase modulation scheme for suppressing stimulated Brillouin scattering," in *10th International Conference on Integrated Optics and Optical Fibre Communication, IOOC-95*, 1995.
- [99] M. N. Islam, *Raman amplification for telecommunications 2: sub-systems and systems*. Springer, New York, USA, 2004.
- [100] J. M. C. Boggio, S. Moro, E. Myslivets, J. R. Windmiller, N. Alic, and S. Radic, "155-nm continuous-wave two-pump parametric amplification," *IEEE Photonics Technology Letters*, vol. 21, no. 10, pp. 612-614, 2009.
- [101] C. M. Caves, "Quantum limit on noise in linear amplifiers," *Physical Review D*, vol. 26, no. 8, pp. 1817-1839, 1982.
- [102] K. Inoue, "Polarization effect on four-wave mixing efficiency in a single-mode fiber," *IEEE Journal of Quantum Electronics*, vol. 28, no. 4, pp. 883-894, 1992.
- [103] Q. Lin and G. P. Agrawal, "Vector theory of four-wave mixing: polarization effects in fiber-optic parametric amplifiers," *Journal of the Optical Society of America B*, vol. 21, no. 6, pp. 1216-1224, 2004.
- [104] G. Cappellini and S. Trillo, "Third-order three-wave mixing in single-mode fibers: exact solutions and spatial instability effects," *Journal of the Optical Society of America B*, vol. 8, no. 4, pp. 824-828, 1991.
- [105] K. Inoue and T. Mukai, "Signal wavelength dependence of gain saturation in a fiber optical parametric amplifier," *Optics Letters*, vol. 26, no. 1, pp. 10-12, 2001.
- [106] K. K. Y. Wong, M. E. Marhic, K. Uesaka, and L. G. Kazovsky, "Polarization-independent two-pump fiber optical parametric amplifier," *IEEE Photonics Technology Letters*, vol. 14, no. 7, pp. 911-913, 2002.
- [107] S. Watanabe, F. Futami, R. Okabe, T. Kato, R. Ludwig, C. Schmidt-Langhorst, and C. Schubert, "Polarisation-independent all-optical amplitude limiter using two-stage gain-saturated fiber parametric amplifiers," in *proc. OptoElectronics and Communications Conference (OECC)*, 2009, paper TuD3.

- [108] I. Sackey, R. Elschner, M. Nölle, T. Richter, L. Molle, C. Meuer, M. Jazayerifar, S. Warm, K. Petermann, and C. Schubert, "Characterization of a fiber-optical parametric amplifier in a  $5 \times 28$ -GBd 16-QAM DWDM system," in *proc. Optical Fiber Communication Conference (OFC)*, 2014, paper W3E.3.
- [109] T. Torounidis, H. Sunnerud, P. O. Hedekvist, and P. A. Andrekson, "Amplification of WDM signals in fiber-based optical parametric amplifiers," *IEEE Photonics Technology Letters*, vol. 15, no. 8, pp. 1061-1063, 2003.
- [110] S. Radic and C. J. McKinstrie, "Two-pump fiber parametric amplifiers," *Optical Fiber Technology: Materials, Devices and Systems*, vol. 9, no. 1, pp. 7-23, 2003.
- [111] S. Watanabe, S. Takeda, and T. Chikama, "Interband wavelength conversion of 320 Gb/s ( $32 \times 10$  Gb/s) WDM signal using a polarization-insensitive fiber four-wave mixer," in *proc. European Conference on Optical Communication (ECOC)*, vol. 3, pp. 85-87, 1998.
- [112] H. Hu, H. C. H. Mulvad, M. Galili, E. Palushani, J. Xu, A. T. Clausen, L. K. Oxenlowe, and P. Jeppesen, "Polarization-insensitive 640 Gbit/s demultiplexing based on four wave mixing in a polarization-maintaining fibre loop," *Journal of Lightwave Technology*, vol. 28, no. 12, pp. 1789-1795, 2010.
- [113] I. Sackey, T. Richter, C. Meuer, R. Elschner, M. Jazayerifar, K. Petermann, and C. Schubert, "Characterization of polarization insensitive FOPA using a polarization-maintaining highly non-linear fiber," in *proc. Optical Fiber Communication Conference (OFC)*, 2013, paper OTu2D.2.
- [114] R. Elschner, T. Richter, M. Nölle, J. Hilt, and C. Schubert, "Parametric amplification of 28-GBd NRZ-16QAM signals," in *proc. Optical Fiber Communication Conference (OFC)*, 2011, paper OThC2.
- [115] R. Elschner and K. Petermann, "BER performance of 16-QAM signals amplified by dual-pump fiber optical parametric amplifiers," in *proc. Optical Fiber Communication Conference (OFC)*, 2010, paper OThA4.
- [116] M. C. Ho, M. E. Marhic, K. K. Y. Wong, and L. G. Kazovsky, "Narrowlinewidth idler generation in fiber four-wave mixing and parametric am-

- plification by dithering two-pumps in opposition of phase,” *Journal of Lightwave Technology*, vol. 20, no. 3, pp. 469-476, 2002.
- [117] F. S. Yang, M. E. Marhic, and L. G. Kazovsky, “CW fiber optical parametric amplifier with net gain and wavelength conversion efficiency greater than one,” *Electronics letters*, vol. 32, no. 25, pp. 2336-2338, 1996.
- [118] S. Radic, C. J. McKinstrie, R. M. Jopson, A. R. Chraplyvy, C. G. Jorgensen, K. Brar, and C. Headley, “Selective suppression of idler spectral broadening in two-pump parametric architectures,” *IEEE Photonics Technology Letters*, vol. 15, no. 5, pp. 673-675, 2003.
- [119] F. D. Ros, R. Borkowski, D. Zibar, and C. Peucheret, “Impact of gain saturation on the parametric amplification of 16-QAM signals,” in *proc. European Conference on Optical Communication (ECOC)*, 2012, paper We.2.A.3.
- [120] A. L. Gaeta and R. W. Boyd, “Stochastic dynamics of stimulated Brillouin scattering in an optical fiber,” *Physical Review A*, vol. 44, no. 5, pp. 3205-3209, 1991.
- [121] L. Grüner-Nielsen, S. Herstrom, S. Dasgupta, D. Richardson, D. Jakobsen, C. Lundström, P. Andrekson, M. E. V. Pedersen, and B. Pálsdóttir, “Silica-based highly nonlinear fibers with a high SBS threshold,” in *Winter Topicals (WTM)*, 2010, paper MD3.2.
- [122] F. Yaman, Q. Lin, and G. P. Agrawal, “Effects of polarization-mode dispersion in dual-pump fiber-optic parametric amplifiers,” *IEEE Photonics Technology Letters*, vol. 16, no. 2, pp. 431-433, 2004.
- [123] M. E. Marhic, G. Kalogerakis, and L. G. Kazovsky, “Gain reciprocity in fibre optical parametric amplifiers,” *IEEE Electronics letters*, vol. 42, no. 9, 2006.
- [124] R. R. Nissim, A. Pejkcic, E. Myslivets, N. Alic, and S. Radic, “Origin of non-reciprocal response in fiber optic parametric amplifiers,” *Journal of Lightwave Technology*, p. 55, vol. 33, no. 2, pp. 495-502, 2015.
- [125] I. Sackey, F. D. Ros, J. K. Fischer, T. Richter, M. Jazayerifar, C. Peucheret, K. Petermann, and C. Schubert, “Kerr nonlinearity mitigation: mid link spectral inversion versus digital backpropagation in  $5\times 28$  GBd PDM 16

- QAM signal transmission,” *Journal of Lightwave Technology*, vol. 33, no. 9, pp. 1821-1827, 2015.
- [126] M. Pelusi, “All-optical compensation of fiber nonlinearity by phase conjugation,” in *proc. OptoElectronics and Communications Conference (OECC)*, 2013, paper WS4-7.
- [127] X. Zhou, G. Li, and E. Mateo, “Electronic phase conjugation for impairment compensation in a fiber communication system,” Sept. 30, 2014. US Patent 8,849,126.
- [128] A. Yariv, “Phase conjugate optics and real-time holography,” *IEEE Journal of Quantum Electronics*, vol. QE-14, pp. 650-660, 1978.
- [129] X. Shu, K. Chisholm, and K. Sugden, “Design and realization of dispersion slope compensators using distributed Gires-Tournois etalons,” *IEEE Photonics Technology Letters*, vol. 16, no. 4, pp. 1092-1094, 2004.
- [130] S. L. Jansen, S. Spälter, G. D. Khoe, H. de Waardt, H. E. Escobar, L. Marshall, and M. H. Sher, “16×40Gbit/s over 800km of SSMF using mid-link spectral inversion,” *IEEE Photonics Technology Letters*, vol. 16, no. 7, pp. 1763-1765, 2004.
- [131] H. G. Weber and M. Nakazawa, *Ultrahigh-speed optical transmission technology*. Springer science and business media, New York, 2007.
- [132] S. K. Ibrahim, J. Zhao, F. C. G. Gunning, P. Frascella, F. H. Peters, and A. D. Ellis, “Towards a practical implementation of coherent WDM: analytical, numerical, and experimental studies,” *IEEE Photonics Journal*, vol. 2, no. 5, pp. 833-847, 2010.
- [133] S. Watanabe, S. Kaneko, and T. Chikama, “Long-haul fiber transmission using optical phase conjugation,” *Optical Fiber Technology*, vol. 2, pp. 169-178, 1996.
- [134] T. Merker, P. Meissner, and U. Feiste, “High bit-rate OTDM transmission over standard fiber using mid-span spectral inversion and its limitations,” *IEEE Journal of Selected Topics in Quantum Electronics*, vol. 6, no. 2, pp. 258-262, 2000.

- 
- [135] N. Kikuchi, K. Sekine, and S. Sasaki, "Analysis of cross-phase modulation (XPM) effect on WDM transmission performance," *Electronics letters*, vol. 33, no. 8, pp. 653-654, 1997.
- [136] M. N. Islam, *Raman amplifiers for telecommunications 1: physical principles*. Springer, New York, USA, 2004.
- [137] T. N. Nielsen, A. J. Stentz, K. Rottwitt, D. S. Vengsarkar, Z. J. Chen, P. B. Hansen, J. H. Park, K. S. Feder, S. Cabot, S. Stulz, D. W. Peckham, L. Hsu, C. K. Kan, A. F. Judy, S. Y. Park, L. E. Nelson, and L. Grüner-Nielsen, "3.28-Tb/s transmission over 3 100 km of nonzero-dispersion fiber using dual C- and L-band distributed Raman amplification," *IEEE Photonics Technology Letters*, vol. 12, no. 8, pp. 1079-1081, 2000.
- [138] A. Carena, V. Curri, and P. Poggiolini, "Comparison between different configurations of hybrid Raman/Erbium-doped fiber amplifiers," in *proc. Optical Fiber Communication Conference (OFC)*, 2001, paper TuA3-1.
- [139] N. S. Bergano, F. W. Kerfoot, and C. R. Davidson, "Margin measurements in optical amplifier systems," *IEEE Photonics Technology Letters*, vol. 5, no. 3, pp. 304-306, 1993.
- [140] T. Mizuochi, "Next generation FEC for optical communication," in *proc. Optical Fiber Communication Conference (OFC)*, 2008, paper OTuE5.
- [141] C. Koebele, M. Salsi, G. Charlet, O. Bertran-Pardo, J. Renaudier, H. Mardoyan, P. Tran, and S. Bigo, "Impact of transmitter bandwidth on transmission performance of coherent 112-Gb/s PDM-QPSK systems," *IEEE Photonics Technology Letters*, vol. 22, no. 24, pp. 1859-1861, 2010.
- [142] J. M. Fini and L. Grüner-Nielsen, "Nonlinear fiber designs with intrinsically low dispersion variations," in *proc. Optical Fiber Communication Conference (OFC)*, 2014, paper Tu2K.2.
- [143] F. Yaman, Q. L. L. Radic, and G. P. Agrawal, "Impact of dispersion fluctuation on dual-pump fiber-optic parametric amplifiers," *IEEE Photonics Technology Letters*, vol. 16, no. 5, pp. 1292-1294, 2004.
- [144] D. Marcuse, C. R. Menyuk, and P. K. A. Wai, "Application of the Manakov-PMD equation to studies of signal propagation in optical fibers with randomly varying birefringence," *Journal of Lightwave Technology*, vol. 15, no. 9, pp. 1735-1746, 1997.
-

## BIBLIOGRAPHY

---

- [145] S. G. Evangelides-Jr., L. F. Mollenauer, J. P. Gordon, and N. S. Bergano, "Polarisation multiplexing with solitons," *Journal of Lightwave Technology*, vol. 10, no. 1, pp. 28-35, 1992.



## Appendix A

# Digital Back-propagation (DBP)

The nonlinear Schrödinger equation (NLSE) describes the evolution of an optical field propagating in an optical fiber. There exist no analytical solution of the NLSE: either the scalar NLSE or the coupled NLSE. In a scalar NLSE, the optical field has only one polarization state (e.g. single-polarization data signal) and it is given by equation (3.28) in Chapter 3. The coupled NLSE takes into consideration all the two orthogonal polarizations (e.g.  $x$ - and  $y$ - polarizations) of the optical field (e.g. PDM data signal) propagating in a fiber. In both the scalar and the coupled NLSE, numerical approach presents an approximate solution of the NLSE. The generalized coupled NLSE equation is given by [10, 82]:

$$\frac{\partial A_x}{\partial z} = -\frac{\alpha}{2}A_x - j\frac{\beta_2}{2}\frac{\partial^2 A_x}{\partial T^2} + \frac{\beta_3}{6}\frac{\partial^3 A_x}{\partial T^3} + j\gamma\left[|A_x|^2 + \frac{2}{3}|A_y|^2\right]A_x \quad (\text{A.1})$$

$$\frac{\partial A_y}{\partial z} = -\frac{\alpha}{2}A_y - j\frac{\beta_2}{2}\frac{\partial^2 A_y}{\partial T^2} + \frac{\beta_3}{6}\frac{\partial^3 A_y}{\partial T^3} + j\gamma\left[|A_y|^2 + \frac{2}{3}|A_x|^2\right]A_y \quad (\text{A.2})$$

Where  $A_x$  and  $A_y$  are the optical fields in the  $x$  and  $y$  polarizations. Note that the field is a function of both time and distance of the fiber. The dispersion terms,  $\beta_j$  ( $j = 2, 3$ ), and the nonlinear coefficient term ( $\gamma$ ) as well as the retarded time ( $T$ ) have been explained in Chapter 3. Note that for co-polarized signals, the cross-phase modulation (XPM) induced by field  $A_y$  on field  $A_x$  is given as,  $\Delta\varphi_{XPM} = 2\gamma|A_y|^2L_{eff}$ . However, for orthogonally polarized signals, the coefficient of 2 reduces to 2/3 [82, p. 206] and this is found in the second term of the nonlinear part (terms containing the nonlinear coefficient,  $\gamma$ ) of equations (A.1) and (A.2).

For the purpose of digital back-propagation of PDM signals, the Manakov

equation (modified coupled NLSE) is often used. The generalized Manakov equation is given by [144]:

$$\frac{\partial A_x}{\partial z} = -\frac{\alpha}{2}A_x - j\frac{\beta_2}{2}\frac{\partial^2 A_x}{\partial T^2} + \frac{\beta_3}{6}\frac{\partial^3 A_x}{\partial T^3} + j\gamma\frac{8}{9}\left[|A_x|^2 + |A_y|^2\right]A_x \quad (\text{A.3})$$

$$\frac{\partial A_y}{\partial z} = -\frac{\alpha}{2}A_y - j\frac{\beta_2}{2}\frac{\partial^2 A_y}{\partial T^2} + \frac{\beta_3}{6}\frac{\partial^3 A_y}{\partial T^3} + j\gamma\frac{8}{9}\left[|A_y|^2 + |A_x|^2\right]A_y \quad (\text{A.4})$$

Here the coefficient (8/9) in front of the nonlinear term takes into consideration the averaging of the polarization rotation (over the Poincaré sphere) of the propagating signal in the fiber [145]. The split-step Fourier method is a well-known numerical approach in solving the NLSE [82]. The numerical approach for solving both equations (A.3) and (A.4) are similar to (A.1) and (A.2). Taking (A.3), for instance, the linear terms and the nonlinear terms on the right-hand-side of equation (A.3) can be group and rewritten as:

$$\frac{\partial A_x}{\partial z} = (\hat{D} + \hat{N})A_x \quad (\text{A.5})$$

Where the linear operator,  $\hat{D}$ , is given by:

$$\hat{D} = -\frac{\alpha}{2} - j\frac{\beta_2}{2}\frac{\partial^2}{\partial T^2} + \frac{\beta_3}{6}\frac{\partial^3}{\partial T^3} \quad (\text{A.6})$$

And the nonlinear operator,  $\hat{N}$ , is given by:

$$\hat{N} = j\gamma\frac{8}{9}\left[|A_x|^2 + |A_y|^2\right] \quad (\text{A.7})$$

In the split-step Fourier method, the entire fiber length is divided into several sections (step-size) of length  $h$  and the field of the signal in equation (A.5) is solved by either neglecting the linear operator the nonlinear operator. To improve the accuracy of the algorithm, the symmetric split-step Fourier method is used [10, 31]. The method requires that, the  $h$  section of the fiber is equally divided into two parts. First, the linear operator is applied in equation (A.5) (while the nonlinear operator is set to zero) and the signal amplitude is solved in the frequency domain over fiber length  $h/2$ . Then, inverse-Fourier transform is applied so that the nonlinear operator is solved in the time domain over fiber length  $h$ , by setting the dispersion operator to zero. Finally, the dispersion in the second part of the section is solved, again in the frequency domain over the remaining fiber length of  $h/2$ , by setting the nonlinear operator to zero. The approximation solution of the optical field after propagating over length  $h$  is given as [10, 31]:

$$A_x(z+h, T) \approx \exp\left(\hat{D}(T)\frac{h}{2}\right) \cdot \exp\left(\hat{N}(T)h\right) \cdot \exp\left(\hat{D}(T)\frac{h}{2}\right)A_x(z, T) \quad (\text{A.8})$$

---

The choice of  $h$  has significance on the performance of the algorithm. Small step-size improves the performance but at the expense of computational time and complexity. Implementation of the split-step Fourier method for digital back-propagation requires that the received field is applied in the NLSE with the signs of the terms in the NLSE are reversed. It is worth noting that back-propagation in the thesis did not include amplified spontaneous noise (ASE) and polarization mode dispersion (PMD). In Chapter 7 Section 7.2.3, the received  $5 \times 28$ -GBd PDM 16-QAM data signals after up to 800-km over dispersion-compensated link were back-propagated using the split-step Fourier method for nonlinearity compensation.



# Appendix B

## List of Acronyms

**ADC** analog-to-digital converter

**ASE** spontaneous emission

**AWG** arbitrary waveform generator

**BER** bit-error ratio

**BPD** balanced photodetector

**BPSK** binary phase-shift keying

**CE** conversion efficiency

**CW** continuous wave

**DAC** digital-to-analog converter

**DBP** digital back-propagation

**DBPSK** differential binary phase-shift keying

**DFG** difference-frequency generation

**DGD** differential group delay

**DRA** distributed Raman amplification

**DSP** digital signal processing

**DQPSK** differential quadrature phase-shift keying

**ECL** external cavity laser

<b>EDFA</b>	erbium-doped fiber amplifier
<b>ESA</b>	electrical spectrum analyzer
<b>FOPA</b>	Fiber-based optical parametric amplifier
<b>FFT</b>	fast Fourier transform
<b>FWM</b>	four-wave mixing
<b>FWHM</b>	full-width at half maximum
<b>GVD</b>	group velocity dispersion
<b>HD-FEC</b>	hard-decision forward-error correction
<b>HNLF</b>	highly nonlinear fiber
<b>IDF</b>	inverse dispersion-shifted fiber
<b>LO</b>	local oscillator
<b>MB</b>	main-band
<b>MLSI</b>	mid-link spectral inversion
<b>NLSE</b>	nonlinear Schrödinger equation
<b>NRZ</b>	non-return-to-zero
<b>OOK</b>	on-off keying
<b>OBPF</b>	optical bandpass filter
<b>OPC</b>	optical phase conjugation
<b>OSA</b>	optical spectrum analyzer
<b>OSNR</b>	optical single-to-noise ratio
<b>PBC</b>	polarization beam combiner
<b>PBS</b>	polarization beam splitter
<b>PC</b>	polarization controller
<b>PCTW</b>	phase-conjugated twin waves
<b>PD</b>	photodiode

---

**PDG** polarization-dependent gain

**PDL** polarization-dependent loss

**PDM** polarization-division multiplexed

**PMD** polarization-mode dispersion

**PMF** polarization-maintaining fiber

**PM-HNLF** polarization-maintaining highly nonlinear fiber

**PPLN** periodically-poled lithium-niobate

**PSK** phase-shift keying

**PSA** phase-sensitive amplification

**QAM** quadrature amplitude modulation

**QPSK** quadrature phase-shift keying

**16-QAM** 16-ary quadrature amplitude modulation

**RF** radio frequency

**RIN** relative intensity noise

**ROADM** reconfigurable optical add-drop multiplexer

**RTO** real-time oscilloscope

**SB** side-band

**SBS** stimulated Brillouin scattering

**SE** spectral efficiency

**SLA** super large area

**Si** silicon

**SNR** signal-to-noise ratio

**SOA** semiconductor optical amplifier

**SOP** state-of-polarization

**SP** single-polarization

**SPINE** stable phase-matching for improved nonlinear efficiency

**SPM** self-phase modulation

**SRS** stimulated Raman scattering

**SSFM** split-step Fourier method

**SSMF** standard single-mode fiber

**VOA** variable optical attenuator

**WDM** wavelength-division multiplexing

**WSS** wavelength-selective switch

**XPM** cross-phase modulation

**ZDW** zero-dispersion wavelength

# Appendix C

## List of Symbols

$\alpha$	linear attenuation coefficient
$\beta_j$	$j^{th}$ -order propagation constant
$\gamma$	nonlinear coefficient
$\lambda$	optical wave wavelength
$\lambda_{zd}$	zero-dispersion wavelength
$\omega_{zd}$	zero-dispersion angular frequency
$\omega_0$	optical carrier angular frequency
$\omega_s$	signal angular frequency
$\omega_i$	idler angular frequency
$\omega_p$	pump angular frequency
$f_j$	$j^{th}$ pump phase-dithering tone
$F(x, y)$	transverse modal field distribution
$D_p$	PMD-coefficient
$g_B$	Brillouin gain coefficient
$P_{th}$	Brillouin pump threshold
$A_{eff}$	effective area
$n_{co}$	core refractive index
$n_{cl}$	cladding refractive index
$r_{co}$	core radius
$r_{cl}$	cladding radius
$P_p$	pump power
$P_s$	signal power
$P_{launch}$	launch power

$n_{sp}$	spontaneous emission factor (inversion factor)
$F$	noise figure
$c \cdot c$	complex conjugate
$NA$	numerical aperture
$P$	optical power
$L$	fiber length
$\mathbf{E}$	electric field vector
$\mathbf{P}$	induced electric polarization
$\chi^{(j)}$	$j^{th}$ -order susceptibility
$\epsilon$	material dielectric permittivity
$\epsilon_0$	absolute dielectric permittivity
$\epsilon_r$	relative dielectric permittivity
$k_0$	wave number in free space
$\mu_0$	absolute dielectric permeability
$v_{gr}$	group velocity
$c$	speed of light in vacuum
$D$	dispersion
$S$	dispersion slope
$B$	birefringence
$\Delta\tau$	time delay
$D_p$	PMD coefficient
$\Delta v_p$	optical wave line-width
$\Delta v_B$	Brillouin gain bandwidth
$A(z, t)$	complex amplitude
$\Delta\varphi_{SPM}$	nonlinear phase shift due to self phase modulation
$\Delta\varphi_{XPM}$	nonlinear phase shift due to cross phase modulation
$R_S$	symbol rate
$R_B$	bit rate
$M$	modulation order
$\Re\{x\}$	real part of $x$
$\Im\{x\}$	imaginary part of $x$
$R$	responsivity
$B_0$	optical bandwidth
$P_0$	output power

---

$\Delta\beta$	linear phase mismatch
$\kappa$	total phase mismatch
$g$	parametric gain coefficient
$P_{SB}$	side-band power
$P_{MB}$	main-band power
$z$	transmission length
X-Pol	$x$ -polarization
Y-Pol	$y$ -polarization
$Q^2$	signal quality factor
Tb/s	terabit per second
Pb/s	petabit per second
dB	decibel
$N$	number of fiber segments
Tx	transmitter
Rx	receiver
$I$	in-phase component
$Q$	quadrature component
w	with
w/o	without
GS/s	giga samples per second
GBd	gigabaud
$\lambda_p$	pump wavelength
$\lambda_s$	signal wavelength
<i>a.u.</i>	arbitrary unit
$m$	number of steps per fiber
$ch$	WDM channel
$\varphi_p$	pump phase
$\varphi_s$	signal phase
$\varphi_i$	idler phase
$\varphi(t)$	symbol phase
$V$	V-parameter
$\hat{D}$	linear operator
$\hat{N}$	nonlinear operator

---



## Appendix D

# Author Publications

### Peer-reviewed Journal Publications

- [J1] **I. Sackey**, T. Richter, M. Nölle, M. Jazayerifar, K. Petermann, J. K. Fischer, and C. Schubert, “Qualitative comparison of Kerr nonlinearity mitigation schemes in dispersion-managed link for  $4\times 28$  GBd 16-QAM signals,” *Journal of Lightwave Technology*, vol. 33, no. 23, December, 2015.
- [J2] **I. Sackey**, F. Da Ros, T. Richter, J. K. Fischer, M. Jazayerifar, C. Peucheret, K. Petermann, and C. Schubert, “Kerr nonlinearity mitigation: Mid link spectral inversion versus digital back-propagation in  $5\times 28$  GBd PDM 16-QAM signal transmission,” *Journal of Lightwave Technology*, vol. 33, no. 9, May, 2015.
- [J3] **I. Sackey**, F. Da Ros, M. Jazayerifar, T. Richter, C. Meuer, M. Nölle, L. Molle, C. Peucheret, K. Petermann, and C. Schubert, “Kerr nonlinearity mitigation in  $5\times 28$  GBd PDM 16-QAM signal transmission over a dispersion-uncompensated link with backward-pumped distributed Raman amplification,” *Optics Express*, vol. 22, no. 22, 2014.
- [J4] M. Jazayerifar, S. Warm, R. Elschner, D. Kroushkov, **I. Sackey**, C. Meuer, C. Schubert, K. Petermann, “Performance evaluation of DWDM communication systems with fiber optical parametric amplifiers,” *Journal of Lightwave Technology*, vol. 31, no. 9, May, 2013.

## Peer-reviewed Conference Papers

- [C1] **I. Sackey**, M. Jazayerifar, R. Elschner, T. Richter, C. Meuer, K. Petermann, and C. Schubert, “Non-reciprocal gain due to counter-propagating pumps in a polarization-independent FOPA with diversity loop,” in *proc. European Conference and Exhibition on Optical Communication (ECOC)*, Valencia, Spain, 2015, paper We.2.4.6.
- [C2] M. Jazayerifar, **I. Sackey**, R. Elschner, F. Da Ros, T. Richter, C. Meuer, C. Peucheret, C. Schubert, and K. Petermann, “Perspectives of long-haul WDM transmission systems based on phase-insensitive fiber-optic parametric amplifiers,” in *proc. IEEE Photonics Society Summer Topical Meeting Series*, Bahamas, 2015, paper TuF4.1.
- [C3] F. Da Ros, **I. Sackey**, M. Jazayerifar, T. Richter, R. Elschner, C. Meuer, M. Nölle, L. Molle, K. Petermann, J. K. Fischer, C. Schubert, and C. Peucheret, “Optical phase conjugation for nonlinearity compensation in WDM PDM 16-QAM transmission over dispersion compensated and dispersion uncompensated links,” in *proc. IEEE Photonics Society Summer Topical Meeting Series*, Bahamas, 2015, paper MF1.1.
- [C4] **I. Sackey**, M. Nölle, T. Richter, J. K. Fischer, M. Jazayerifar, K. Petermann, and C. Schubert, “Evaluation of Kerr Nonlinearity based on digital back-propagation and digital coherent superposition,” in *proc. Photonic Networks, 16. ITG Symposium*, pp. 135-139, Leipzig, Germany, 2015.
- [C5] P. W. Berenguer, **I. Sackey**, C. Schubert, and J. K. Fischer, “Quantization of Volterra kernel coefficients for reduced complexity,” in *proc. Photonic Networks, 16. ITG Symposium*, pp. 162-166, Leipzig, Germany, 2015.
- [C6] **I. Sackey**, F. Da Ros, T. Richter, R. Elschner, M. Jazayerifar, C. Meuer, C. Peucheret, K. Petermann, and C. Schubert, “Design and performance evaluation of an OPC device using a dual-pump polarization-independent FOPA,” in *proc. European Conference and Exhibition on Optical Communication (ECOC)*, Cannes, France, 2014, paper Tu.1.4.4.
- [C7] M. Jazayerifar, **I. Sackey**, R. Elschner, S. Warm, C. Meuer, C. Schubert, and K. Petermann, “Impact of SBS on polarization-insensitive single-pump optical parametric amplifiers based on a diversity loop scheme”, in *proc. European Conference and Exhibition on Optical Communication (ECOC)*, Cannes, France, 2014, paper Tu.4.6.4.

- 
- [C8] F. Da Ros, **I. Sackey**, R. Elschner, T. Richter, C. Meuer, M. Nölle, L. Molle, M. Jazayerifar, K. Petermann, C. Peucheret, and C. Schubert, “Kerr non-linearity compensation in a  $5\times 28$  GBd PDM 16-QAM WDM system using fiber-based optical phase conjugation,” in *proc. European Conference and Exhibition on Optical Communication (ECOC)*, Cannes, France, 2014, paper P.5.3.
- [C9] F. Da Ros, M. Nölle, C. Meuer, A. Rahim, K. Voigt, A. Abboud, **I. Sackey**, S. Schwarz, L. Molle, G. Winzer, L. Zimmermann, C. G. Schäffer, J. Bruns, K. Petermann, and C. Schubert, “Experimental demonstration of an OFDM receiver based on a silicon-nanophotonic discrete Fourier transform filter,” in *proc. IEEE Photonic Conference*, San Diego, CA, USA, 2014, paper MG2.5.
- [C10] **I. Sackey**, R. Elschner, M. Nölle, T. Richter, L. Molle, C. Meuer, M. Jazayerifar, S. Warm, K. Petermann, and C. Schubert, “Characterization of a fiber-optical parametric amplifier in a  $5\times 28$ -GBd 16-QAM DWDM system,” in *proc. Optical Fiber Communications Conference (OFC)*, San Francisco, CA, USA, 2014, paper W3E.3.1.
- [C11] M. Jazayerifar, S. Warm, R. Elschner, **I. Sackey**, C. Meuer, C. Schubert, and K. Petermann, “Investigation of nonlinear effects in long-haul DWDM communication systems with in-line fiber optic parametric amplifiers,” in *proc. Photonic Networks, 14 ITG Symposium*, Leipzig, Germany, May 2013.
- [C12] **I. Sackey**, T. Richter, C. Meuer, R. Elschner, M. Jazayerifar, K. Petermann, and C. Schubert, “Characterization of polarization insensitive FOPA using a polarization-maintaining highly non-linear fiber,” in *proc. Optical Fiber Communications Conference (OFC)*, Anaheim, CA, USA, 2013, paper OTu2D.2.

\*It is worth noting that some of the results in the following publications have been used in the thesis: [J2], [J3], [C1], [C2], [C3], [C6], [C7], [C8], and [C12].